Università degli Studi di Udine

CORSO DI DOTTORATO DI RICERCA IN SCIENZE E TECNOLOGIE CLINICHE
CICLO XVIII

TESI DI DOTTORATO DI RICERCA

A MEMS (Micro Electro Mechanical Systems) approach to highly sensitive multiplexed biosensors

DOTTORANDA
Martina Tardivo

RELATORE
Prof. Giacinto Scoles

CO-RELATORE
Dr. Marco Lazzarino

ANNO ACCADEMICO
2015/2016

Abstract

In the field of Micro Electro Mechanical Systems (MEMS), micro and nanomechanical resonators are playing a growing role in biosensing. Thanks to their extreme sensitivity, fast response and low cost, they can be competitive with current diagnostic systems. Nonetheless, the real challenge for new biosensing techniques consists in multiplexing functionality, the ability to detect more than one ligand simultaneously. In this direction, a promising approach is offered by micropillars technology, and in this project, the advantages coming from their geometry are exploited to develop a new high sensitive and multiplexing biosensor. Micropillars are vertical oriented micromechanical resonators, used as mass sensors, in which the biomolecular adsorption is confined on their micron sized top area. This allows an easy quantification of the deposited mass and a reduction of the response time due to a faster diffusion mechanism. Moreover, pillars can be easily arranged in dense arrays of several thousand sensors in a square millimeter, offering a promising platform for multiplexing.

In order to obtain a further improvement in sensibility, specificity and speed of analysis, an amplification of the signal, coming from the deposited mass, has been investigated. A sandwich assay approach based on functionalized gold nanoparticles has been applied and the signal amplification has been demonstrated using a biotin-streptavidin system.

A multiple functionalization and a parallel read-out detection method have been also developed in order to drive the sensor towards a multiplexing system. The first target has been reached treating the pillar surface with a photocleavable thiol on which, after the UV laser exposure, -NH2 groups are available and can be used to introduce other functionalities, such as antibodies, through the reaction with –COOH groups. Afterwards, the best condition for the chain cleavage and the amine coupling have been investigated, using -COOH fully coated Quantum Dots as binding elements.

Moreover, thanks to a further optimization of the pillar geometry, that lead to structures with a larger oscillation amplitude, the development of an innovative strategy for a parallel read-out based on CCD imaging and software image analysis has been carried out.

Advantages from this method are demonstrated also for a single marker detection: acquiring simultaneously the frequency shift of tens pillars and applying a proper statistical analysis, it's possible to overcome the variability of the single measures improving the device sensitivity.

As proof of principle this method has been applied for the detection of PSMA (Prostate Specific Membrane Antigen) at diagnostically relevant concentrations (nM level) both from physiological solution and serum.

Index

Chapter 1

Introduction to biosensors

In this chapter, the concept of surface sensing is introduced, focusing on biomedical applications and outlining the performances required in this field. After a brief description of the different types of surface biosensors, a more detailed explanation of micromechanical technology is provided, as well as an overview of the issues concerning its use in clinical diagnostic applications. Following, micropillars technology is introduced as a promising solution for part of the previously mentioned problems. Finally the scope of this research project, the development of a highly sensitive and multiplexing biosensor, is illustrated.

1.1 Surface sensing in biomedical application

Chemical Sensors are devices used to detect, quantify and monitor chemical species (named analyte or ligand) in a liquid or gas environment. Information about the species is provided in form of measurable physical signals and is correlated with their concentrations.

The two main constituents of a sensor, determining the sensor type but also its performances, are: a recognition element, in whose structure a receptor is included, and the solid transducer. The recognition element is attached to the transducer, thus, when the analyte interacts selectively with the receptor, the physicochemical change, induced by the recognition, is converted into a physical measurable output signal by the transducer.

The versatility of chemical sensors is manly related to the possibility to tune their application developing a proper recognition interface. The sensitive area is modified to allow a high specific interaction with the target molecule, even in a complex mixture of other species that can be several orders of magnitude more abundant than the one to be detected. When the sensitive area is modified with a biological layer, a biomolecular sensor surface is defined. The most common biological interfaces are made of antibodies or nucleic acids (DNA/RNA). Thus, biosensors are generally characterized by high affinity and selectivity; recognition is based on antibody-antigen binding, with a dissociation constant at the nanomolar scale, or on the even stronger interaction obtained with hybridization of complementary nucleic acids (DNA/RNA). In this filed, the most innovative approaches involve the use of small receptor (aptamers)[1, 2] made of oligonucleotides or peptides, that are selected among all the possible configuration in order to have high affinity to the target molecule. Due to their small dimension compared to larger receptors, they can be easily synthesized with good chemical stability and cost effectiveness, can access also concealed protein epitopes and be modified with reporters, functional groups, signal moieties.

Thanks to this versatility, since the 80s, biosensors are experiencing a widespread development in different application fields, such as in food safety, to assess the quality of drinking water or to detect the presence of allergens or drug residues as antibiotics or growth promoters in food, and in the clinical field, to monitor the presence of diagnostically relevant molecules [3].

80% of all commercial biosensor devices are developed for medical application [4]. Nowadays, a wide variety of biosensors for metabolites such as glucose lactate, cholesterol, and creatinine are available; like the glucose biosensors, commercial tests such as for pregnancy (hCG), Escherichia coli O157, influenza A and B viruses, Helicobacter pylori, human immunodeficiency virus, tuberculosis, and malaria have achieved success providing great advantages in diagnostic[5].

Research on biosensors is highly interdisciplinary, in particular, in case of biomedical applications, the increasing clinical needs of more and more fast, accurate and precise diagnosis can be satisfied exploiting at the same time the advances in molecular biology, as well as in the areas of microelectronics, micro fabrication, material science and optics. In recent years, novel, high performances biosensors have been proposed for measurement of cancer biomarkers, cardiac biomarkers as well as biomarkers for autoimmune disease, infectious disease and for DNA analysis, also including measurements in alternate sample types, such as saliva. The number of research reports describing promising biosensors for analytes of clinical interest continues to increase; however, the translation of this new technology from the research laboratory to the clinical is much slower [6]. To change this tendency, new technologies have to focus on both the intrinsic and the overall sensor system performances.

The intrinsic biosensor performances are identified as [3]:

- detection limit, commonly defined as the minimum concentration that can be reliably detected and that provides a response signal that is three times the level of the background noise;
- specificity, the capability to distinguish the signal generated by the analyte among those generated by other species;
- detector sensitivity, that is the change in signal per unit value of the sensor response and is function of the sensor properties but also of the measurement and amplification techniques employed;
- dynamic range, the range of concentration which can be detected comprised between no signal and saturation;
- repeatability of the measurements;
- response time, which may depend on several different parameters, such as analyte diffusion and transport to the biointerface, the time required to transduce the signal, the number of events necessary to produce a detectable signal.

The performances of the overall system are related to: the complexity of fabrication and integration; the potential of multiplexing; the device robustness and shelf life; the trade-off between sensitivity and frequency of false positives; the readiness and adaptability for mass production [6].

For many biomarkers the diagnostic level of significance is within the picomolar and the nanomolar range and can be reached by conventional immunofluorescence assays; thus, the real challenge for new biosensors technologies is to achieve this sensitivity, or better, in combination with a shorter analysis time and a multiplexing functionality-the ability to detect more than one ligand simultaneously [7].

Disease diagnosis and therapeutical response often involve the interplay between a variety of complex biological networks encompassing multiple rather than single markers, thus, currently the multiplexing potential of a biosensor strongly increases the power of the diagnosis. Moreover multiplexing technologies express their maximum efficiency when they are array-based, and the use of platforms - that allows simultaneous capture of several analytes - is coupled with a parallel detection technique. Thus, the high density of information per sample volume, decreases the cost and time of analysis.

Commercially available multiplexing devices, based on standard beads or planar array technology, suffer from limitations as low flexibility and scalability which slow down the turnaround time (time-to-result) in routine clinical testing [8]. In the recent years, well established technologies have been improved also through microfluidic integration, mainly with the aim of reducing the analysis time [9, 10]. Instead, the most interesting multiplexing medical application have been provided exploiting the advantages offered by biosensors based on nano-micro fabrication technology; some examples are: the detection of a six different cytochins down to 20pg/mL to monitor the inflammatory response of infants after cardiopolmunary bypass [11]; the development of a novel sandwich-type electrochemical immunosensor for simultaneous detecting of carcinoembryonic antigen (CEA) and alpha-fetoprotein (AFP) [12]; and finally Maverick^{TM} devices, introduced by Ganelyte in 2012, consisting of a diagnostics platform, based on commercial multiplex silicon photonic chip, for rapid detection of up to 32 biological analytes from a drop of sample in just 10 to 20 minutes [13].

1.2 Classification of surface based biosensors

Based on the nature of the transduction signal, obtained by the conversion of the bio-recognition physicochemical signal into a measurable output, biosensors are generally classified into electrical, optical or mechanical. In figure 1.1, adopted from [14], the most common biosensors are schematically divided into the defined class.

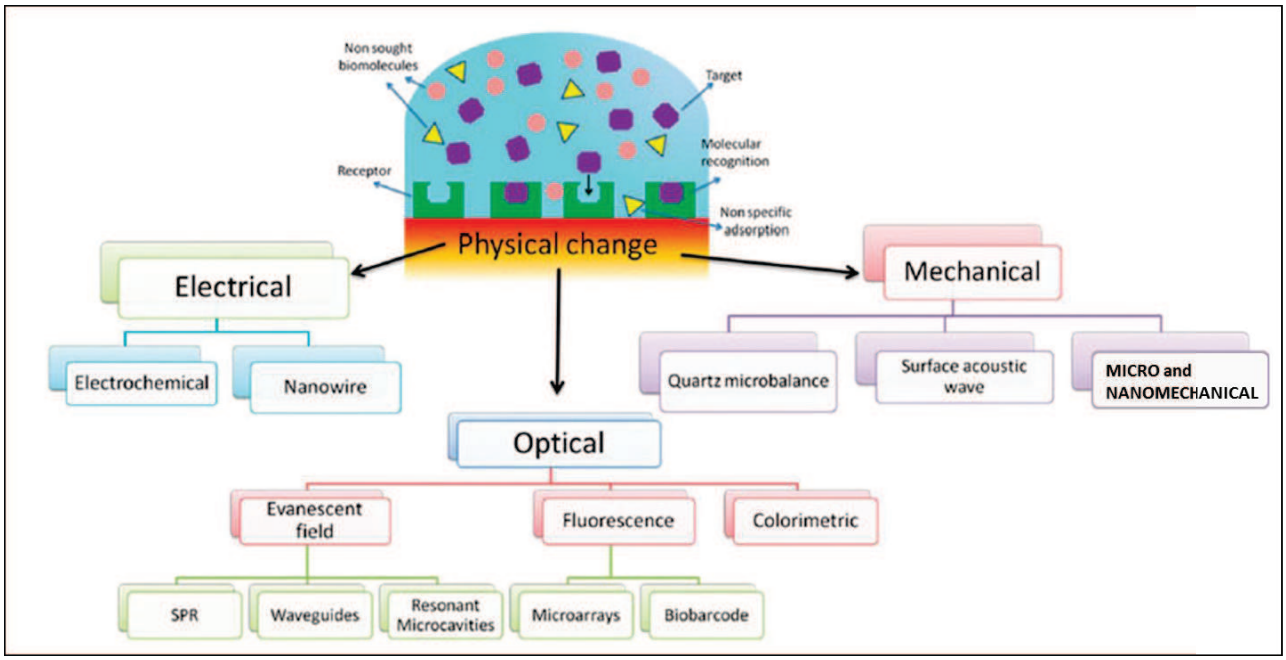

Figure 1.1 *–Schematic representation of the most common surface biosensors divided into electrical, optical and mechanical classes, based on the nature of their transducer*

Due to their mature and well established technology, optical and electrical biosensors have dominated in both research laboratories - considering the number of publications from 1985 to 2010 [14] - and clinical diagnostic [15]. As it will be shown in the following paragraphs, most of the diagnostic assays are based on the detection of optical labeled molecules, and the disadvantages of this approach could be easily overcome using electrical methods. Nonetheless, the needs of more sensitive, fast and multiplexing response lead micro- and nano-mechanical sensors (belonging to the mechanical class) to gain a growing attention as biomolecular sensors, also due to the possibility to be competitive in term of cost, since the use of the well-established semiconductor technology enables a low cost batch production.

1.2.1 Electrical biosensors

Electrical sensors exploit the charge transfer due to a reaction on the sensor surface, or the surface potential change due to the molecular adsorption or binding.

In the first case a bioelectrochemical sensor is defined. In these devices, an enzyme is usually immobilized on the sensor surface and the reaction with the analyte forms a donor/acceptor couple that produces the charge transfer to the sensing element. The effect of this bioelectrochemical reaction is detected between two electrodes - one of which is represented by the sensors surface - as measurable current (amperometric detection) ore measurable potential or charge accumulation (potentiometric detection).

Electrochemical biosensors have experienced the most widespread diffusion manly as amperometric devices. The most common example of electrochemical sensor is represented by the glucose sensor. In the majority of the commercial devices the amperometric signal due to the reaction of glucose and the immobilized glucose

oxidase (GOx) enzyme is measured, in presence of a mediator that is oxidized/reduced at the electrode surface leading to a circulating current. Currently, disposable chips made of layers of electrodes, spacers and immobilized enzymes are commercially available at low cost, allowing several analysis during a day through a point-of-care device, in which just a blood drop from a pricked finger is enough to have information about glucose levels in blood. The required range of detection in this kind of analysis is quite high, ranging from 1-30 mM as extremes values for episode of hypo or hyper-glycemia, with a required detection resolution in the order of 50 μM [16]. In addition to glucose oxidase, other enzymes are commonly immobilized to catalyse the reaction of clinically relevant analytes as cholesterol, urate or glutamate [17].

Nanowires and carbon nanotubes are also emerging as an extremely powerful electrical sensor in field effect transistors (FET) for molecular and biomolecular detection at the single molecule level, exploiting the conductance changes when the target molecule binds to the surface of the device, due to a change in local surface potential or in the solution pH. The extremely high surface-to-volume ratio of nanowires and nanotubes makes these devices much more sensitive compared to the planar FET sensor, as it will be discussed later in this chapter.

As applications of nanowires FET in biosensing, in 2005, Lieber' group proposed an highly sensitive, label-free, multiplexed electrical detection of cancer markers using silicon-nanowire field-effect devices in which distinct nanowires and surface receptors are incorporated into arrays[18]. In 2007 Kim *et al.* demonstrated the detection of prostate specific antigen (PSA) in real time at 1fg/ml concentration[19]. In 2011, silicon nanowires FET have been applied to detect target DNA at 1fM concentration and to distinguish single-nucleotide polymorphisms [20], while recently in Wang's group, Alpha-fetoprotein, a tumor-associated fetal protein, has been detected down to pM concentration [21].

Regarding carbon nanotubes, in 2014, two interesting application were demonstrated. A flexible, nonenzymatic glucose biosensor based on Ni-coordinated, vertically aligned carbon nanotube arrays was developed and tested detecting glucose in a linear range of 0.05 to 1.0 mM and with a detection limit of 30μM [22]. Zhu's group has proposed an electrochemical Glucose oxidase biosensor by vacuum-impregnation of a glucose oxidase in a polyvinyl alcohol (PVA) aqueous solution into carbon nanotubes (CNTFs)[23].

1.2.2 Optical biosensors

Among the optical biosensing techniques, a first important distinction can be made between labeled and label-free detection methods. In the first case, target molecules reacts with optically active molecules and the signal of the latter is detected and related, through a calibration curve, to the concentration of the first. Based on their nature, the detectable signal can be produced directly from the tag (it is the case of fluorofors, colored tags (Qds), radioactive tag) or after the reaction of the tag with a proper substrate. This is the case, for example, of the horseradish peroxidase (HRP), an enzyme-conjugated biomolecule: after biomolecular

binding to the target, the complex is exposed to a solution of a substrate for the enzyme, which produces a colorimetric change proportional to the amount of the target molecule.

The most common example of optical labeled analysis is represented by the ELISA (Enzyme-linked immunosorbent assay), commonly used in the clinical practice. It has the advantage to detect molecules at sub-picomolar level in almost one hour [7], but it is limited by the number of different biomolecules that can be detected on the same assay.

Labeled markers are commonly applied also for protein or nucleic acids detection through the microarray technique, where thousands of different probes can be immobilized on a solid support (glass, silicon or plastic) by automatic ink-jet spotting or by lithographic techniques. It is the case of Affymetrix® gene chip, where nucleotides sequences are formed in situ by selective exposure of portions of the substrate to UV light.

Another interesting example is the Biobarcode assay, introduced by Mirkins in 2003 [20]. It exploits the combination of two different sets of particles: one made of gold and functionalized with polyclonal antibodies and a barcode DNA sequence, and the other made of a magnetic material (typically iron) decorated with monoclonal antibodies. In presence of the target molecule, a sandwich-like assay is formed; then, the complex is separated by the application of a magnetic field and the DNA barcode is dehybridized. The free DNA sequences are fluxed to the detection area, where they bind their complementary sequences which are immobilized on a glass surface, and detected through a further hybridization with gold nanoparticles decorated with specific DNA sequences. This technique has been demonstrated to detect prostate specific antigen (PSA) biomarker at 500 aM concentration [21].

Although Biobarcode assay is compatible with multiple protein detection, being the antibodies and the DNA sequence specific for each target, the multiplexing detection is rather complex, being still subjected to the availability of different antibodies capable to bind the same target, which represent the main limit of the labeled techniques.

The optical label-free methods generally exploit the evanescent field effect produced on the sensor surface by incident light with a precise angle. The evanescent field exponentially decays moving into the bulk solution at a depth from tens to hundreds of nanometers [24]. Receptor biomolecules, such as antibodies, DNA sequences or aptamers are immobilized on the sensor surface; the measurement chamber is filled with the solution containing the analyte; when the target molecule binds the receptor, close to the surface, a local change of the refractive index is produced.

The most common example is the Surface Plasmon Resonance (SPR) technique: a charge density oscillation (surface plasmon wave, SPW) generated at the interface of two media of opposite dielectric sign (gold or silver as metal and a dielectric material) interacts with the evanescent field created by the incident light. At specific resonant angle or resonant wavelength, coupling between photon and SPW occurs. The change of the refractive index, due to the binding of the target molecule on the surface, results in a change of the resonance angle, of the resonance wavelength or of the resonance intensity. One example of commercial SPR sensor is Biacore™ , also used in the clinical practice to monitor cancer biomarkers with sensitivity at the

nanomolar level; however, enhancing SPR signal with an end-point sandwich assay based on gold nanoparticles, sub-femtomolar sensitivity have been reached on oligonucleotide detection [25]
In addition to be a label-free technique, another advantage coming from the SPR technique is the fast response, that allows real time measurements and the absence of pre-treatment steps; moreover, when the SPR is operated in the imaging mode and coupled with a microarray platform, sequence-specific multiplex analyses can be conducted [26] . On the opposite: being the surface usually in the squared centimetre range, this technique suffers from mass transport limitation, which strongly influences the binding kinetic and therefore the intensity of the signal; the SPR signal can be strongly influenced by artefacts changing the refractive index, requiring a reference element to avoid spurious effects.
Finally, with the aim of developing transducers exhibiting ultimate detection limits, research is focusing on waveguides and optical microcavities based sensors. These technologies exploit the total internal reflection effect obtained on their geometries to generate an evanescent field at the surface, which, again, is exponentially depleted inside the liquid and is influenced by the binding of molecules with their receptors. Fan *et al.,* in 2008, have defined that the detection limits of this new optical technologies ranges from 0.1μM to 3pM [13, 24], but Baaske *at al.,* in a more recent work, introduced a biosensing platform optical microcavity-based that exhibits single-molecule sensitivity and is selective to specific single binding events [27].

1.2.3 Mechanical sensors

Mechanical biosensors are based on the effect of bioadsorption on the surface of the sensor, which induces a mechanical change that can be quantified and related to the amount of adsorbed mass. The mass deposition induces a surface stress effects that leads to the bending of the structure, or to a change of the mass and/or stiffness of the sensor, inducing a change of the resonance frequency. In the particular case of surface acoustic wave sensors, the bioadsorption changes the mass and the viscosity of the biofunctional layer, affecting properties as the velocity of transmission, the amplitude, the resonance frequency and the delay time of a wave travelling on the surface of the sensor [3, 28].
One of the first example of mechanical mass sensor is represented by the quartz crystal microbalance: a centimeter-scale resonator (the typical diameter is 14 mm) is used for the quantification of the deposited mass through the shift of its resonance frequency; due to its piezoelectric nature, through electrical methods, a direct and real time measurement of the resonance can be performed [29, 30] .
Quartz crystal microbalances have been widely used for detection in vacuum, gas or liquid phase; moreover, due to their shear motion parallel to the liquid, that strongly reduces the dissipation of the medium, a narrow resonator's bandwidth can be obtained, while the resonance frequency span is usually between 5-25 MHz
This has allowed the application of these sensors also to the study of the viscoelastic properties of thin biological films in a liquid environment [14]. The application of this device for biological detection has

shown limits of detection ranging from the nM level in liquid to the fM by the application of a sandwich-like assay and measurements in vacuum [7].

Another important example in mechanical biosensing is represented by micro- and nano- sized cantilevers: horizontal structures clamped to one end to the solid substrate; the adsorbed mass is quantified from their bending (static mode) or by measuring the variation of their resonance frequency (dynamic mode). Due to their importance in mechanical biosensing and for the work which is here presented, more details about their structure, operational mode are given in §1.3 while their actuation and detection is discussed in Chapter 2.

A further reduction of the dimensions of these oscillators has led to the use of silicon nanowires (SiNW) and carbon nanotubes (CNT) as extremely sensitive mass sensors; in past years, high sensitive applications in ultra-high vacuum ware proposed. Suspended single crystal silicon nanowires were fabricated in Roukes' group through a bottom-up approach, the resonance frequency was measured considering the power transmitted through the nanowire, and the mass resolution demonstrated by this resonator was around 10 fg [31]. In 2012 Y. Lu at al. presented a nanomechanical mass-sensing resonator made of ordered vertical nanowire arrays on top of a Si/SiO2 bilayer thin membrane; exploiting the high surface area-to-volume ratio of the device (108 m-1), DNA detection at femtomolar concentration was demonstrated [32]. Chaste *et al.* , by using a double clamped CNT, demonstrated a further reduction of mass resolution down to the yoctogram level (10-24 g), corresponding to the mass of a single proton[33] . On the other hand, Sawano at al. pointed that the nanometric size of these structures makes the damping of the surrounding medium the dominant effect, hindering their application as reliable sensors at environmental conditions, such as liquid [34].

1.3 Micro and nanocantilevers as biosensing tools

Micro and nano cantilevers were initially conceived in the 80' as a tool for the atomic force microscopy, but they experienced soon a wide diffusion also as biomolecular sensor [35] so that today they are present on the market as commercial devices such the systems produced by Mecwins. This was mainly because of their high sensitivity coming from their reduced mass and the possibility to perform label-free detection and to monitor in real time different biomolecules on the same array through parallel functionalization. In addition, their compact scale allows easy integration with other electrical, mechanical or microfluidic components on the same device.

When a molecule adsorbs on the sensitive part of a cantilever, the increase of the cantilever mass modifies its mechanical behaviour and this change can be reflected on the bending of the structure or on the change of the resonance frequency. Based on the observed effect, cantilevers can be measured in static or dynamic mode, as shown in figure 1.2

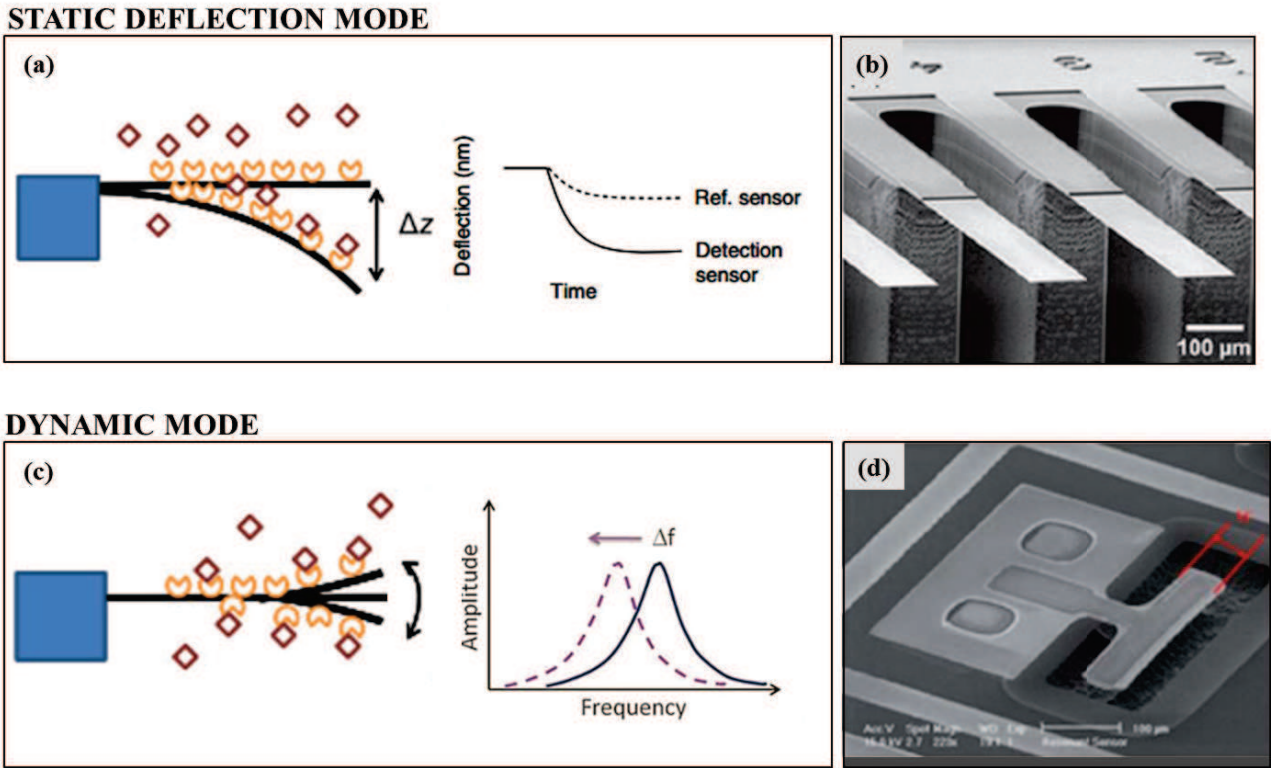

Figure 1.2 – *Operation mode of horizontal micro/nano cantilever. (a)The static mode, in which the bending of the structure is measured; (b) an array of horizontal microcantilevers for static operational mode, image from [14]. (c The dynamic mode, in which the resonance frequency shift is monitored; (d) A lateral extensional mode piezoelectric resonator, image from[36].*

1.3.1 Static operation mode

In the static operation mode, the cantilever bending is the result of the elastic expansion or contraction of its structure, generated by the difference in the surface stress between the top active side and the passivated back side. The surface stresses can be generated by a redistribution of the electron cloud of the surface atoms, that modifies the inter-atomic interactions at the interface. Another possible cause for surface stresses can be found in adsorbate-adsorbate interactions (steric forces, electrostatic forces, hydrogen bonding, desolvation interactions and entropic effects consequent to the molecular binding).

In the case of homogeneous and isotropic cantilever, with thickness much lower than the lateral dimensions and on the hypothesis of small strain and rotations due to stress, the deflection δ of a cantilever can be related to the differential stress through the following Stoney's formula:

$$\delta = \frac{(1-\nu)}{E}\left(\frac{L}{t}\right)^2 \Delta\sigma \qquad 1.1$$

Where υ, the Poisson ratio and E, the Young modulus define the material elastic properties; L and t are the cantilever length and thickness, respectively. Eqn. 1.1 cannot be applied close to the clamp region, where

the deformation is hampered by the anchoring of the cantilever to the support. To describe the curvature along the longitudinal position other models have been formulated [37].
Surface stress effects lead usually to displacements in the order of nanometer or sub-nanometer. To increase the transduction effect the main parameters to act on are the geometry (increasing the aspect ratio L/t) and mechanical properties of the cantilever (reducing the Young modulus, as in the polymer based cantilevers)
As successful application of cantilevers in static detection can be cited: in 2000, Gerber *et al.* with the differential bending of two gold coated cantilevers, previously functionalized with complementary and non-complementary single strand DNA, demonstrated the capability to distinguish between single-base mismatches [38]. Wu *et al*. applied for the first time this technique to the detection of prostate specific antigen (PSA) in a complex mixture of bovine serum albumin and human plasminogen, providing a detection limit of 100 pM [39]. Very recently, Ndieyira and co-workers have demonstrated the use of nanomechanical cantilevers as a surface-stress sensor to monitor the mechanical response of receptor molecules (analogous to the ones of the bacterial cells) immobilized on cantilevers to the exposure at different concentrations of two different antibiotics. The consequent bending of the cantilevers allowed the study of the influence of weak and strong competing ligands in serum, which severely affects the amount of free drug interacting with the immobilized receptors, allowing also the direct comparison of the effects of different drugs. It is noteworthy to stress that this technique revealed an effective bending of the cantilever at a minimum antibiotic concentration of 10 nM, while in the SPR technique commonly used for this kind of studies, the minimum detectable concentration is of 300 nM[40].

1.3.2 Dynamic operation mode

Cantilevers which operate in dynamic mode are defined "micro/nanomechanical resonators"; they are characterized by resonating frequencies related to the different modes at which they can oscillate,
A load applied on the resonator surface induces a modifications on both the overall mass and on the stiffness of the system, producing a variation of the resonance frequency.
Cantilevers can oscillate both out of plane (flexural modes and torsional modes) or in plane (lateral modes and longitudinal modes). A complete description of the mathematical models for these different modes are reported in Johnson and Mutharasan's review[41].
In general, the cantilever behavior is commonly described through a lumped model: as a spring of elastic constant k with a mass m loaded at its end, that oscillates in a viscous medium[42]. If a periodic force F(t) is applied, the system can be modeled as a forced harmonic oscillator with a damper, described by the following equation:

$$m\ddot{x} + m\gamma\dot{x} + kx = F(t) \qquad 1.2$$

where γ represents all the damping sources and x is the system displacement during the periodic oscillation.
If the driving force is expressed as $F = F_0\cos(\omega t)$, the solutions for Eqn. 1.2 are

$$x(t) = \frac{F}{m}\frac{1}{\sqrt{\left(\omega_0^2-\omega^2\right)^2+(\gamma\omega)^2}}\cos(\omega t+\theta) \qquad 1.3$$

$$\tan\theta = -\frac{\gamma\omega}{\omega_0^2-\omega^2} \qquad 1.4$$

where θ represent the phase shift between the actuating force and the cantilever oscillation.

The natural angular frequency (eigenfrequency) is defined as $\omega_0 = \sqrt{k/m}$ and the amplitude x(t) has a maximum for $\omega = \omega_0\sqrt{1-1/2Q^2}$, where Q is the quality factor of the resonator.

The quality factor is experimentally obtained from the ratio between the resonance frequency fr and the full width at the half maximum (FWHM) of the resonance peak: the larger is Q, the sharper is the resonance curve and the smaller is the resonance frequency shift that can be detected. From the analysis made by Ekinci *et al*. on nanoelectromechanical systems, the dependence of the mass resolution with the square root of Q has been demonstrated[43].

$$\text{mass resolution} \propto \frac{m}{\sqrt{Q}} \qquad 1.5$$

The quality factor has an important physical meaning, being defined as the ratio between the stored energy and the energy losses per vibration cycle of the oscillator. Passing from vacuum to air and liquid, the values of Q can decrease from 10000-100000 to less than 10, due to the viscous losses of the medium where the oscillator moves. When the damping effect is low, the term $\sqrt{1-1/2Q^2}$ is negligible and the resonance frequency of the lowest flexural mode can be considered equal to the natural frequency f_0 of the resonator, (considering that $\omega = 2\pi f$)

$$f_0 = \frac{1}{2\pi}\sqrt{\frac{k}{m^*}} = \frac{1}{2\pi}\sqrt{\frac{E}{\rho}}\frac{t}{L^2} \qquad 1.6$$

In order to consider the influence of the resonator geometry on the resonance frequency, the oscillator mass m is substituted by the effective mass, m*, that is dependent both on the geometry and on the mode of resonance, as each portion of the oscillator moves differently at each mode.

In conclusion: considering the effect of the adsorbed molecules on the mass and the stiffness of the resonator, the resonance frequency shift can be expressed as:

$$\Delta f = \frac{f_n}{2}\left(\frac{\Delta k}{k}-\frac{\Delta m}{m_n^*}\right) \qquad 1.7$$

where m^*_n is the effective mass relative to the nth mode.

As can be seen, an increase of the beam stiffness leads to higher resonance frequency, while increasing the mass, the resonance frequency reduces, as also expressed by Figure 1.3c. The Eqn. 1.7 represents an approximated model, valid only for homogeneous molecular adsorption on the beam surface.

1.4 Issues concerning biological detection with MEMS

As already anticipated in § 1.3, the application of dynamic mode MEMS in the biological field is highly motivated by several advantaged in comparison with traditional detection methods, and a wide number of promising applications has been proposed. Nevertheless, so far their application in clinical work was rather limited, mainly due to specificity and reproducibility issues in a really complex environment as blood or serum. Ehwald's group developed a (MEMS)-based system for continuous glucose monitoring [44]and in Xu work an overview of electromechanical biosensors for pathogen detection is presented [45].
To obtain a successful application in the biomedical field, the following aspects have to be considered and properly managed:

- Influence of surface stress, stiffness and viscoelasticity changes on the mechanical behavior of the cantilever;
- Environment influence: in air and liquid the cantilevers have a less defined resonance curve as in vacuum, considerably reducing the resolution [14];
- Biological noise [7]

1.4.1 Factors influencing the cantilevers' mechanical behaviour

When a molecule adsorbs on a cantilever, in addition to the mass increase of the system, also other three mechanical quantities are modified: the surface stress, the viscoelasticity and the stiffness. These effects modify the mechanical behavior of the cantilever and, if not well managed, can lead to a difficult interpretation of the measurements[14].
For example, the deposition on the cantilever of a metal film, as substrate for biomolecular immobilization, can strongly influence the bending and should be taken into account; the elasticity of the deposited layer and its influence on the cantilever mechanical response should be verified. The difference in surface stress between the top and bottom side of the cantilever, the in-plane stresses near the clamp, as well as the viscoelasticity of the functionalization layer deposited on the cantilever, can induce frequency shifts, but their influence can often be neglected compared to mass and stiffness effects[14].
In general, stiffening effects are dominating close to the clamped end (or to the nodes at higher resonant modes), while on the free end of the cantilever (or on the antinodes at higher resonant modes), the mass effect is dominant. An example of this behavior is reported in Figure 1.3, taken from[46],where bacteria are deposited by ink-jet spotting along the cantilever, and the cantilever dynamic response is detected for each position. As shown, the resonance shift changes with the cell position inducing negative, null or positive resonance shifts.

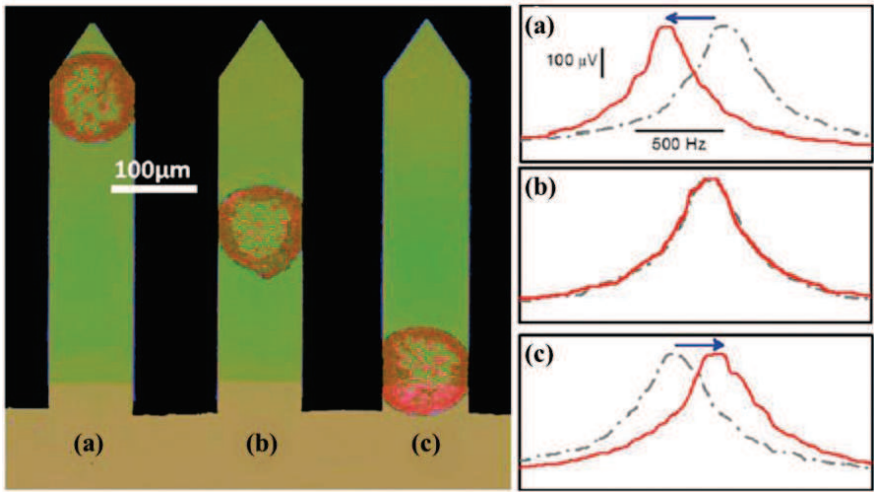

Figure 1.3 – *Effect of the position of bacteria deposited by ink-jet spotting along the cantilever: left side reports the optical image of bacteria deposited at the apex (a), in the middle (b) and at the base of a cantilever (c). Right side shows the corresponding resonance spectra due to Brownian motion of the three cantilevers in air before (dashed line) and after (continuous line) the bacteria deposition. Adapted from [46]*

Thus, in the case of not homogenous coating of the analyte on the cantilever, the mass contribution, and consequently, the resonance frequency shift, depends also on the position where the adsorption takes place. One approach to manage this issue, can be the measurement of at least two independent mechanical resonances, as proposed by Roukes' group in 2012. They demonstrated the use of a double clamped cantilever configuration as a nanomechanical mass spectrometer, in which the problem of the dependence of the resonance shift on the adsorption position was solved by measuring simultaneously the first two modes of vibration of the resonator[47].

Focusing on the dynamic mode operation, on which this work is referred, when also the stiffening effect on Eqn. 1.7 can be neglected, the resonance shift is only mass-dependent and the ratio

$$\frac{\Delta f}{\Delta m} = -\frac{1}{2}\frac{f_n}{m_n} \qquad 1.8$$

is defined as the mass sensitivity of the resonator. In order to increase both the mass resolution and the sensitivity to mass variations, common strategies are to reduce the mass of the system and increasing the resonance frequency by shrinking the resonator size or, alternatively, to operate the same sensor at higher resonance modes.

1.4.2 Influence of the environment

The biomolecular recognition and its effects on the biological events naturally happen in the physiological liquid environment, thus, the application of micro and nano resonators in this environment for real-time biological recognition would represent a significant advancement in the field of biological studies. Nonetheless, the application of such systems in liquid is limited by the strong damping effect due to the higher viscosity of the medium: the resonator experience a resistance to motion. The effects of this

phenomenon are: first, an additional "virtual mass" is introduced, which contributes to decrease the resonance frequency and so needs to be accurately evaluated prior to the quantification of the adsorbed biomolecular species; second, the further dissipative contribution dramatically reduces the quality factor and, consequently, limits the minimum resonance shift. As summarized by Tamayo at al. in [14], the performances of the cantilevers in air and liquid have not experienced the same improvements as in vacuum. As shown in figure 1.4, the detected mass is on the order of magnitude of femtogram in air and nanogram in liquid, far from the attogram reached in vacuum

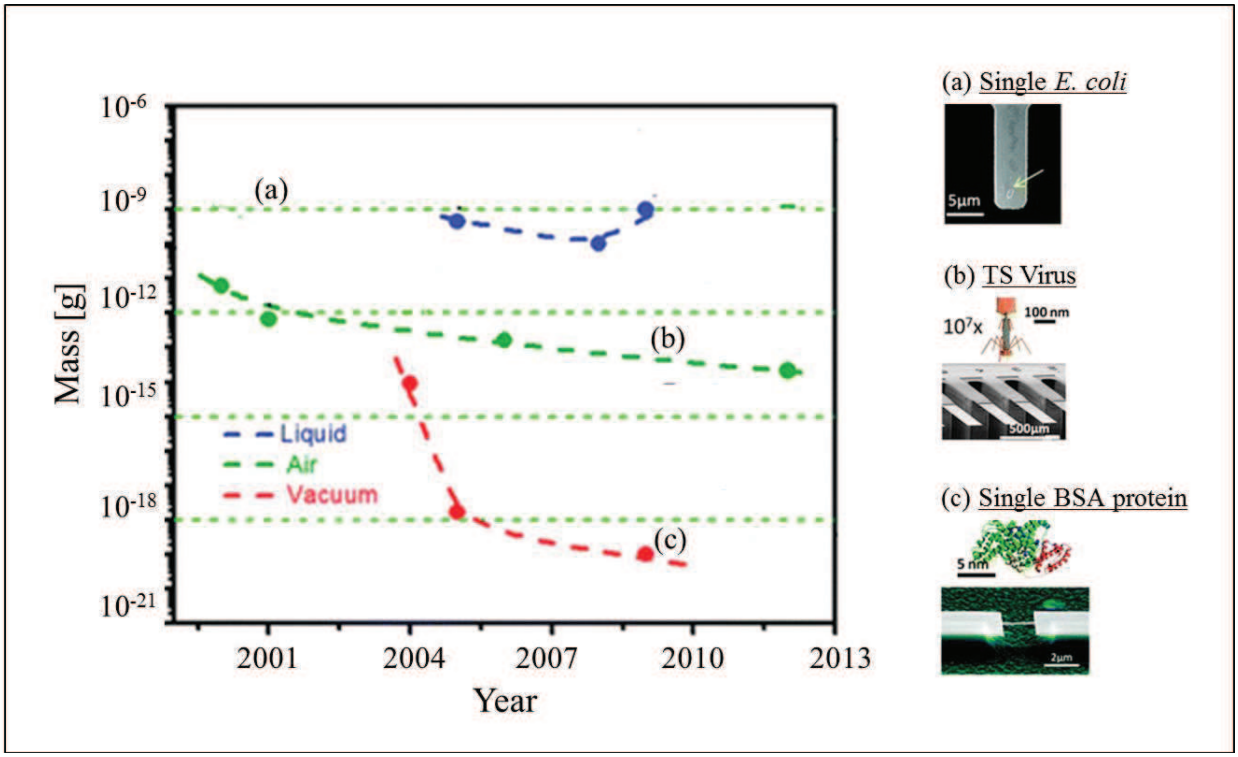

Figure 1.4 – *Chronology graph of the achievements in label-free biological detection based on nanomechanical resonators. The detected mass levels are plotted, the data split into measurements in vacuum(red), air(green) and liquid(blue). Measurements in vacuum show a high mass sensitivity that increased during the years till the attogram; measurements in air and liquid have always shown a minor mass sensitivity, reaching only femtogram and nanogram respectively in air and liquid. To the right side of the image, reference applications; image adapted from [14].*

In order to reduce the interaction of the resonator with the liquid, different approaches have been so far proposed, modifying the resonator geometry or its motion respect to the liquid medium.

- ***Microcantilever operation at higher resonance modes.*** It has been experimentally demonstrated that cantilevers operating at higher order modes both in air and in liquid show an increase of the quality factor and also the mass resolution[48, 49]. As direct application of this principle, Braun *et al*. in 2009 [8] used micron sized cantilevers for direct detection of T5 bacteriophage virus that binds to the Fhu-A membrane-protein receptor of *Escherichia Coli*. A detectable shift respect to the negative control was found at 300fM concentration, corresponding to an immobilized mass of almost 1ng; in the experiment by Ricciardi *et al*.[48], the microcantilever material and geometry were optimized to

maximize the Q factor using the fifth mode of actuation and used for real time monitoring of Angiopoietin-1, a protein involved in tumor angiogenesis.

- ***Suspended microchannel resonators***. This approach consists in flowing the analyte solution in a microfluidic channel fabricated within the resonator which can externally oscillate in vacuum maintaining high values of Q-factor (up to 15000)[50]. Such kind of resonator revealed to be a powerful instrument, showing mass resolution in the order of the attogram and finding applications in studies of biomolecular recognition, cell mass and density quantifications, and investigation of biological processes. An example of application of this technology is the work of Grover and co-workers [51].

- **Modification of the solid-liquid interactions.** In order to reduce the interaction of the resonator with the liquid, different approaches have been so far proposed, modifying the resonator geometry or its motion respect to the liquid medium. The best results have been obtained by fabricating cantilevers closely flanked by a fixed structure. In this way, the water surface tension forms a meniscus between the oscillating cantilever and the surrounding structure, reducing the liquid contact just to one side of the cantilever. The resonator is actuated at the first flexural mode and measured by optical lever detection, with the laser spot focused on the bottom of the cantilever. The authors used this platform to measure the resonance shift produced by the adhesion of a single latex bead demonstrating a mass detection limit of 30 fg[52].

When the detection in liquid is not possible, in most of the experiments reported in literature the so called "dip and dry" approach is used. The bioadsorption of the receptor and the target recognition are performed in liquid, while the measurement of resonance frequency is performed in air or in vacuum. Obviously, this technique does not allow a real time detection of biomolecular events, and studies of kinetics and molecular dynamics could be performed only with repeated experiments with different exposure times and measurements *a posteriori*. In addition, the rinsing and drying steps could induce spurious events on the sensor surface, as precipitation of salts from the solution or non-specific biomolecules adsorption that would alter the quantification of the adsorbed analyte and lead to false results[7, 48]; thus, as it is shown in Chapter 6, a strategy to minimize these effects has to be implemented.

1.4.3 Biological noise

The specificity and reproducibility issues in a really complex environment as blood or serum, is limited by the biological noise that induces nonspecific adsorption effects on the sensor, increasing the minimum detectable concentration respect to the intrinsic limit of the sensor. The concentration of the analyte of interest can be also billions of times lower than the most abundant species (the concentration of albumin, for example, is normally around 600 μM). To have an estimation of what can be the biological noise, Arlett and co-workers [7] reported an hypothetical example considering a target/receptor couple with binding affinity

$K_a^S \approx 10^{11}$ M^{-1}, while for non specific binding they assumed a rate of association $K_a^{NS} \approx 10^4$-10^5 M^{-1}; considering the concentration of albumin as the most prevalent, c_{prev} = 600 μM, a comparable number of specific and non specific binding sites, b_S and b_{NS} respectively, and a limit of detection that produces a signal to background ratio of 3:1, they estimated the biological noise floor c_{noise} as:

$$c_{noise} = 3\frac{c_{prev} b_{NS} K_a^{NS}}{b_S K_a^S} \qquad 1.9$$

which, for the above mentioned case, results in a noise level of ~ 1.8 nM.

The use of high affinity receptors strongly reduces the interaction with non specific molecules, but in any case biological noise is not avoidable. However, this limitation can be reduced, by adopting several improvements[7, 14]:

- **High density of functionalization:** as suggested by Nair and Alam on their model [53], high coverage of highly specific receptors (with density around 2 x 10^{12} molecules/cm^2) allows the target discrimination even in presence of much more abundant species;
- **Passivation of the functionalized surface:** after the receptor immobilization, filling of void portions with small inert molecules helps to reduce bio-fouling by non specific molecules and increases the specificity. In particular the most common passivating agents are polyethylene-glycol (PEG) and bovine serum albumin (BSA). PEG is used in the form of oligo-terminating short chains (3-6 monomer units) that assemble on the surface in a disordered configuration, increasing with the chain length. The mechanism of repellency is based on the fact that the protein adsorption would be associated with a loss of entropy on the OEG layer, making this process energetically not favored, as explained by Nelson and co-workers [54]. Instead, BSA is used for its low internal stability and its tendency to adsorb on all surfaces independently on the electrostatic interactions or the hydrophobic or hydrophilic nature of the substrate, with a gain in the conformational entropy due to adsorption[55].
- **Use of internal control reference:** the use of arrays of mechanical sensors allows to dedicate some of them as internal control: in this way, both the functionalized sensors and the controls are exposed to the same incubation conditions and the contribution of the biological noise (and also of other fluctuations due to fluid flow, temperature, etc.) can be easily subtracted. An example of this approach was reported by Braun *at al.* [49].
- **Sandwich assay:** as will be described in detail in Chapter 3, in order to increase both sensitivity and specificity, a further incubation step with a second receptor can be used: this receptor binds the target molecule on a different portion respect to the one used for the immobilization on the sensor, and is usually conjugated to a reporter (gold nanoparticles, dyes, fluorescent labels) that produces a detectable effect after the binding to the target.
- **Pretreatment of the sample:** in order to increase the ratio of the target molecules respect to the most abundant species, pre-concentration of the sample can be performed, for example through immunoaffinity depletion. Antibodies immobilized to a substrate or to nanoparticles are used to

capture the specific antigen from blood or serum; the formed complex is then recovered on a second step, by the detachment of the antibody from the substrate [56] or by the application of an external magnetic field, in the case of magnetic nanoparticles, as in the biobarcode assay[57]. Limitations related to this approach are the possibility that competing molecules are concentrated with the target or that the depletion of the most abundant species results also in depletion of the target molecules, as demonstrated for cytokines, which can be present in a complex with albumin in higher ratio respect to the free form.

The evaluation of sensors performances in terms of sensitivity and specificity (§1.1) are really important. However, the application of the presented approaches should be carefully evaluated, as an improvement of sensitivity can result also in a higher number of false positives, and vice versa. In addition, such treatments can also increase the complexity, the costs and the time required for the analysis, so a trade-off is necessary considering the specific requirements of the application [4].

1.5 The micropillar (a vertically oriented mechanical oscillator) technology

Vertically oriented mechanical oscillator were introduced for the first time in 2008 by the Oesterschulze's group [58] and they turned out to be a promising alternative to the horizontal cantilevers and double clamped beams. These vertical columnar resonators, with a top area of almost 10 x 15 μm^2, were obtained initially as isolated columns. figure 1.5a, and then fabricated inside a protective well, as shown in figure 1.5b. The use of these resonators, in dynamic mode, as mass sensors was demonstrated by the Oesterschulze's group measuring the shift induced by silica beads deposited on the top area, providing a mean sensitivity around 0.8 Hz/fg; they also measured the influence of different gases on the resonance shift and the damping behavior[59, 60].

In 2010, in our research group, smaller vertical resonators , named micropillars, with a top area of 3x8 μm^2(Figure 1.5c) were exploited by Melli to fabricate a new type of fast and sensitive mechanical biosensor[61]. All details about the fabrication process and characterization are reported in Chapter 2.

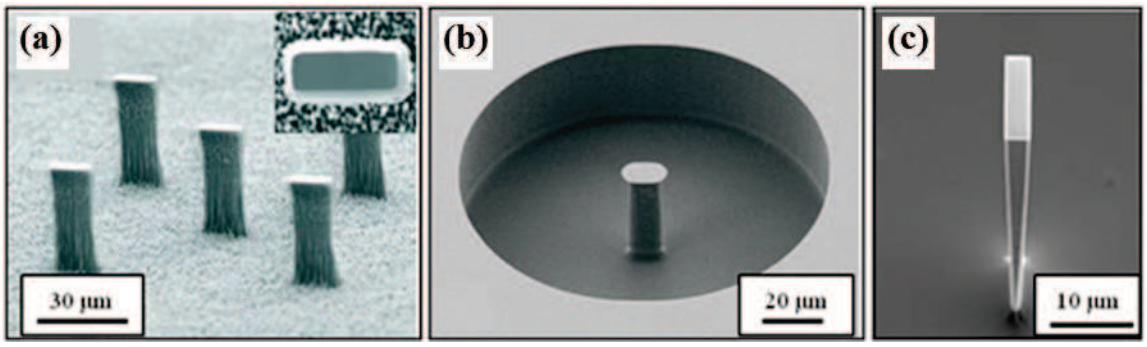

Figure 1.5 – *SEM images of different examples of vertical silicon resonators: (a,b) large, isolated pillars fabricated in Oesterchulze's group; (c) smaller, tapered silicon resonator obtained by Melli. Adapted from [58](a), [59](b) and [61](c).*

Thanks to their geometry, micropillars better embody the advantages offered by vertical mechanical resonators; indeed, they can solve some of the problems observed applying horizontal cantilever for biological application and exposed in §1.4

Because of the reduced lateral size, pillars can be fabricated in very dense array (up to thousands per mm^2),as shown in figure 1.6 . As result, the highly packed configuration results in a rough surface that coupling with a proper lateral surfaces functionalization with hydrophobic-terminated molecules enables to obtain a superhydrophobic Cassie-Baxter state; a detailed description of this effect is reported in Chapter 2. Operating in the superhydrophobic state ensures that the biochemical recognition process occurs only on the top. Thus the non-specific adsorption on the lateral wall is drastically reduced and consequently also the deterioration of the devices, such as stress inductions or changes in the elastic constant of the resonator. Moreover, the availability of high density array also means the possibility of highly parallel detection of the adsorbed biomolecules, thus, as will be shown in Chapter 4, micropillar array represent also a suitable platform to implement multiplexing detection[62].

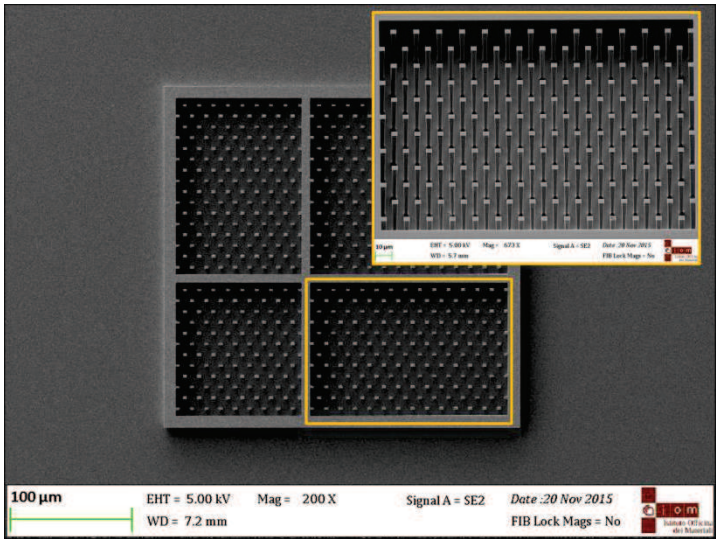

Figure 1.6 – *SEM image, top view of an pillars array; the inset shows a magnification of a tilted view in which the intere body of pillar is visible.*

The most important advantage offered by tapered shape micropillars design is that allows the selective deposition of gold (used as a substrate for the immobilization of thiolated receptor molecules) on the top of the pillars (and on the bottom floor of the matrix). Thus the localized and small adsorption area, the top of the pillars, is the only one that interacts with the liquid, allowing a faster kinetic of adsorption compared to larger, planar sensors. This improved dynamic was demonstrated by Melli in 2011, by studying the kinetic of formation of a self-assembled monolayer of thiolated, single strand DNA (SH-ssDNA) and the hybridization efficiency[63]. The main results are reported in Figure 1.7.

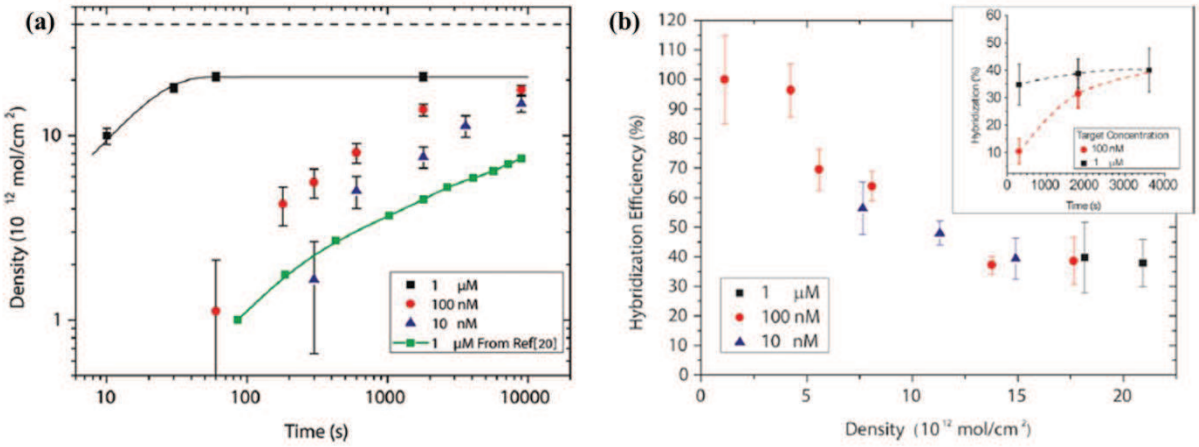

Figure 1.7 – *(a) Comparison of kinetics of diffusion of thiolated DNA on pillars at different concentrations (black, red and blue markers) respect to the output of SPR: at the same concentration, the saturation of the sensitive area is reached in 3 order of magnitude less time. (b) Hybridization efficiency of micropillars as a function of the SAM density: the inset shows the results of two different concentrations, showing that even al 100 nM concentration of the complementary DNA, the maximum efficiency is reached in one hour. Adapted from[63].*

He found that, at 1 µM concentration of SH-ssDNA, 1 minute of incubation was enough to reach the saturation of the top area of pillars, with a calculated density of $2.1 \pm 0.1 \times 10^{13}$ mol/cm^2. In comparison, the same concentration on the flat, larger surface of a Surface Plasmon Resonator (SPR) led to a lower coverage, even after more than three hours .

This different behavior was explained considering that on pillars molecules can diffuse from a spherical volume. Indeed, the linear dimension of the top area of the pillars is comparable to the molecular diffusion length and the sensitive area is surrounded by non-adsorbing areas, since the neighboring pillars are separated by a significantly larger distance. On the contrary, on the planar sensor, diffusion occurs in a columnar volume, requiring a longer path for molecules to reach and saturate the surface. This is consistent with the analysis reported by Nair *et al.* regarding 3D diffusion on nanosized sensors[64].

1.6 Scope of the project

The aim of this project is to exploit the advantages of the micropillars approach for the development of a high sensitive and multiplexing biosensor.

The first part of the activities was focused on the improvement of the mass detection limits, using an approach in which functionalized nanoparticles act as a secondary molecular recognition in sandwich-like assays, thus significantly amplifying the detected mass. This approach has been tested on a biotin-streptavidin system.

The second part of the work was focused on the development of a multiple detection approach, that involves two main aspects: the individual functionalization of sensors with different molecular probes, based on

photocleavable chemistry and an optical parallel detection method to measure simultaneously a wide number these sensors.

Finally, the above mentioned approaches have been applied to a case of clinical interest: the detection of Prostate Membrane Specific Antigen (PSMA), a promising alternative biomarker compared to Prostate Specific Antigen (PSA) to better distinguish patients with prostate cancer respect to other diseases.

References:

[1] K.M. Song, S. Lee, C. Ban, Aptamers and Their Biological Applications, Sensors, 12(2012) 612-31.
[2] S. Song, L. Wang, J. Li, C. Fan, J. Zhao, Aptamer-based biosensors, TrAC Trends in Analytical Chemistry, 27(2008) 108-17.
[3] K.M. Goeders, J.S. Colton, L.A. Bottomley, Microcantilevers: sensing chemical interactions via mechanical motion, Chemical reviews, 108(2008) 522-42.
[4] N. Fracchiolla, S. Artuso, A. Cortelezzi, Biosensors in Clinical Practice: Focus on Oncohematology, Sensors, 13(2013) 6423-47.
[5] E.B. Bahadir, M.K. Sezginturk, Applications of commercial biosensors in clinical, food, environmental, and biothreat/biowarfare analyses, Analytical biochemistry, 478(2015) 107-20.
[6] P. D'Orazio, Biosensors in clinical chemistry - 2011 update, Clinica chimica acta; international journal of clinical chemistry, 412(2011) 1749-61.
[7] J.L. Arlett, E.B. Myers, M.L. Roukes, Comparative advantages of mechanical biosensors, Nature nanotechnology, 6(2011) 203-15.
[8] D. Falconnet, J. She, R. Tornay, E. Leimgruber, D. Bernasconi, L. Lagopoulos, *et al*., Rapid, sensitive and real-time multiplexing platform for the analysis of protein and nucleic-acid biomarkers, Analytical chemistry, 87(2015) 1582-9.
[9] B.H. Shadfan, A.R. Simmons, G.W. Simmons, A. Ho, J. Wong, K.H. Lu, *et al.*, A multiplexable, microfluidic platform for the rapid quantitation of a biomarker panel for early ovarian cancer detection at the point-of-care, Cancer prevention research, 8(2015) 37-48.
[10] M. Mirasoli, F. Bonvicini, L.S. Dolci, M. Zangheri, G. Gallinella, A. Roda, Portable chemiluminescence multiplex biosensor for quantitative detection of three B19 DNA genotypes, Analytical and bioanalytical chemistry, 405(2013) 1139-43.
[11] P. Chen, M.T. Chung, W. McHugh, R. Nidetz, Y. Li, J. Fu, *et al.*, Multiplex serum cytokine immunoassay using nanoplasmonic biosensor microarrays, ACS nano, 9(2015) 4173-81.
[12] Z. Wang, N. Liu, Z. Ma, Platinum porous nanoparticles hybrid with metal ions as probes for simultaneous detection of multiplex cancer biomarkers, Biosensors & bioelectronics, 53(2014) 324-9.
[13] I.A. Estrada, *et al.*, Multiplex detection of pathogen biomarkers in human blood, serum, and saliva using silicon photonic microring resonators, Proc SPIE 9490, Advances in Global Health through Sensing Technologies 2015, (2015).
[14] J. Tamayo, P.M. Kosaka, J.J. Ruz, A. San Paulo, M. Calleja, Biosensors based on nanomechanical systems, Chemical Society reviews, 42(2013) 1287-311.
[15] A.P. Turner, Biosensors: sense and sensibility, Chemical Society reviews, 42(2013) 3184-96.
[16] Y. Tian, M.J. Cuneo, A. Changela, B. Hocker, L.S. Beese, H.W. Hellinga, Structure-based design of robust glucose biosensors using a Thermotoga maritima periplasmic glucose-binding protein, Protein science, 16(2007) 2240-50.
[17] Y. Wang, H. Xu, J. Zhang, G. Li, Electrochemical Sensors for Clinic Analysis, Sensors, 8(2008).
[18] G. Zheng, F. Patolsky, Y. Cui, W.U. Wang, C.M. Lieber, Multiplexed electrical detection of cancer markers with nanowire sensor arrays, Nature biotechnology, 23(2005) 1294-301.
[19] A. Kim *et al.*, Ultrasensitive, label-free, and real-time immunodetection using silicon field-effect transistors, Applied physics letters, 91(2007) 103901.
[20] A. Gao *et al.*, Silicon-nanowire-based CMOS-compatible field-effect transistor nanosensors for ultrasensitive electrical detection of nucleic acids, Nano letters, 11(2011) 3974-8.
[21] F. Zhou, Z. Li, Z. Bao, K. Feng, Y. Zhang, T. Wang, Highly sensitive, label-free and real-time detection of alpha-fetoprotein using a silicon nanowire biosensor, Scandinavian journal of clinical and laboratory investigation, 75(2015) 578-84.
[22] W.S. Kim, G.J. Lee, J.H. Ryu, K.C. Park, H.K. Park, A flexible, nonenzymatic glucose biosensor based on Ni-coordinated, vertically aligned carbon nanotube arrays, RSC Adv, 4(2014).
[23] L. Zhu, C. Deng, P. Chen, X. You, H. Su, Y. Yuan, M. Zhu, Glucose oxidase biosensors based on carbon nanotube non-woven fabrics, Carbon, 7(2014).
[24] X. Fan, I.M. White, S.I. Shopova, H. Zhu, J.D. Suter, Y. Sun, Sensitive optical biosensors for unlabeled targets: a review, Analytica chimica acta, 620(2008) 8-26.

[25] X. Yao *et al.*, Sub-attomole oligonucleotide and p53 cDNA determinations via a high-resolution surface plasmon resonance combined with oligonucleotide-capped gold nanoparticle signal amplification, Analytical biochemistry, 354(2006) 220-8.
[26] J.B. Fasoli, R.M. Corn, Surface Enzyme Chemistries for Ultrasensitive Microarray Biosensing with SPR Imaging, Langmuir, 31(2015) 9527-36.
[27] M.D. Baaske, M.R. Foreman, F. Vollmer, Single-molecule nucleic acid interactions monitored on a label-free microcavity biosensor platform, Nature nanotechnology, 9(2014) 933-9.
[28] A. Afzal, N. Iqbal, A. Mujahid, R. Schirhagl, Advanced vapor recognition materials for selective and fast responsive surface acoustic wave sensors: a review, Analytica chimica acta, 787(2013) 36-49.
[29] C.K. O'sullivan, G.G. Guilbault, Commercial quartz crystal microbalances – theory and applications, Biosensors & bioelectronics, 14(1999).
[30] C.I. Cheng, Y.P. Chang, Y.H. Chu, Biomolecular interactions and tools for their recognition: focus on the quartz crystal microbalance and its diverse surface chemistries and applications, Chemical Society reviews, 41(2012) 1947-71.
[31] X.L. Feng, R. He, P. Yang, M.L. Roukes, Very High Frequency Silicon Nanowire Electromechanical Resonators, Nano letters, 7(2007).
[32] Y. Lu, S. Peng, D. Luo, A. Lal, Femtomolar sensitivity DNA photonic crystal nanowire array ultrasonic mass sensor, Micro Electro Mechanical Systems (MEMS), 2012 IEEE 25th International Conference, (2012).
[33] J. Chaste *et al.*, A nanomechanical mass sensor with yoctogram resolution, Nat Nanotechnol, 7(2012).
[34] S. Sawano, T. Arie, S. Akita, Carbon nanotube resonator in liquid, Nano letters, 10(2010) 3395-8.
[35] S. Fanget *et al.*, Gas sensors based on gravimetric detection—A review", Sensors Actuators B Chem, 160(2011).
[36] W. Pang, H. Zhao, E.S. Kim, H. Zhang, H. Yu, X. Hu, Piezoelectric microelectromechanical resonant sensors for chemical and biological detection, Lab on a chip, 12(2012).
[37] J. Tamayo, J.J. Ruz, V. Pini, P. Kosaka, M. Calleja, Quantification of the surface stress in microcantilever biosensors: revisiting Stoney's equation, Nanotechnology, 23(2012) 475702.
[38] J. Fritz *et al.*, Translating biomolecular recognition into nanomechanics, Science, 288(2000).
[39] G. Wu *et al.*, Bioassay of prostate-specific antigen (PSA) using microcantilevers, Nat Biotechnol, 19(2001) 856–860.
[40] J.W. Ndieyira *et al.*, Surface-stress sensors for rapid and ultrasensitive detection of active free drugs in human serum, Nat Nanotechnol, 9(2014).
[41] B.N. Johnson, R. Mutharasan, Biosensing using dynamic-mode cantilever sensors: a review, Biosens Bioelectron, 32(2012).
[42] N. Lobontiu, Dynamics of Microelectromechanical systems, Springer (2007).
[43] K.L. Ekinci, Ultimate limits to inertial mass sensing based upon nanoelectromechanical systems, J. Appl. Phys. 95, 2682 (2004)
[44] M. Birkholz *et al.*, Sensing glucose concentrations at GHz frequencies with a fully embedded Biomicro-electromechanical system (BioMEMS), J. Appl. Phys. 113, 244904 (2013)
[45] S. Xu, Electromechanical biosensors for pathogen detection: a review, Microchim Acta, 178(2012).
[46] D. Ramos *et al.*, Origin of the response of nanomechanical resonators to bacteria adsorption J. Appl. Phys. 100, 106105 (2006)
[47] M.S. Hanay *et al.*, Single-protein nanomechanical mass spectrometry in real time, Nature Nanotechnology 7, 602–608 (2012)
[48] C. Ricciardi, G. Canavese, R. Castagna, I. Ferrante, A. Ricci, S.L. Marasso, *et al.*, Integration of microfluidic and cantilever technology for biosensing application in liquid environment, Biosensors & bioelectronics, 26(2010) 1565-70.
[49] T. Braun *et al.*, Quantitative time-resolved measurement of membrane protein-ligand interactions using microcantilever array sensors, Nature nanotechnology, 4(2009) 179-85.
[50] T.P. Burg, Vacuum-Packaged Suspended Microchannel Resonant Mass Sensor for Biomolecular Detection, J Microelectromechanical Syst, 15, 1466 - 1476 ,(2006).
[51] W.H. Grover, A.K. Bryan, M. Diez-Silva, S. Suresh, J.M. Higgins, S.R. Manalis, Measuring single-cell density, Proceedings of the National Academy of Sciences of the United States of America, 108(2011) 10992-6.

[52] J. Linden, E. Oesterschulze, Improving the quality factor of cantilevers in viscous fluids by the adaptation of their interface, Appl. Phys. Lett. 100, 113511 (2012).
[53] P.R. Nair, M.A. Alam, Theory of "Selectivity" of label-free nanobiosensors: A geometro-physical perspective, Journal of applied physics, 107(2010) 64701.
[54] K.E. Nelson *et al.*, Surface Characterization of Mixed Self-Assembled Monolayers Designed for Streptavidin Immobilization, Langmuir, 17 (2001), 2807–2816
[55] K. Nakanishi, T. Sakiyama, K. Imamura, On the adsorption of proteins on solid surfaces, a common but very complicated phenomenon, Biosci Bioeng, 91(2001).
[56] E. Stern *et al.*, Label-free biomarker detection from whole blood, Nature nanotechnology, 5(2010) 138-42.
[57] J.M. Nam, C.S. Thaxton, C.A. Mirkin, Nanoparticle-based bio-bar codes for the ultrasensitive detection of proteins, Science, 301(2003) 1884-6.
[58] J. Kehrbusch, E. A. Ilin, M. Hullin, E. Oesterschulze, High frequency columnar silicon microresonators for mass detection, Appl Phys Lett, 93(2008).
[59] J. Kehrbusch *et al.*, High-frequency micromechanical columnar resonators, Sci. Technol. Adv. Mater. 10 (2009) 034601
[60] J. Kehrbusch *et al.*, Columnar shaped microresonators for mass detection and gas analysis, Microelectron Eng, 87(2010).
[61] M. Melli, A. Pozzato, M. Lazzarino, Inverted tapered pillars for mass sensing, Microelectronic engineering, 87(2010) 730-3.
[62] M. Tardivo *et al.*, Parallel optical read-out of micromechanical pillars applied to prostate specific membrane antigen detection, Biosensors & bioelectronics, 72(2015) 393-9.
[63] M. Melli, M. Lazzarino, G.Scoles, Fast detection of biomolecules in diffusion-limited regime using micromechanical pillars, ACS Nano, 2011, 5 (10), 7928–7935
[64] P.R. Nair, M.A. Alam, Performance limits of nanobiosensors, Applied physics letters, 88(2006) 233120.

Chapter 2

Micropillars devices: fabrication and characterization

This chapter is organized in two subsections: the first part outlines the processes and the protocols used in the micropillars device fabrication, from the microfabrication to the surface treatment; the second part is focused on the devices characterization, the evaluation of the wettability in superhydrophobic configuration, and the measurement of the resonance frequency and sensitivity. Reference values that define the quality of the processes are also provided.

2.1 Fabrication of ready-to-use micropillars devices

The fabrication of a *ready-to-use* micropillars device involves three phases, schematised in figure 2.1:

- the definition of the geometrical structure of the pillars starting from a plain silicon wafer, consisting in lithographic patterning and plasma etching steps;
- the surface treatment, that ensures a Cassie-Baxter superhydrophobic state;
- the surface sensors (top of pillar) treatment for the further development of a proper bio-recognition layer.

Starting from the first protocol developed by Mauro Melli [1], both the microfabrication procedures and the superhydrophobicity functionalization strategy have been further improved mainly by Daniele Borin. All details regarding the optimization are reported in their Ph.D thesis and in [2]. Here the final adapted protocols are described.

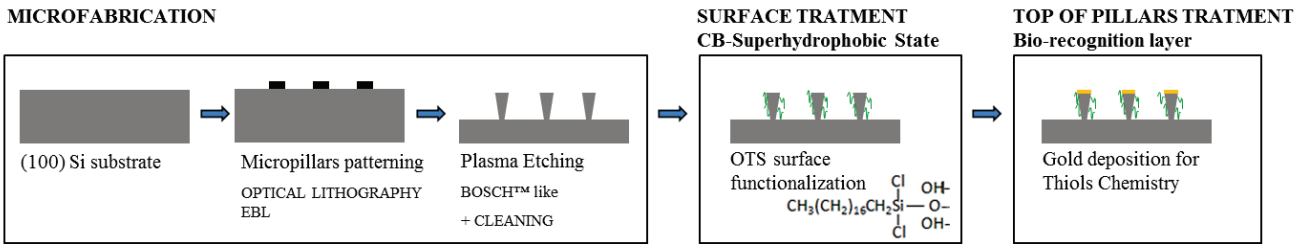

Figure 2.1 – *Schematic representation of the 3-phases involved in the development of a ready-to-use micropillars device. Microfabrication consists in micropillars patterning on a silicon substrate and etching. After that, surfaces are chemically treated to obtain a Cassie-Baxter superhydrophobic state and finally, sensors surfaces (top of pillars) are treated to enable the further development of a bio-recognition interface.*

These devices have a relatively low production costs, also in a prototypal stage; therefore they are used as produced, and then disposed.

2.1.1 Microfabrication

The processes involved in the top-down micropillars fabrication are well known and commonly used in integrated circuitry industry. In particular, micropillars are obtained by a deep dry etching of a patterned Si wafer, followed by a cleaning phase. Here below, an overview of the pattering and etching principles is given, while detailed procedures and used parameters are outlined in §2.1.1.1.

- **Micropatterning:**

  As schematically shown in figure 2.2, the micropatterning operation is used to transfer the desired pattern on the substrate, creating protected and exposed areas. This operation can be performed by optical or Electron Beam Lithography- EBL.

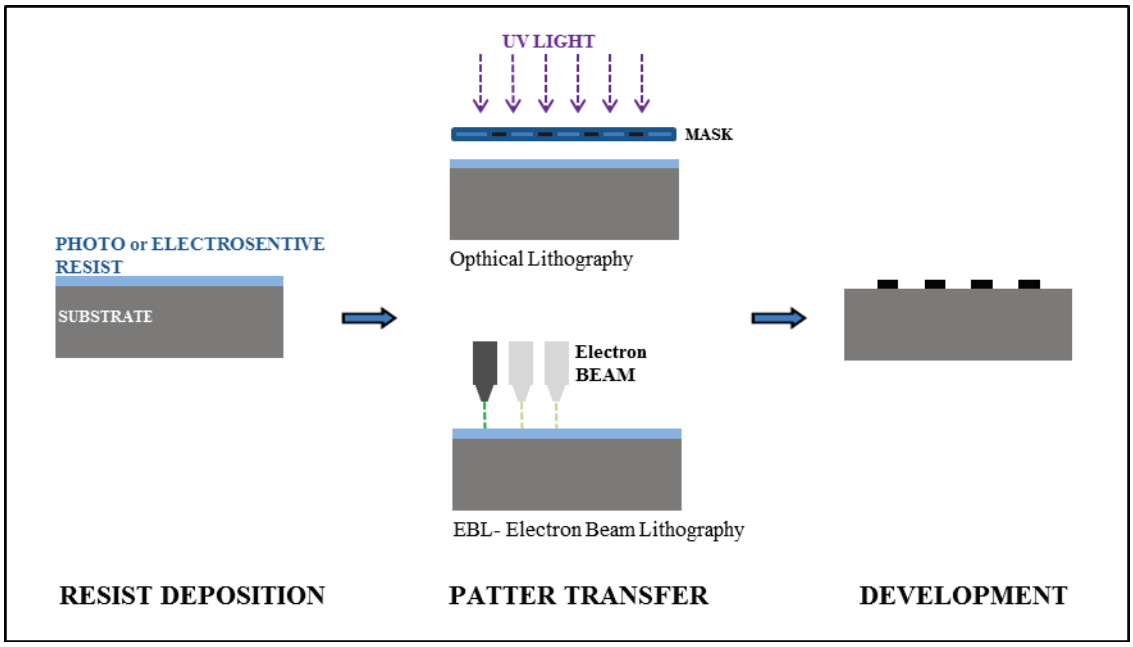

Figure 2.2 – *Schematic representation of the operations involved in the micropatterning process. First a resist is deposited on the substrate; afterwards, through UV laser or electron beam, the patterning is transferred; finally, the soluble portions of the resist is removed by the immersion in a Developer.*

When optical lithography is used, a polymeric photosensitive layer (photoresist) is deposited (usually by spin coating), on the substrate, and the pattern is transferred from an optical mask to the substrate by ultraviolet light exposure and subsequent removal of the exposed areas. The mask is made of silica or quartz glass with a thin metallic pattern (usually chromium) that screens the transmission of light on specific areas, that represent the negative (or the positive) of the desired pattern[3]. Instead, in case of Electron Beam Lithography, the wafer is coated with a thin layer of an electron-sensitive resist and the pattern is realized by directly writing through electromagnetically focused scanning electron beam[4]. In both cases the photon or electron exposure generates a structural change on the exposed part, leading to a change in solubility. Thus, after exposure (and eventually post-bake

treatment), the substrate is immersed in a specific solution (named Developer), to remove the soluble portions of the resist, obtaining on the substrate the desired protected/unprotected areas. The photoresist can be positive or negative: in the first case the photoresist becomes soluble on the exposed areas, while in negative resists the not illuminated areas are removed by the developer.
As explained in detail in §2.1.1.1, in order to perform the following etching step, the pattern it is not transferred directly on silicon but on a metal (Cr or Ni) which acts as a mask during the etching.

- **Plasma etching:**

With the etching process the two-dimensional pattern of the metal mask layer is transferred to the substrate (Silicon), by removing the excess of material in the unprotected areas. Based on the physical state of the reactant, etching can be distinguished in wet and dry processes; here only the latter is considered.
In a dry etching, the reaction is performed in vacuum in a gaseous atmosphere of etchant species, that can be molecules or excited/ion species created by plasma, so that this process can be also defined Reactive Ion Etching (RIE). These species react with the material to be removed, transforming silicon or its derivatives in products that are volatile at room temperature and mTorr pressure. For example, silicon reacts with fluorine (sulfur hexafluoride (SF_6) or tetrafluoromethane (CF_4)) to produce silicon fluorides (SiF_4),. The reaction rate and its directionality are controlled by the chamber pressure, the reagents flow rates, the temperature and the generated electrical field[3]. When deeper and steep-sided structures have to be created, as in case of micropillar fabrication, a specific type of Dry etching is used, named Deep Reactive Ion Etching (DRIE). The most common example of DRIE is represented by the Bosch^{TM} process (patented in 1994)[5]. It consists of repeated cycles of etching (based on SF_6 chemistry) and passivation, obtained by uniform deposition of a fluoropolymer thin film (CF4).

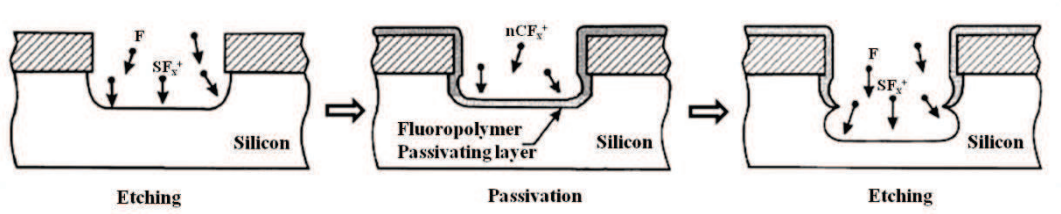

Figure 2.3 – *Representation of the Bosch-based deep reactive ion etching (DRIE) process. The repetition of passivation and etching steps results in undulated side-walls. Adapted from http://www.tf.uni-kiel.de/matwis/amat/semitech_en/kap_7/backbone/r7_2_2.html*

During etching, due to the almost vertical ion bombardment, on the bottom the passivation layer is removed and silicon is etched, while on lateral walls the ion bombardment should not be effective. This cyclic process results in undulated or scalloped side-walls, as reported in figure 2.3. Actually, due to the not perfect anisotropy of the process, a small undercut or overcut is unavoidable.

One of the most important value to describe the quality of the process is the aspect ratio, i.e. the ratio between the height of the etched structure and the lowest lateral dimension. The minimum feature size strongly depends on the thickness of the layer to be patterned. The thicker the substrate to be etched, the thicker has to be the mask to endure the longer etching time. But the longer the etching time, the bigger can be the underetching due to lateral silicon etching even below the masked areas. Plasma DRIE processes allow to obtain easily aspect ratio of 10:1[6].

2.1.1.1 Micropillars fabrication protocols

To allow a production in standard and reproducible conditions, all operations were performed in a clean room environment (class 10-1000)[7], characterized by controlled temperature, illumination, humidity and environmental dust density.

- **Micropatterning**

As already anticipated, micropillars patterning has been developed both with photolithography and electron beam lithography. The dimensions of the figures patterned in this stage reflect the base of the final vertical structure and thus the resonance properties. To drive pillars to oscillate with a well-defined first resonance mode, that is orthogonal to the longer edge, the minimum ratio between the two dimensions of the patterned figure (the longer edge over the shorter one) is set to 1.5. Indeed, below this value, the base of the vertical structure goes towards a cylindrical form, the resonance still occurs along an unique direction but it is less controllable along which one. Thus, with EBL structures of 2x3μm have been patterned. Using optical lithography, due to the lower resolution limit and considering also the rounded corners (see figure 2.4b), a ratio of 2 is assumed and structures of 2x4μm are patterned. In general, the variability of the structures obtained by optical lithography is higher, spreading the resonance frequency of pillars in a wider range, while EBL allows a resolution below 10 nm, depending mainly on the resist properties. The main drawback of EBL is the expensive machinery required and the extremely low throughput, as the required time is proportional to the patterned area. Nonetheless, when possible electron beam lithography was preferred to photolithography.

- **Photolithographic patterning**

A schematic representation of the detailed photolithographic patterning protocol is illustrated in Figure 2.3a. As preliminary step, a layer of 100 nm of chromium is deposited on a silicon wafer by sputtering. In order to promote the adhesion of the photoresist to chromium, a thin layer of hexamethyldisilazane (HMDS, Microchemicals GmbH) is deposited by spin coating at 5000 rpm for 30 s and then baked at 115 °C for 1 minute. Then, the positive photoresist MEGAPOSIT ™ SPR ™ 220 1.2 (Dow Chemical, US) is spun at 4500 rpm for 30 s and soft baked at 115 °C for 90 s, producing a resist layer of almost 1 μm of

thickness. The wafer is loaded on a mask aligner and put in contact with an optical chromium mask (Deltamask, NL) where lattices of full rectangles of 2x4 µm and fixed distance were patterned. The wafer is exposed to UV light source (usually a mercury lamp with main lines at 365.4, 404.7 and 435.8 nm), for 4.5 s , after that a post baking for 90 s at 115 °C is performed.

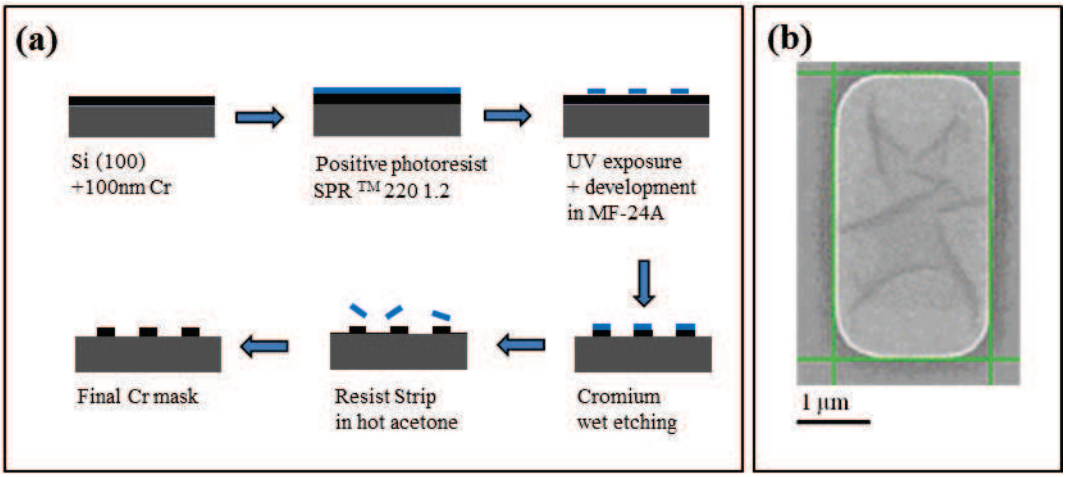

Figure 2.4 – *(a) Schematic representation of the micropillars array patterning by optical lithography. (b) SEM image of the resulting mask shape after wet etching of chromium and removal of the residual resist.*

The development is performed by dipping the wafer for 30s in MF-24A developer (MEGAPOSIT, Dow Chemical, US), a solution based on tetramethylammonium hydroxide that removes the resist from the areas exposed to UV light. Finally, the unprotected chromium is etched for 1 min in a solution based on acetic acid and cerium ammonium (CH_3COOH 1M, $Ce(NH_4)_2(NO_3)_6$ 0.55M) and the residual resist over chromium is stripped by hot acetone. A top view of the final chromium mask available for the subsequent dry etching is shown in Figure 2.4b.

- Electron Beam Lithography patterning

A schematic representation of the steps involved in micropillars patterning by electron beam lithography is shown in Figure 2.5a. A 500 nm layer of polymethyl methacrylate-PMMA 950K electronic resist is spun on the silicon wafer at 5000 rpm for 1 minute and baked at 180 °C for 10 minutes. Lattices made of rectangles of 2x3µm and fixed distance are patterned through electron beam lithography (EBL). In particular, electronic gun is actuated at 30 keV and the proper exposure parameters are determined by a dose matrix study. The optimal conditions used are an area step size of 80 nm and a dose factor of 280 $pA \cdot s/cm^2$. In this conditions, a sharp rectangular shape is obtained, as illustrated in Figure 2.5b.

After exposure, the wafer is developed on a mixture of methylisobutylketone (MIBK) : isopropyl alcohol (IPA) 1:3 for 40 s and then for few seconds on a 1:1 solution of the two, leaving the wafer with rectangular holes in correspondence of the exposed areas.

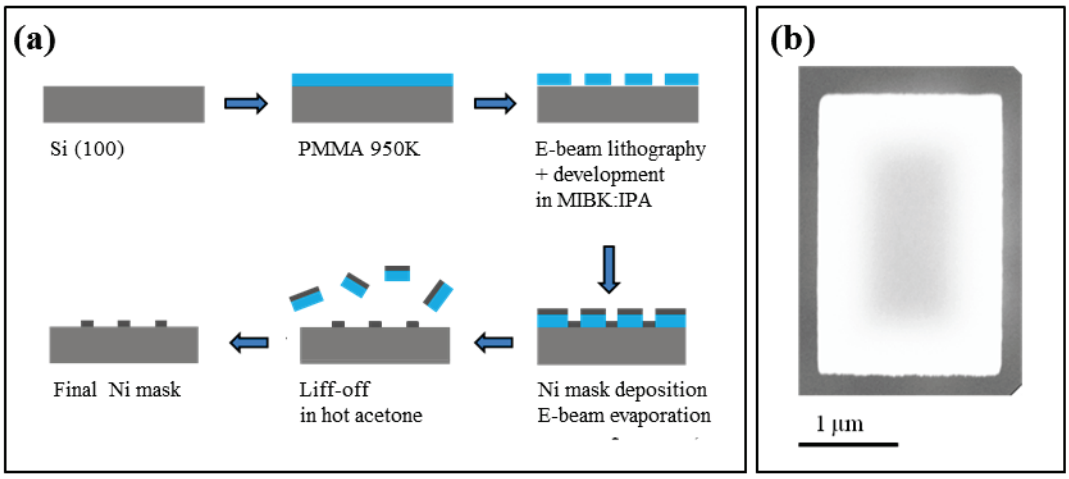

Figure 2.5 – *(a) Schematic representation of the micropillar patterning procedure by electron beam lithography. (b) SEM image of the sharp rectangular Ni mask obtained after the EBL and lift-off processes.*

A thin (20 nm) nickel mask is deposited on the patterned wafer by e-beam evaporation and the following removal of remaining PMMA in hot acetone (Lift-off) provides the wafer with small rectangles of Ni for the dry etching.

▪ Dry plasma Etching: a Bosch-like process

Deep plasma etching of pillars is performed within an Inductively Coupled Plasma (ICP) reactor, where a coil on the upper part of the chamber undergo a time-varying electric current, generating a variable magnetic field, that induces an electric field within the chamber, generating discharges and the creation of the plasma. The reactive species are accelerated toward the wafer by a bias created with the plate at the bottom of the chamber.

As preliminary steps, the patterned wafer is exposed to a short oxygen plasma to remove the residuals of resist and to an argon milling treatment to better define the edges of the Ni or Cr mask; process parameters are reported in table 2.1.

Gas	Time [s]	Gas flow rate [sccm]	Power [W]	
			Coil	Platen
O_2	20	40	10	200
Ar	15	30	30	450

Table 2.1 – *Dry etching process.* *Parameters for preliminary step of oxygen plasma and argon milling.*

After that, a vertical anisotropic etching is obtained using a BOSCH™-like process; 33 cycles of passivation (based on C_4F_8) and etching (SF_6) are executed with the parameters reported in table 2.2 . Etching step is performed with a mixture of SF_6 and Ar, while in the passivation a mixture of octafluorocyclobutane (C_4F_8) and Ar is used. In the etching step Ar is introduced to improve the removal of the passivation layer from the bottom of the etched surface and to increase the directionality of etching; during the passivation it increases the plasma stability [8]. Moreover, a positive ramp is introduced during the passivation, thus, as discussed in §2.1.1.2, tapered structures with a vertical undercut confined only on the upper part are obtained.

STEP	Time [s]	Ramp [s]	Bias [V]	Gas flow rate [sccm]		Power [W]	
						Coil	Plate
PASSIVATION	10	0.3	190	C_4F_8	Ar	600	50
				100	20		
ETCHING	18	-	140	SF_6	Ar	600	50
				110	20		

Table 2.2 – *Etching and passivation recipes used for deep plasma etching of micropillars.*

- **Cleaning**

Once etched, micropillars are exposed again to an oxygen plasma cleaning (50 sccm, plate power = 800 W, coil power = 20 W, 2 min) in order to remove the fluorocarbon film deposited on the lateral walls during the passivation steps. The metal mask and the eventual organic residuals are removed by dipping the wafer in hot piranha solution (H_2SO_4 (48%):H_2O_2 (30%) mixed in a 7:3 volume ratio, at 70°C for 15 minutes). The superficial layer of silicon dioxide formed during the oxygen plasma and the exposure to the strongly oxidant piranha is removed by dipping the sample in Buffered Oxide Etchant (BOE, 7:1 volume ratio of 40% NH4F to 49% HF in water) for 1 min, obtaining a clean silicon surface on the whole pillar. The fabricated arrays are then rinsed in deionized water and dried under mild nitrogen flux.

2.1.1.2 Result of the microfabrication process

The microfabrication processes results in 5x5mm^2 silicon chips with a 300x300 µm^2 patterned area containing an array of 640 pillars. Figure 2.6a shows a SEM image of a slightly tilted pillars array. The frame surrounding the whole matrix has the purpose to protect the array from mechanical damaging and avoid the wetting of the matrix from the sides, once the array is fully immersed in liquid during incubation step. The four quadrant structure is also made for a practical issue: four independent matrix are available, preserving a part of the array in case of damage of another one.

Each pillars matrix consists of an hexagonal distribution of 2x 3µm pillars with a center-to-center distance of 12µm.

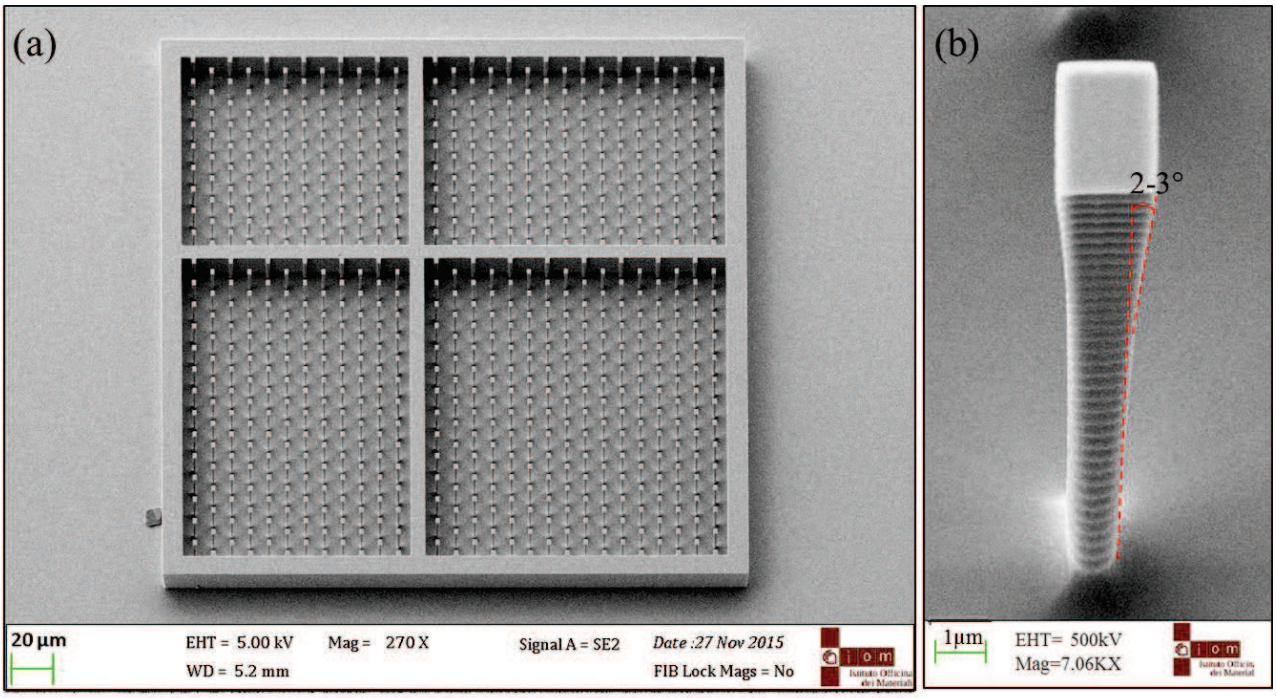

Figure 2.6 – *SEM image of a slightly tilted pillar array, in which the frame surrounding the whole matrix and the hexagonal pillar distribution are visible. (b) A SEM image of a magnified tapped pillar in which the typical scalloped walls and undercut shape (approximately 2-3°) on the upper part are visible.*

Figure 2.6b shows a magnification of tapped pillar structure in which the scalloped walls typical of the BOSCH –like process are visible. Finally, as anticipated in §2.1.1.1, the fabrication protocols have been optimized to obtain structures with a controlled undercut (approximately 2-3°) only on the upper part, as highlighted by the red dotted lines in fig 2b. This concave structure terminating with a vertical post ensures that the pillar size at the base does not depend on the pillar height; thus it was possible to vary one parameter (the height) at a time, allowing a better tuning of the resonance frequencies just acting on the pillars height. As a result the response of the pillars was more uniform between different fabrication batches. The height of the used structure was between 13 and 14µm, and the base width was about 800nm

2.1.2 Superhydrophobic state

The wetting behavior of liquids on a surface is described by the value of the static contact angle Θ, formed between the liquid and the solid phase. For an ideally flat, homogeneous and rigid surface, Θ is expressed by the Young equation 2.1, where γ_{SV}, γ_{SL} and γ_{LV} are the interfacial free energies per unit area of the solid-vapour, solid-liquid, and liquid-vapour interfaces, respectively.

$$\cos\theta = \frac{\gamma_{SV} - \gamma_{SL}}{\gamma_{LV}} \qquad 2.1$$

Thus, on a flat surface a Θ<65° define a hydrophilic state, while Θ>65° corresponds to a hydrophobic behavior and Θ>100° to a "superhydrophobic" one [9], as represented in figure 2.7.

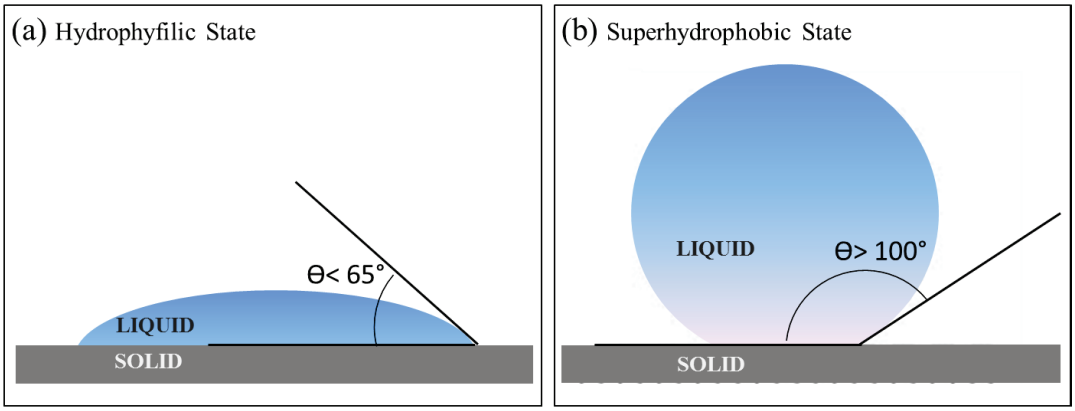

Figure 2.7 – *Representation of the static contact angle Θ in the case of Hydrophilic state (a) and Superhydrophobic state (b).*

The behavior of the liquid on a surface, can be strongly influenced not only by the chemistry at the interface but also by the surface roughness. Indeed, when a polar liquid like water is in contact with a rough hydrophobic substrate, the superhydrophobic state is more prominent with a Θ even higher than 150° [10, 11].

Considering the interaction of the liquid with the structures - pillars in our case - that define the roughness of the surface, two different superhydrophobic configuration can be obtained: the Wenzel state and the Cassie-Baxter state. A shown in figure 2.8a, in the Wenzel state, water intercalates between the structures without spreading all over the solid pattern. The corresponding so-called "Wenzel apparent contact angle", θ_w^*, is expressed by the equation E 2.2 which relates θ_w* to the contact angle θ on a ideally flat substrate with the same chemical composition through *r*, the Wenzel roughness factor.

$$\cos\theta_w^* = r \cdot \cos\theta \qquad 2.2$$

The Wenzel roughness factor is defined as the ratio between the actual area of the rough surface and the geometric projected area, which is always larger than 1. Thus, the equation indicates that in the wetted regime, the surface roughness enhances the hydrophilicity of hydrophilic surfaces and the hydrophobicity of hydrophobic surfaces.

While, in the Cassie-Baxter (CB) state, also named "*composite regime"*, the liquid is in contact only with the top of the asperities, while a cushion of air prevents the lateral side wetting through the formation of a meniscus between air and liquid phases, figure 2.8b. The "Cassie apparent contact angle" θ_c^* is expressed by the equation E 2.3

$$\cos\theta_c^* = -1 + \varphi_s(1 + \cos\theta) \qquad 2.3$$

θ_c^* is related to the static contact angle on the flat surface with the same composition, by the solid area fraction φ_s, defined as the ratio of the effective solid area in contact with the liquid and the apparent solid area (in this case, φ_s is always less than 1):

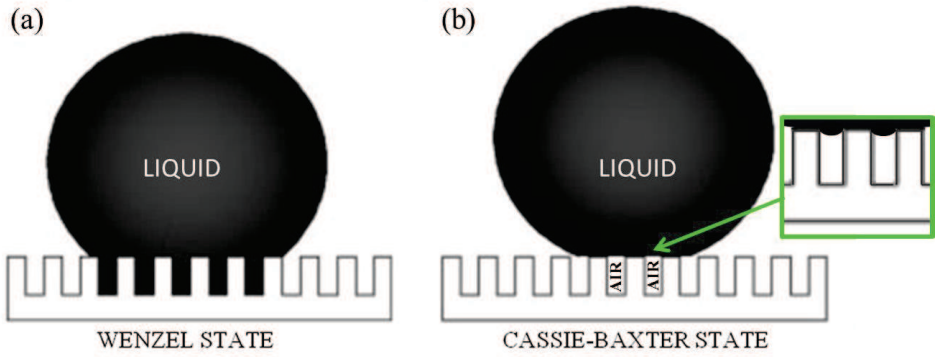

Figure 2.8 - *Wenzel (a) and Cassie-Baxter (b) superhydrophobic configurations: in the first case, liquid intercalates between structures under the droplet, while in the second, liquid is partially suspended by an air cushion formed between structures; the meniscus in visible in the box. Adapted from[11].*

The achievement of a stable CB superhydrophobic state is crucial to use micropillars arrays as mass sensors. Indeed, this state limits the contact of the solution only with the top area of the vertical resonators, providing a localized adsorption of receptors for target molecular recognition. If liquid would wet also the side walls of micropillar, a non-specific mass deposition could occur, altering the mass quantification and nullifying one of the main advantages of micropillars respect to the horizontal cantilever mass resonators.

Superhydrophobic CB states has been obtained on microstructured substrates of intrinsically hydrophilic material, by fabricating structures with asperity slope lower than the contact angle on flat. In this case, the transition between Cassie-Baxter and Wenzel state is a balance of the energy gain due to the wetting of hydrophilic walls and the energy increase due to the growth of the highly energetic liquid-air interface. Typical examples are hydrophilic surfaces with concave pores or lattices of overturned truncated cones[12]. This behavior has also been confirmed for array of tapered micropillars, fabricated with different geometrical configurations, from hexagonal to squared lattices, by Kashaninejad et al.[13]

In the case of our micropillars, the scalloped sidewalls produced by the cyclic dry etching process (figure 2.6b) introduce a further roughness that reduces the contact angle and doesn't ensure a stable CB configuration. Indeed, when we investigated the geometrical configuration proposed by Kashaninejad [13], the water droplet resulted in the complete wetting of the arrays. In some cases, droplet deposition has been effectively possible, but the metastable condition resulted in a sudden collapse of the droplet, with the failure of the Cassie Baxter state.

2.1.2.1 Pillars hydrophobization

In order to achieve permanent Cassie-Baxter state superhydrophobic properties , a surface chemical treatment was introduced, coating the pillars walls with a hydrophobic layer based on

Octadecyltrichlorosilane (OTS, pristine form Sigma Aldrich). The procedure presented here is the result of the evaluation of different possible processes reported in [2].

Immediately before the surface treatment, hydroxyl groups are formed on the surface by treating silicon chip with oxygen plasma (45 sccm, power 45 W, 3 min). After that, the hydrophobic coating is obtained by the reaction of the hydroxyl groups with the Chlorine groups of the Octadecyltrichlorosilane, figure 2.7.

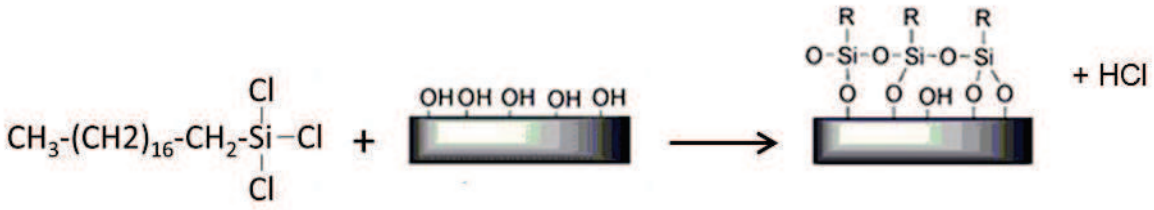

Figure 2.9 – *Reaction scheme of Octadecyltrichlorosilane (OTS) with hydroxyl group on silicon oxide surface. The reported case shows complete monolayer formation. Adapted from [14].*

This reaction is strongly influenced by the presence of water: in fact it has been demonstrated that the absence of water leads only to a partial coverage of Silane [15, 16], while an excess causes polymerization due to reaction of multifunctional silanes and multilayer deposition[14, 17]. A certain amount of water is physisorbed on the surface after hydroxyl groups formation, and experience showed that this is sufficient to ensure the formation of a full coverage. Thus, in order to avoid further absorption of water and to maintain controllable conditions, the reaction was performed overnight by OTS evaporation in a vacuum jar, enabling also the neutralization of the developed hydrochloric acid, through a NaOH absorber.

At the end of the silanization treatment, samples are rinsed in acetone and isopropyl and then dried under a gentle nitrogen flux. Finally, in order to remove the exceeding OTS molecules that are not chemisorbed to the pillar surface, chips are traded in furnace at 150°C per 8 hours[16].

2.1.3 Top of pillars treatment

In order to use micropillars as biomolecular sensors, a proper bio-recognition interface has to be developed. To obtain this, functionalization procedures based on the well-known interaction of thiolated molecules with gold have to be exploited. Thus, immediately before this functionalization step a layer of gold is deposited on top of pillars by e-beam or thermal evaporation. To improve the adhesion of gold with the top of pillars, a Chromium layer (5 nm) is deposited, followed by 20 nm of gold, obtained using a low deposition rate (0.5 Å/s) to ensure a major uniformity. Thanks to the pillar tapered shape, the metal deposition is limited to the top of the pillars and the ground of the array, without affecting the lateral walls. This, in combination with the superhydrophobic Cassie Baxter state, ensures that the further adsorption of molecules takes place only on top of pillars, with advantages in terms of kinetic of absorption, as explained in §1.5, and avoiding the non-specific adsorption on the lateral walls.

Based on the studies made by D. Borin *et al.* [2], the hydrophobic surface treatment leads to a deposition of OTS also on the top of pillar. Nonetheless, depositing gold after the hydrophobic treatment does not affect

the adhesion of the gold layer and doesn't introduce an additional surface roughness that could influences the formation of a dense bio-recognition layer. Conversely, in this way a high cleanliness and consequently a full reactivity of gold can be exploited during the further functionalization step.
After the gold deposition, the reactive layer covalently bond to the top pillars surface is obtained as simple monolayer, is the case of antibodies, or as self-assembled monolayer (SAM) in the case of alkanethiols; details about the used procedure are given in the following chapters.

2.2 Pillar characterization

In this paragraph the procedure and the results concerning the characterization of micropillar are reported. The device characterization involves: the evaluation of the hydrophobic treatment quality, the measurement of the resonance frequency the Q factor and the sensor sensitivity (Hz/fg).

2.2.1 Hydrophobic treatment evaluation

The quality of the hydrophobic treatment is evaluated through Static contact angle measurements. They are performed by depositing one droplet of liquid on the substrate after the hydrophobic treatment and analysing the shape of the self standing drop. The routine control is executed on the flat surface surrounding the chip; in this case a volume of 0.5 µL is enough to cause the detachment of the drop from dispenser syringe. When this measurement is performed on the superhydrophobic pillar array, due to the very low interaction with the solid area, the drop tends to remain attached to the syringe. Thus, to obtain a self standing drop the volume has to be increased around 5-7µL and consequently also the patterned area has to be extended respect to the 300x300 μm^2 used for adsorption studies. Therefore, in order to measure the contact angle over our structured surface, a dedicated micropillars arrays of at least 1.5x1.5 mm^2 have been patterned. Moreover, since in these measurement the side wetting is not an issue, these larger arrays are fabricated without the lateral frame, giving the possibility to visually evaluate the behavior of the liquid between the pillars.

2.2.1.1 Contact angle measurement

Contact angle measurements are performed through a drop shape analysis system (FM 4200, Krüss GmbH, Germany, see Figure 2.8) that consists of a CCD camera, a cold light source, a micropositioning sample holder, and a microsyringe mounted on a dispensing system. The vertical position of the syringe and the volume of the drop are controlled with a dedicated software.

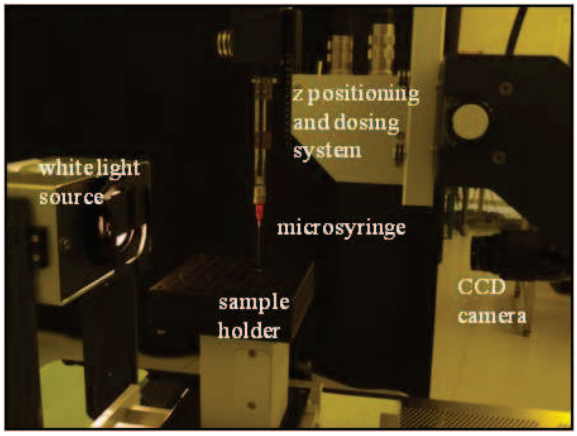

Figure 2.10 – *Drop shape analysis system used to evaluate the contact angle on flat and patterned pillars surfaces.*

A droplet of few µL is put in contact with the substrate and the shape of the self standing drop is registered by the CCD. The solid-liquid contact line can be refined manually and, through the software algorithms, the drop contour at the liquid-air interface is fitted with a proper method and the contact angle between liquid and solid is calculated.

2.2.1.2 Results of contact angle measurements

The static contact angle of a millQ water drop on a flat (figure 2.11a) and on a wide matrix chip (figure 2.11b), both treated with OTS, results >105° and >150° respectively, in aggrement with what already reported in literature [9] These value are assumed as reference for the routine check performed after the silanization treatment.

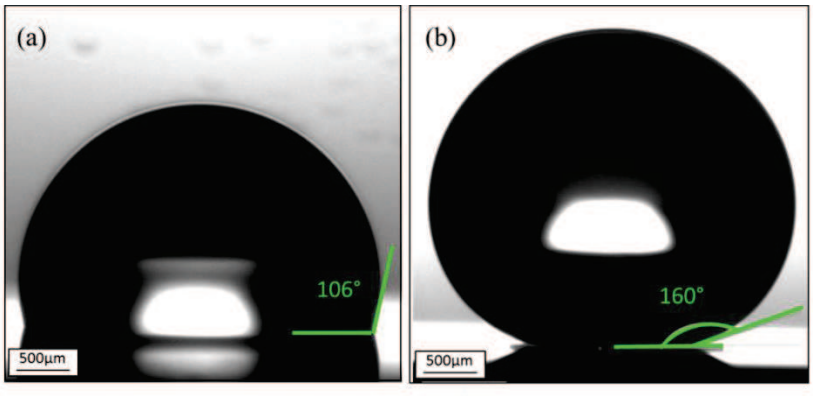

Figure 2.11 – *Static contact angle measure on flat surface (a) and superhydrophobic pillars(b) after salinization treatment.*

In order to test the possibility to use the superhydrophobic pillars array biomolecular sensor with bare human biological samples, OTS treated surfaces have been tested also with human plasma, at different dilutions (from pure form to 1:1000) in milliQ water or in Phosphate Buffered Saline (PBS). Plasma is a dense system of proteins and amphiphilic molecules, therefore it behaves differently compared to milliQ water. Indeed, it

has been observed that with a mild plasma dilution (at least 1:20) the Cassie-Baxter state on the micropillars array is maintained, independently of the used solvent. So, micropillars can be effectively used also with human plasma: the price to pay is represented by a further dilution of the target species that often are already low in concentration [2].

Morover, the influence of the gold layer on the surface has been investigated both with milliQ water and plasma. On the flat surface, the contact angle on OTS treated surfaces results to be higher respect to the gold coated one, while on pillars the superhydrophobic behavior appears to be not influenced by the presence of gold. This is in accord with [18, 19] that hightlight the major importance of the asperities at the three-phase interface, rather than the type of the surface in contact with the liquid. So, in our case, being the gold deposition limited just to the top area of pillars, the Cassie-Baxter state is anyway maintained.

2.2.2 Resonance frequency measurements

The pillars resonance response, on which their use as sensors is based, can be strongly influenced not only by the fabrication process, but also by the hydrophobic treatment, as demonstrated by D. Borin *et al.* [2]. For this reason the pillars response is evaluated after all the fabrication processes are completed. Resonance frequency measurements for calibration purposes are performed with the same setup used for biosensing experiments.

Pillars resonators are actuated using a piezoelectric crystal, driven by a sinusoidal electrical signal and mechanically coupled to the resonator. Measurements of micropillars resonance frequency is performed through the optical lever method[2, 20], commonly applied in cantilever technology. The principle of the method is schematically represented in Figure 2.12. Briefly, it exploits the reflection of a laser beam from the cantilever surface to a segmented photodiode (with 2 or 4 quadrants). At the beginning of the measurement, the reflected laser spot is aligned in order to be at the center of the photodiode and when the cantilever oscillation occurs, the spot position changes; by comparing the electrical signal from the two or four segments, the location of the centroid of the laser spot can be determined ad associated to the cantilever oscillation amplitude.

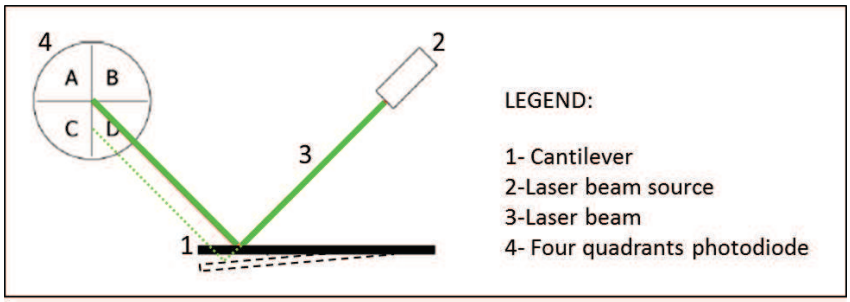

Figure 2.12 – *Schematically representation of the optical lever method based the reflection of a laser beam from the cantilever surface to a segmented photodiode. Depending on the light energy striking the sensitive area of each photodiode segment, an electrical signal is produced and recorded.*

The pillars response is monitored as function of the actuation frequency; the resulting spectra are then analyzed, in order to evaluate the resonance frequency and Q factor. These values are then used for a calibration step, that enables the calculation of the sensor sensibility.

2.2.2.1 Measurement setup

Measurements of micropillars resonance frequency have been performed in vacuum, using the vacuum setup shown in figure 2.12, manly composed by a chamber with an optical window and feed-through connections for the actuation of the pillars motion. Pre-vacuum is provided by a multi-roots dry pump (ALCATEL Adixen ACP 28, US), mechanically uncoupled from the chamber by an heavy attenuator, while the high vacuum level (around $1e^{-6}$ mbar) required for the measurements is obtained by a turbo pump (VARIANT TV70D, Italy) installed laterally to the vacuum chamber and fixed on a damped structure, over which a full scale gauge is mounted and used to monitor the pressure inside the chamber.
Due to the chamber leakage, once the chamber is not anymore evacuated, the pressure rises rapidly. Despite it has been demonstrated that below the 10^{-3} mbar level the effect of pressure on resonance frequency shift and on Q-factor is negligible [21], in order to ensure comparable results the chamber is continuously evacuated during the measurements. Thus, the vacuum setup configuration has been designed to reduce the transmission of vibrations and the effects of mechanical perturbations during measurement.

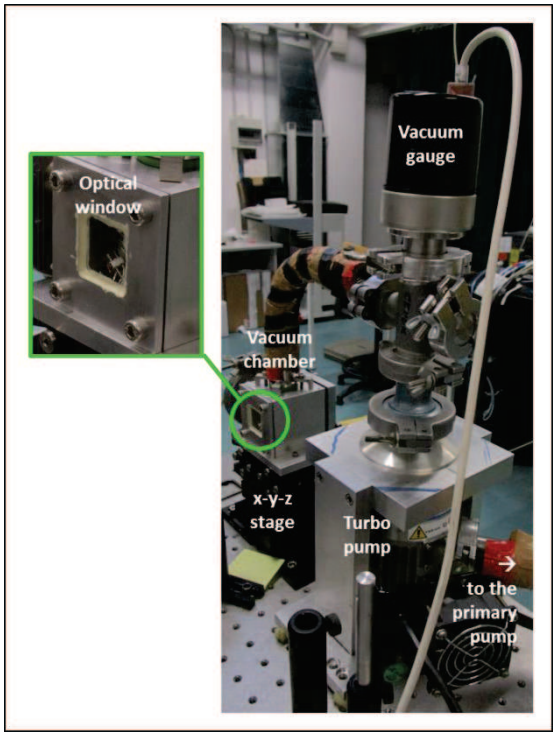

Figure 2.12 – *Image of the vacuum setup, with the turbo pump and the vacuum gauge mechanically uncoupled respect to the vacuum chamber.*

Pillars motion is provided by a piezoelectric crystal (lead zirconate titanate, PZT-5A type, EBL Products, U.S., longitudinal motion) actuated with a sinusoidal signal in a voltage range of 0.5-2 VPP and frequency range of 1.5-2.5MHz.

In the vacuum setup, the sample holder is provided with four different piezo actuators with a capacitance of 0.7-1.5 nF, insulated from each other and from the metallic support by a thin glass layer; on each piezo a small silicon chip with one micropillar array is fixed by double tape. The sample holder is integrated with the vacuum chamber, which is mounted on a xyz micropositioning system to allow alignment with the optical setup during pillars measurement.

In Figure 2.13 illustrates the optical setup scheme though which the optical lever method is implemented for the detection of pillars resonance frequency.

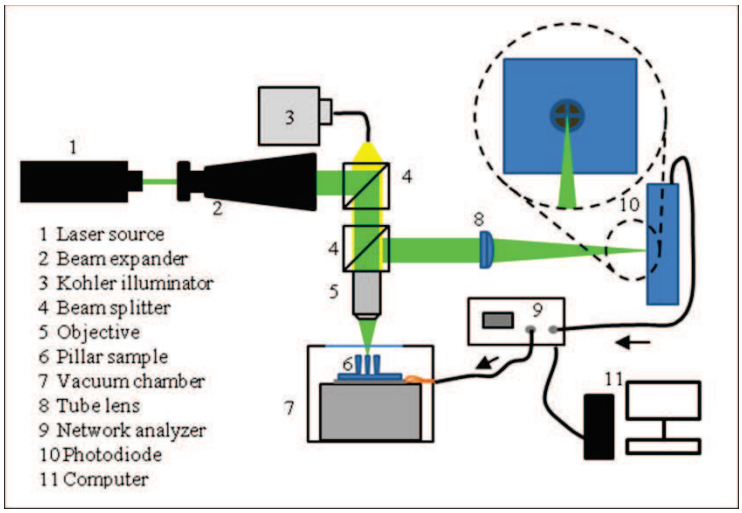

Figure 2.23 – *Schematic representation of the optical setup scheme used for the detection based on the optical lever method.*

A DSPP green laser source (wavelength 532 nm, max power = 100 mW) and a white light source are focused by a long working distance objective (OLYMPUS LMPLFLN 20x or 50x magnification, numerical aperture of 0.40 and 0.50, respectively) thought the optical windows of the chamber, on the top of the pillar to be investigated. The power of the laser is set at 1-2 mW but considering the intensity losses along the optical path, the power on top of pillars is estimate to be less than 100 μW. The reflected beam passes through a tube lens (focal length of 200 mm) that is necessary to focalize, on the photodiode, the infinitive corrected image exiting from the objective. In order to allow the alignment of the spot on the top of a pillar, a mirror can be inserted just before the photodiode to deviate the laser and the white light to a CCD, equipped with a long pass filter (610 nm cut off length) to avoid the saturation of the sensor by the laser. Two 50:50 beam splitters are mounted to convey the laser beam and the white light on the sample and to direct the reflected image toward the photodiode or the CCD.

The detector used to measure pillars oscillation amplitude is a fast four quadrant photodiode (HAMAMATSU S7379-01, with a cut-off frequency around 80 MHz), that is integrated on a home-made electronic circuitry. The signals of the four quadrants are mixed and integrated to give as outputs the

positions of the laser spot on the x and y directions, which are directly proportional to the displacements of the measured pillar. The photodetector circuitry is mounted on a three axis micropositioning system, that is used to align the laser spot at the center of the photodiode. The effective alignment on the x and y direction is monitored through an oscilloscope.

The piezoelectric crystal used to actuate the pillar motion is controlled by a network analyzer (HP 3577A), and the actuation is made by a pure (single frequency) sinusoidal signal, (maximum actuation voltage 3 V_{pp} peak-to-peak): by performing frequency sweeps of progressively reduced span (from 500 kHz to 10 kHz), the resonance spectra of a single pillar is optimized and collected. In network analyzer, the sinusoid is spliced into two signals, one of which goes to the piezo actuator, while the other is used as reference for collection of the resonance spectra. The network analyzer allows collection of 401 points per scan, so the frequency step is automatically determined by the scan width. The x or y signal relative to the pillar oscillation at each frequency is collected by the network analyzer for data storage and processing, as will be illustrated in the next paragraph.

2.2.2.2 Data processing

The resonance spectra are processed by an IgorPro procedure especially developed to obtain automatically the value of the resonance frequency, f_r, and the quality factor, Q. By this procedure, each resonance spectrum is analyzed to identify the resonance peak position; the oscillation amplitude is normalized to compare spectra with different ranges of minimum and maximum and finally the square of the normalized resonance peak is fitted with a Lorentzian curve [20], as shown in Figure 2.14.

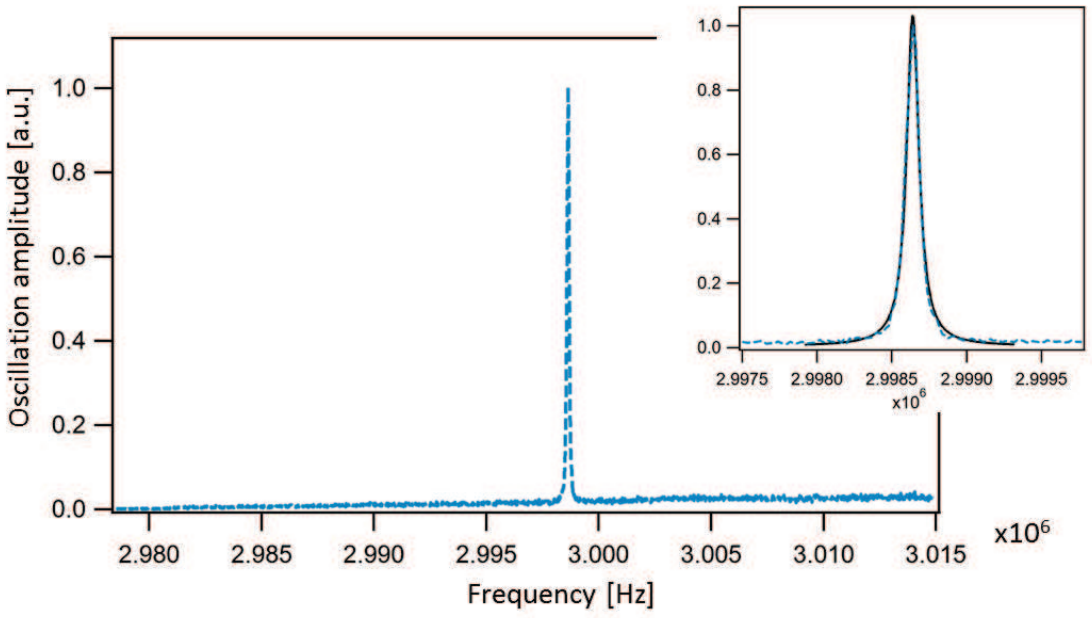

Figure 2.34 – *Example of resonance spectrum: in the main graph, the blue dotted trace represents the oscillation amplitude recorded during a frequency scan in the range between 2.980MHz and 3.015MHz, while the zoom shows the same peak fitted with a Lorentzian curve (dark trace).*

The use of a Lorentzian fit is explained considering equation 2.4, derived from the discussion at §1.3.1, with $\omega = 2\pi f$ corresponding to the angular frequency,

$$x(\omega) = \frac{F}{m}\frac{1}{\sqrt{\left(\omega_0^2-\omega^2\right)^2+(\gamma\omega)^2}} \qquad 2.1$$

Taking its square, it results:

$$x^2(\omega) = \left(\frac{F}{m}\right)^2\frac{1}{\left(\omega_0^2-\omega^2\right)^2+\left(\frac{\omega_0}{Q}\omega\right)^2} = \left(\frac{F}{m}\right)^2\frac{1}{\left((\omega_0-\omega)\cdot(\omega_0+\omega)\right)^2+\left(\frac{\omega_0}{Q}\omega\right)^2} \qquad 2.2$$

If we are close to the resonance frequency and Q is high enough, we can consider that $(\omega_0 + \omega) \cong 2\omega_0$ and that $\omega_0 / Q \cdot \omega \cong \omega_0^2/Q$, so that Eqn. 2.5 can be rewritten as

$$x^2(\omega) = \left(\frac{F}{m}\right)^2\frac{1}{4\omega_0^2(\omega_0-\omega)^2+\omega_0^2\left(\frac{\omega_0}{Q}\right)^2} = \frac{1}{\omega_0^2}\left(\frac{F}{m}\right)^2\frac{1}{4(\omega_0-\omega)^2+\left(\frac{\omega_0}{Q}\right)^2} \qquad 2.3$$

Comparing the last form with the Lorentzian function

$$y = y_0 + \frac{A}{(x_0-x)^2+B} \qquad 2.4$$

from the fitting, x_0 corresponds to the resonance frequency f_r, while Q factor can be calculated from B as

$$Q = \frac{x_0}{\sqrt{2\cdot B}} \qquad 2.5$$

2.2.2.3 Results: resonance frequency and pillar calibration

Despite the parallel fabrication process, resonance frequency of pillars, of different chip, can vary in a wide range, from 1.5 to 3Mhz, with a stable Q_{factor} that is around 12000. The main cause of variety in resonance frequency are the several inevitable sources of inhomogeneities in the lithographic process; on this topic Roukes' group and Murray's group have already reported respectively in [22] and [23]. In our production, the effects of these inhomogeneities have been also evaluated considering the variation of the resonance frequencies of 8 arrays fabricated with the same condition but belonging to different production batches. The mean frequencies of the arrays were spread between 1.9 and 2 MHz. Figure 2.15 shows the histogram of the values of the resonance frequency of all sensors. The mean value is 1.922MHz and the root square deviation is 9% , which is in line with the data reported in literature.

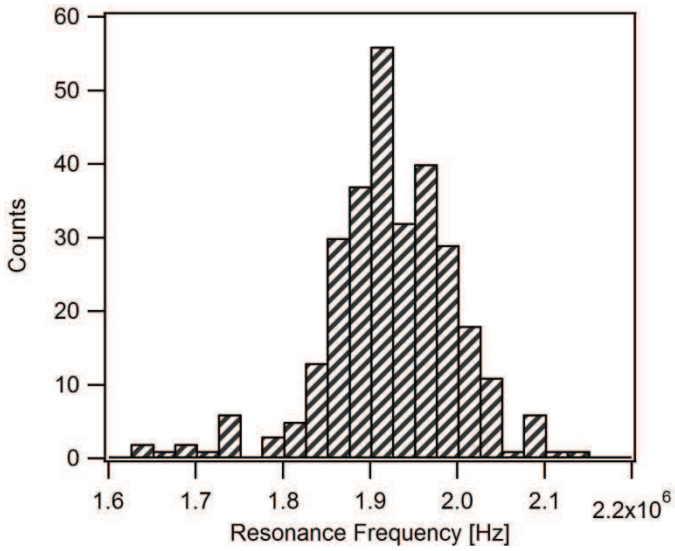

Figure 2.15 – *Histogram of the values of the resonance frequency of sensors from 8 arrays. The mean value is 1.922MHz and the root square deviation is 9%*

Due to the fact that the resonance frequencies of pillars are slightly different but distinguishable, in order to calculate the resonance shift due to mass deposition, each pillar has been measured before and after the mass absorption. Moreover, the obtained resonance shift can be converted to mass through a calibration value that is calculated per each pillar.

The calibration is obtained measuring the resonance frequency before and after the deposition of a known mass, small compared to the resonator one; for example, the same thin layer of gold which is used as base for the formation of the bio-recognition layer. As shown in Figure 2.16, the resonance shift due to the deposited mass is calculated as difference between the resonance frequency at the two steps, for example after and before gold deposition. As already anticipate in Chapter 1, a mass deposited on pillars lead to the reduction of resonance frequency that, in the case of the spectra reported in Figure 2.16, corresponds to -75kHz.

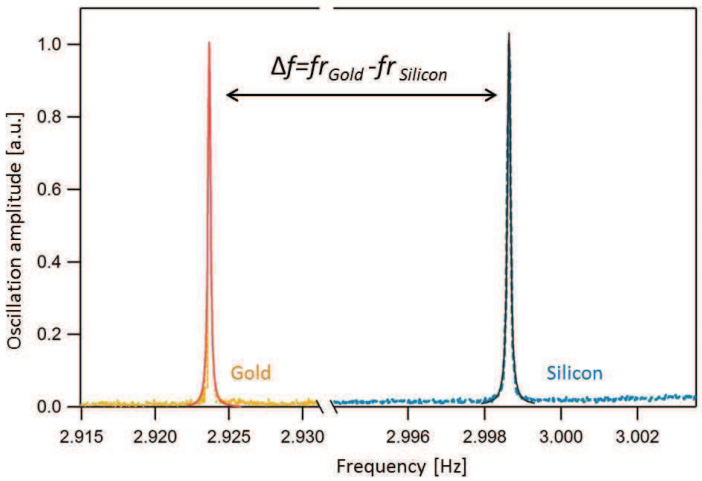

Figure 2.16 – *Frequency resonance peaks recorded for a pillar before (blue trace) and after (orange trace) the deposition of a thin layer of gold (20nm). The resonance shift induced by the gold deposition is about -75kHz.*

After that, the mass sensitivity of the resonator, named *S*, defined as the ratio between the resonance frequency absolute shift and the mass increase, can be calculated by Eqn. 2.9 [1]

$$S = \frac{\Delta f}{\Delta m} \qquad 2.6$$

This number, together with the fact that the measurement and the data processing procedures allow to determine the resonance frequency with an indetermination of about 70 Hz, provides an ultimate mass sensitivity which ranges from 24Hz/fg to 33 Hz/fg.

In addition to sensors quality definition, S is used to calculate the mass deposited in the further biosensing experiment. The frequency shift due to the bio-recognition is converted in a deposited mass by Eqn. 2.10

$$\Delta m = \frac{\Delta f}{S} \qquad 2.10$$

and then in molecular density (molecules/cm^2), assuming the mass of the deposited species (fg) and the pillar surface(cm^2). In the case of a large number of pillars, instead of calculate the sensitivity of each pillar, an average value of S, coming from a subset of measured pillars, can be assumed without introducing relevant errors in the mass calculations.

References:

[1] M. Melli, A. Pozzato, M. Lazzarino, Inverted tapered pillars for mass sensing, Microelectronic engineering, 87(2010) 730-3.

[2] D. Borin *et al.*, How to engineer superhydrophobic micromechanical sensors preserving mass resolution, Sensors and Actuators B: Chemical, 199(2014) 62-9.

[3] S. Fransilla, Introduction to microfabrication, John Wiley & Sons Ltd, (2004).

[4] A.A. Tseng, C.D. Chen, K. Chen, and K.J. Ma, Electron Beam Lithography in Nanoscale Fabrication:Recent Development, Electronics Packaging Manufacturing, IEEE Transactions on, 26(2003).

[5] Robert Bosch GmbH, Method of Anisotropically Etching Silicon, in: U.-P.N. 893 (Ed.)1994.

[6] K.J. Morton, G. Nieberg, S. Bai, S.Y. Chou, Wafer-scale patterning of sub-40 nm diameter and high aspect ratio (>50:1) silicon pillar arrays by nanoimprint and etching, Nanotechnology, 19(2008) 345301.

[7] ISO14644-1:1999, Cleanrooms and associated controlled environments Part 1: Classification of air cleanliness.

[8] N.K. Kim, K.C. Kim, T.G. Kim, and J.G. Park, Chemical and nanomechanical characteristics of fluorocarbon thin films deposited by using Plasma Enhanced Chemical Vapor Deposition, J Korean Phys Soc, 50(2007).

[9] Y. Tian, L. Jiang, Wetting: Intrinsically robust hydrophobicity, Nature materials, 12(2013).

[10] X.S. Cui, W. Li, On the possibility of superhydrophobic behavior for hydrophilic materials, Journal of colloid and interface science, 347(2010) 156-62.

[11] A. Lafuma and D. Quéré, Superhydrophobic states, Nat Mater, 2(2003).

[12] G. Whyman, E. Bormashenko, How to make the Cassie wetting state stable?, Langmuir : the ACS journal of surfaces and colloids, 27(2011) 8171-6.

[13] N. Kashaninejad, W.K. Chan and N.T. Nguyen, Eccentricity effect of micropatterned surface on contact angle, Langmuir : the ACS journal of surfaces and colloids, 28(2012).

[14] P.H. Mutin, G. Guerrero, A. Vioux, Hybrid materials from organophosphorus coupling molecules, Journal of materials chemistry, 15(2005) 3761.

[15] J.D. Le Grange, J.L. Markham. C.R. Kurkjian, Effects of Surface Hydration on the Deposition of Silane Monolayers on Silica, Langmuir : the ACS journal of surfaces and colloids, 9(1993).

[16] D.L. Angst, G.W. Simmons, Moisture Absorption Characteristics of Organosiloxane Self-Assembled Monolayers, Langmuir : the ACS journal of surfaces and colloids, 7(1991).

[17] M.E. McGovern, K.M.R. Kallury, M. Thompson, Role of Solvent on the Silanization of Glass with Octadecyltrichlorosilane, Langmuir : the ACS journal of surfaces and colloids, 10(1994).

[18] C.W. Extrand, Model for Contact Angles and Hysteresis on Rough and Ultraphobic Surfaces, 18(2002).

[19] C.W. Yao *et al.*, C.P. Marsh, Droplet contact angle behavior on a hybrid surface with hydrophobic and hydrophilic properties, Applied physics letters, 101(2012) 111605.

[20] M. Melli, M. Lazzarino and G.Scoles, Fast detection of biomolecules in diffusion-limited regime using micromechanical pillars, ACS nano, 5(2011).

[21] K.Y. Yasumura *et al.*, Quality Factors in Micron- and Submicron-Thick Cantilevers, Journal of Microelectromechanical Systems, 9(2000).

[22] I. Bargatin *et al.*, Large-scale integration of nanoelectromechanical systems for gas sensing applications, Nano letters, 12(2012) 1269-74.

[23] A. Sampathkumar, K.L. Ekinci, T.W. Murray, Multiplexed optical operation of distributed nanoelectromechanical systems arrays, Nano letters, 11(2011) 1014-9.

Chapter 3

Mass signal amplification based on a sandwich assay approach

This chapter deals with the high sensitivity of biosensors, with a specific focus on a sandwich assay approach. Preliminary experiments for mass amplification on pillars using this approach are presented, as introduction and motivation for the investigation on the dependence between the sandwich formation and the dimension of the sensing surface. This analysis provided the conditions for a successful application of the mass amplification on micropillars array, which is demonstrated in the last paragraph.

3.1 Sandwich assay approach for high sensitive biosensor

Sensitivity, together with specificity and high throughput, are the most important parameters on which the research for innovative biosensors is focused since several years. Conventional immunofluorescence assays, widely used in clinical setting, can easily access level of significance within the nanomolar to picomolar range, but higher sensitivity is often requested. This occurs, for instance, when biomarkers are characterized by a low threshold, as for cytokines (e.g. interleukins and interferon), for which a detection limit of at least 50fM is necessary. Moreover, in the case of small analytes (with a molecular weight below 1000 Da) such as endocrine disruptors, the sensor response originated from the binding of this molecules is generally not strong enough to be detected [1, 2]. High sensitivity is as well extremely important in the early stage of diseases; indeed, in this phase the therapeutic efficacy could be very high, but biomarkers are present in blood at very low concentration (fM level or below), and thus they are difficult to be detected with traditional methods. For instance, PSA detection is normally performed in clinical trials in a range of 80-300pM, while ultrasensitive PSA assay at fM level is required for the early detection of tumor recurrence[3].

In 2011, Roukes' group have performed an analysis that shows the performances of different biosensing techniques in terms of limit of detection (LOD) versus the analysis time; the summarizing graph is shown in Figure 3.1. For all the considered techniques, there is a clear trade-off: the reduction of the LOD is generally associated with an increase of the time of analysis.

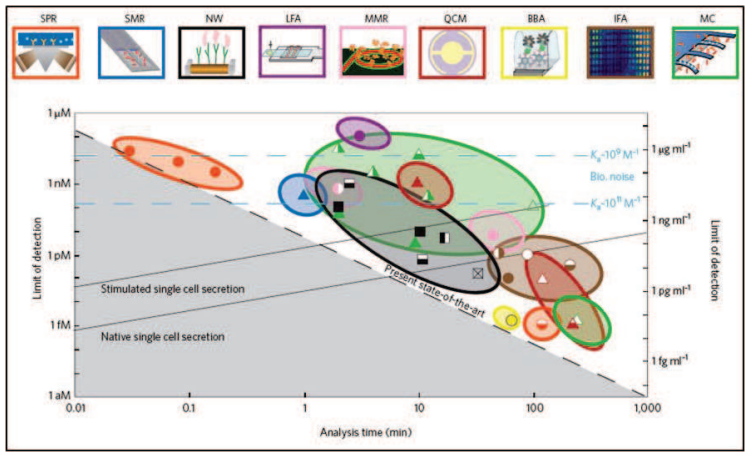

Figure 3.1 – *Comparison of different biosensing techniques in terms of limit of detection versus analysis time. In x axis the analysis time expressed in minutes is reported, while the lower detection limits in y axis is expressed both as molar concentration and as grams per milliliter (considering a reference mass of 34 kDa). Legend of the acronyms: SPR= Surface Plasmon Resonance; SMR = Suspended Microchannel Resonator; NW = Nanowire; LFA = Lateral Flow Assay; MMR = MicroMechanical Ring resonator; QCM = Quartz Crystal Microbalance; BBA = Biobarcode Assay; IFA = ImmunoFluorescence Assay; MC = MicroCantilevers. Image from [4].*

The introduction of nanotechnologies has given the opportunity to explore the potential of nanoscale sensors as ultrasensitive detection systems. Indeed, as demonstrated by P. R. Nair and M. A. Alam [5], the dimensionality of the molecular diffusion field towards the sensor surface plays an important role in determining the limit of detection (LOD) of the sensor. By means of both analytical relationships and numerical simulations, the authors have proved that 2D and 3D molecular diffusion, obtained on SiNWs or nanospheres respectively, allow to reach detection limits up to four order of magnitude higher than what obtained with the 1D diffusion field of planar sensors at the same incubation time. An absorption rate improvement of three orders of magnitude has been also experimentally demonstrated by M.Melli *et al.* comparing traditional cantilevers (1D molecular diffusion) with micropillars on which, due to their geometrical characteristics, a 3D molecular diffusion occurs [6]. However, at very low concentrations - typically femtomolar – the analysis time can still be really long due to the rare binding events on such small sensing surfaces: as reported by P. R. Nair and M. A. Alam, the detection at this concentrations requires an average incubation time that can range from hours to days for SiNW- and CNT-based cylindrical sensors [5].

In order to overcome this issue, the minimum number of analytes required to produce a detectable signal must be decreased. One possibility is to revise the geometrical parameters of the sensor, as suggested by P. R. Naira and M. A. Alam [5]. As alternative, an effective solution can be represented by the enhancement of the signal produced by the single binding trough a sandwich assay approach. The principle is the same used for immunofluorecence assays: a final labelling step is introduced, during which an enhancer element - generally a nanoparticle on which an additional biorecognition molecule (e.g. a second antibody) is tethered - is attached to the target providing the amplification of the signal. In this way, few binding events can be detected and a lower detection limits can be achieved in a short incubation time. In particular for mass sensor, as the pillars, the concept of mass amplification was introduced for the first time at the end of 80s by Richards et al.[7]. In 1994 Ward et al. patented the mass amplification of the response of the analyte on a

quartz crystal microbalance[8]. Later, this strategy has been used both performing the amplification as the last step, as well as increasing the target molecule mass by linking a heavy AuNP particle before exposing it to the surface. In 2009 Waggoner *at al.* combine a new mass sensor geometry (trampoline-like devices) with the mass amplification based on heavy magnetic nanoparticles (NPs weight=1 fg) to detect PSA at fM level; a detection limit of 1,5 fM was demonstrated. In the same year, Kim's group proposed the use of a silica nanoparticles-enhanced DNA assay, to detect the Hepatitis B Virus DNA at fM concentration[9]; the same was done by Lee at al,. for the PSA detection [3]. In 2012 Jeon's group proposed an enhanced detection that used magnetic-photocatalytic nanoparticles. First, they used these particles to separate target biomarkers from human serum; then, after the binding on the surface, exploiting a photocatalytic silver reduction they detected different biomarkers (including interleukin-6, interferon-γ, and alpha-fetoprotein) at fM concentration[10]. Finally, Tamayo and co-workers recently demonstrated the detection of biomarkers from serum at the aM level using gold nanoparticle that act as both mass and plasmonic labels[11].
The sandwich assay approach is generally considered onerous due to the introduction of a second incubation step that leads to a more complex system[4]. On the other hand, beside the reduction of the lower detection limits and the possibility to detect low concentrations at low analysis time, this strategy also offers an increase of the specificity: the non-specific bonds generated during the first step are not effective since they do not react to the following label incubation step, increasing the ratio between the positive signal and the noise.

Moreover, implementing the sandwich assay approach on a micropillars system, using small metal nanoparticles (≤ 20nm) the quantitative character of our mass sensor is preserved and interesting applications regarding the fast detection of the ratio between two biomarkers can be implemented. For a better explanation of this point, the prostate cancer diagnosis can be taken as reference. It has been demonstrated that the ratio between two biomarkers alternative to PSA, prostate membrane specific antigen PSMA and its splice variant PSM' has a significant prognostic value[12].The extracellular C-terminus, present in both antigen forms, is identified by a first antibody, while the intracellular N-terminal domain, which is present only on PSMA, can be recognized by a second antibody[15]. Thus, if the sensor surface is coated with the first antibody, it will provide the total amount of PSMA and PSM'; after that, applying an amplification step based on the use of metal nanoparticles coated with the antibody that recognises only the PSMA form, the PSM' quantity can be calculated as difference between the total (i.e. PSMA+PSM') and the PSMA quantity.

3.2 Mass amplification on pillars: preliminary experiments

In this paragraph the results of mass signal amplification experiments, applied both to DNA and protein detection on micropillars arrays, are briefly reported. Even if their results were not positive, the experiments are discussed as an introduction to the following research activity, described in § 3.3, regarding the possible influence of surface dimensions on the formation of the sandwich. This activity enabled us to identify the

best conditions to successfully apply the sandwich assay amplification strategy on a micropillars, as it will be described in § 3.4.

For both the experiments, micropillars devices were fabricated and made superhydrophobic following the protocols described in Chapter 2, § 2.1.1.1 and § 2.1.2.1 respectively. They were calibrated according to the procedure described in § 2.2.2., resulting in a mass sensitivity around 25 Hz/fg. The measurements of the resonance frequency have been performed in vacuum with the setup and the method described in § 2.2.2.2; data processing was performed as reported in § 2.2.2.3.

3.2.1 Mass amplification of DNA detected signal

The first implementation of the sandwich assay strategy on our micropillars array was done exploiting the biotin-streptavidin system, that is one of the gold standards in sensors development due to its very high affinity (Kd~ 10^{-15}M). The streptavidin was immobilized on pillars surface using DDI strategy (direct DNA immobilization). Figure 3.2 shows a schematic representation of the experiment.

Figure 3.2 – *Schematic representation of a sandwich assay amplified detection of DNA, based on biotin-streptavidin system. First a probe layer is formed with a thiolated ss-DNA; after that, a complementary DNA terminated with a streptavidin is detected. As last step, the system is exposed to biotinylated nanoparticles that bind the streptavidin increasing the signal.*

A micropillars array, previously coated with a thin layer of gold, was functionalized with a single strand DNA; after that, the hybridization of the complementary DNA sequence specifically terminated with streptavidin was performed. The streptavidin is used as binding site for the mass amplification element, represented by a biotinylated gold nanoparticle. The evolution of the experiment was followed detecting the resonance frequency after each step; the deep and dry method was applied: after each step, samples were rinsed in buffer and water, dried with N_2 and measured. The material used and details of the experiment protocol are summarized below.

-ss-DNA self-assembled monolayer formation:

ss-DNA SAM was formed incubating micropillars with a solution of 3' thiol-capped DNA 22-oligonucleotide @5µM in TAE 1X, 1 M NaCl, overnight at room temperature;

-cDNA-STV hybridization:

DNA hybridization was performed exposing the functionalized micropillars array to a solution of the complementary DNA terminated with streptavidin (DNA 22-oligonucleotide modified at 5' with streptavidin

by the group of *Dr. Ljiljana. Fruk-CFN, Karlsruhe Institute of Technology*) in TAE 1X, 1 M NaCl, 2h at room temperature;

-amplification with biotinylated nanoparticles:

the amplification step was performed exposing the hybridized system to a solution of biotinylated gold nanoparticles (CGB5K-20 purchased from Cytodiagnostics) @ 100nM in water, for 2h at room temperature.

Detection and amplification of cDNA at two concentrations were tested, 100nM and 10pM. In both cases, after the exposure of the system to the biotinylated nanoparticles, an increase of the resonance frequency was recorded; this suggests that the nanoparticles provide a reduction of the material presence of pillars instead of the expected amplification of the negative shift coming from the previous hybridization step. To understand what happened, the experiment was reproduced on a flat gold surface using AFM nanografting technique. To assess the experimental conditions used on pillars, considered that the top of pillars is 2x3μm, ss-DNA sequence was grafted creating patches of 1x1 μm. After that, the hybridization with the complementary DNA terminated with a streptavidin (concentration 100nM) and the exposure to the biotinilated nanoparticles were performed. For each step of the experiment AFM imaging was performed. In Figure 3.3, on the left side AFM images are shown, while on the right the heights of the three patches along a cross section are reported. Comparing the height of the patches after the formation of the ss-DNA SAM (AFM image (a), blue line on the graph) with the one obtained after the hybridization (AFM image (b), green line on the graph), an increase of about 5nm is registered, confirming the hybridization success. Instead, after the exposure to the biotinilated nanoparticles, the height is reduced to the level of the ss-DNA SAM or below, suggesting that the nanoparticles induce the de-hybridization (AFM image (c), red line on the graph). Indeed, performing again the hybridization step (AFM image (d), yellow line on the graph), the height goes back to the previous value, and executing again the exposition to the nanoparticles (AFM image (e), purple line on the graph). it comes back to the ss-DNA SAM height.

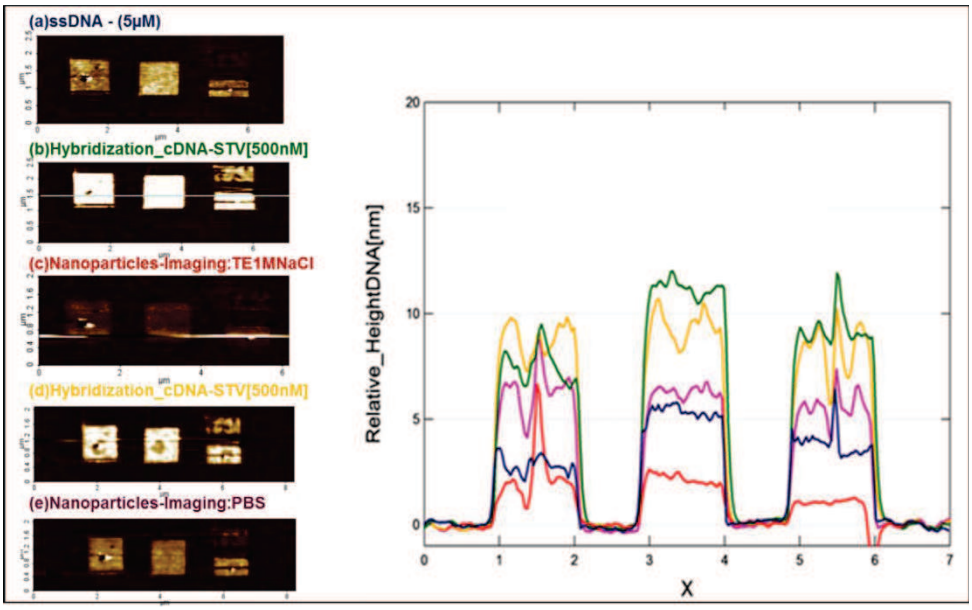

Figure 3.3- *Results of AFM analysis performed on 1x1 μm grafted patches during the sandwich assay steps. On the left, AFM imaging of ss-DNA SAM (a), first c-DNA-STV hybridation (b), first exposition to biotinylated nanoparticles (c), second c-DNA-STV hybridation (d), second exposition to biotinylated nanoparticles (e). On the right side, the graph reports the heights of the three patches along a cross section of the AFM image. AFM analysis performed in collaboration with the group of Dr. Loredana Casalis, NanoInnovationLAB, Elettra Sincrotrone Trieste.*

In this case the negative result has been associated to a competition between the DNA hybridazation, which has a nM affinity, and the biotin-streptavidin bound, whose affinity is at the fM level.

3.2.2 Mass amplification of protein detection signal

A second tentative of sandwich assay application was done amplifying the signal obtained by protein detection, reproducing on micropillars array the same conditions used in ELISA tests. As shown in Figure 3.4, a layer of a thiolated antibody was created on the pillars surface; after the exposure to the antigen, a last labelling step was performed, incubating the system with a second antibody.

Figure 3.4 – *Schematic representation of a sandwich assay amplified detection of protein. First, a layer of thiolated antibody is formed on the surface of gold pillars; after the antigen detection, the system is incubated with a second antibody.*

The materials and protocol are here only briefly described, while an exhaustive discussion about them is provided in Chapter 6, where they are extensively used. The experiment had the aim of amplifying the pillars resonance frequency shift obtained by the detection of PSMA, prostate specific membrane antigen, a transmembrane glycoprotein used as alternative biomarker in the prostate cancer diagnosis. The first antibody was a monoclonal antibody (named D2B), that recognises extracellular C-terminus of the antigen,

while the second one is an anti-Histidine (His)-HRP (conjugated with the peroxidise enzyme HRP), molecular weight 190kDa, normally used in ELISA test .
Being the aim of this preliminary experiment only to confirm the feasibility of the sandwich on pillars, we considered that the use of a secondary antibody, even without conjugated nanoparticles, should be sufficient to result in a mass amplification. The details of the experiment are reported below:

*-first antibody layer: m*icropillars array were incubated with a solution of D2B @ 70nM in Ethanol, for 15 minutes at room temperature;

*-PSMA detection: f*unctionalized pillars were exposed to a solution of PSMA in phosphate saline buffer at a certain concentration, for 1h at room temperature;

- first antibody conjugation: he system was incubated with a solution of the second antibody @ 70nM for 1h at room temperature.

The resonance frequency measurements were performed in vacuum, but differently from the previous experiments with DNA, in order to avoid any alteration of the antibody configuration, all steps are performed without breaking the wet condition; therefore all the reported values refer to different samples.
PSMA has been detected at two concentrations (100nM and 10nM); for each concentration two samples were prepared, and for one of them also the amplification step has been performed.
In Figure 3.5 the resonance frequency shifts are reported as function of the PSMA concentration. The values are an average coming from ten different pillars and the error bars are calculated as standard deviation.

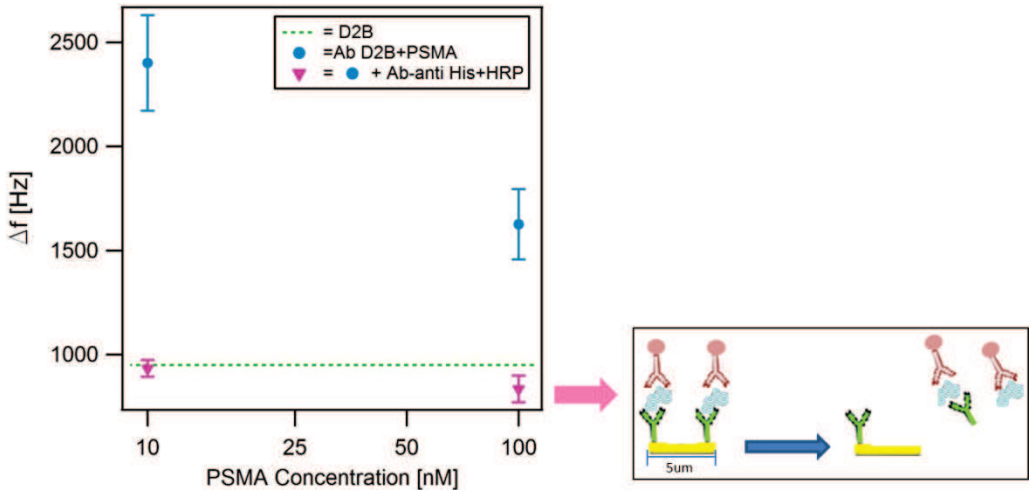

Figure 3.5–*Resonance frequency shifts are calculated after the detection of PSMA (blue dots) and after the amplification step with a second antibody (purple dots) as function of the PSMA concentration. The values are an average coming from ten different pillars and the error bars are calculated as standard deviation*

In the graph, the green line represents the frequency shift correlated to the layer of the first antibody. The blue spots indicate the resonance shift due to the PSMA detection, while the purple spots correspond to the shift recorded after the incubation with the second antibody.
Also in this case the signal recorded after the amplification step is comparable with the one obtained with the first antibody. Contrary to what supposed for the experiment with DNA, no competition in terms of affinity should be present in this case.
Considering this result, the fact that this protocol is normally used in ELISA assay and that the examples of mass amplification via sandwich assay reported in literature are performed on surfaces whose area is from one[2], the only case of small surface, to three order of magnitude[3, 9, 11] larger than that of pillars ($<10\mu m^2$), it has been hypothesized that the small pillar surface with its high reactivity could influence the formation of the sandwich assay. Thus, we decided to investigate if there is any correlation between the creation of the sandwich and the dimensions of the sensing area.

3.3 Investigation on the sensing area dimensions influence on sandwich assay formation

In order to investigate if the formation of the sandwich assay is influenced by the dimension of the area, substrates containing gold patches with an area that varies in a range between 4 to $10000\mu m^2$ were developed and used to test the formation of the sandwich exploiting a biotin-streptavidin system: a self assembled monolayer that exposes biotin was formed, incubated with streptavidin and exposed to biotinylated nanoparticles. The quantity of nanoparticles deposited on the surface was evaluated as function of the patches area, of the incubation time and of their concentration.

3.3.1 Fabrication of substrates containing gold patches of different dimensions

The samples containing gold patches are fabricated combining optical photolithography with a resist transfer to the final glass substrate. The protocol is schematically summarised in figure 3.6a.
A thin layer of gold (40nm) is deposited on a clean oxidized silicon wafer, without any adhesion layer. Above the gold a thin layer of positive photoresist (SPR™220- microresist technology) is deposed by spin coating (3000rpm, 1min). The photoresist is exposed to UV light (wavelength 365nm, power 7mW) for 8 seconds through a silica optical mask containing the positive image of the patches to be patterned. In this way the regions exposed to the UV light become soluble and are eliminated through the development step, performed immersing the silica substrate in a proper developer (MF-24A MicroChem) for 30 seconds, and exposing the gold out of the patches design. At this point a wet etching of gold is performed, immersing for 15 seconds the silica substrate in a solution KI/I_2 with a mixing ratio $KI:I_2:H_2O$ = 4g:1g:40mL: the gold that is not protected by the resist is removed, obtaining a grating of gold patches. After that, gold patches are transferred on a glass surface exploiting their low adhesion to silicon oxide. This part of the protocol is performed immediately before to use them, so that the full reactivity of clean gold can be exploited.

A small quantity of a negative resist (ORMOCOMP-Microresist Technology) is then deposited on the gold patches grating. A rectangular piece of glass with a dimension of 1,5x2cm, previously cleaned in Piranha solution (H2SO4:H2O2=7:3) for 15 minutes and activated by plasma oxygen for 5 minutes at 100mW, is placed on the resist, and a soft backing is performed at 80°C for 2 minutes; in this way ORMOCOMP becomes less viscous and fills the gaps between the gold patches. A curing step is performed exposing the substrate to the UV light (wavelength 365nm, power 7mW) for 3 minutes. After that, in order to improve the adhesion of ORMOCOMP to the glass, a post backing at 80°C is performed for 5 minutes. At the end the glass substrate is stripped, obtaining on its surface a layer of ORMOCOMP in which gold patches are integrated.

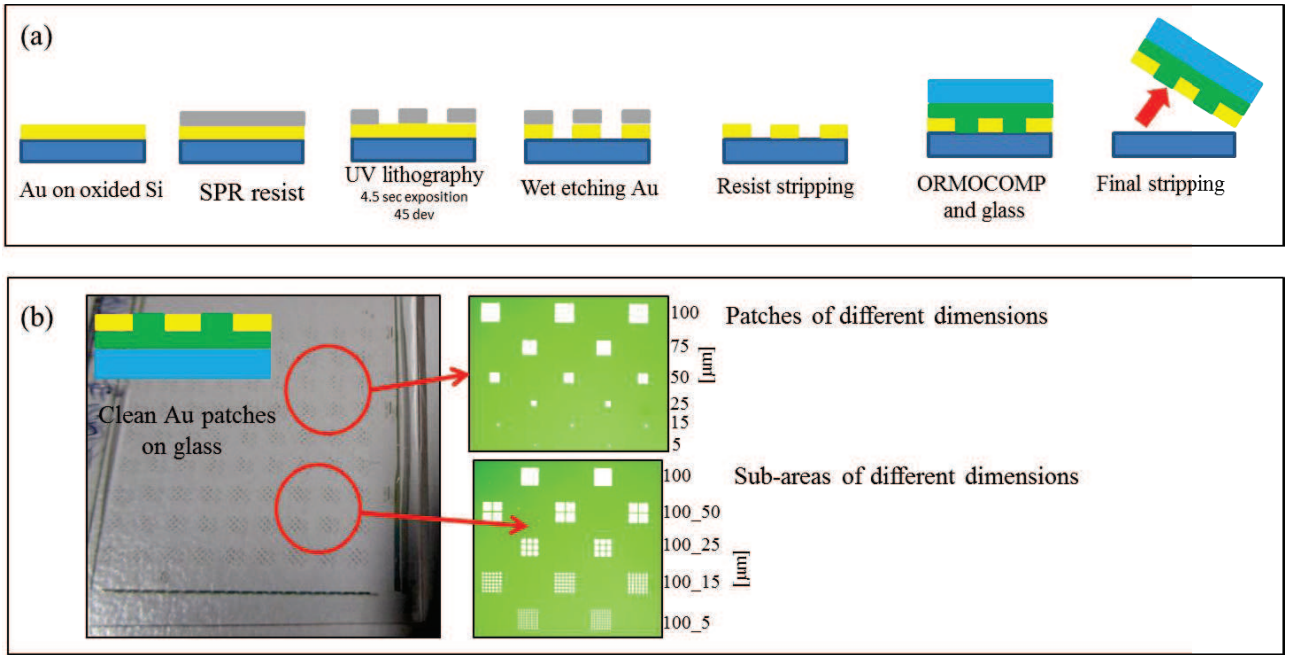

Figure 3.6–*Schematic representation of the gold patches substrate fabrication protocol(a); an example of the resulting substrate (b)*

The results of the fabrication process are shown in figure 3.6b. Three types of gold patches were produced: the first consists of isolated gold patches, with areas in the range from 4 to 10000 μm^2, and minimum distance between two patches of 100 µm. The second and the third series consist of 100x100µm gold patches, which are divided in sub-squares 50x50µm, 25x25µm, 15x15µm and 5x5µm, with two different distances between the sub-areas: 10 and 5 µm. In the following paragraphs, isolated single patches will be indicated with their lateral side dimension (e.g. 100 for a patch 100x100µm), while patches in array will be indicated as *ndm,* where n=dimension of the lateral side of the patches and m=distance between patches in the array.

3.3.2 Biotinylated nanoparticles

Gold nanoparticles are functionalized in our lab, due to the high quantity needed to perform a systematic study.

The 3' thiol-capped DNA oligonucleotides modified at 5'with biotin used for the functionalization were purchased with HPLC purification from Sigma-Aldrich. The gel filtration columns used to desalt DNA solution from DTT were illustraTM NAP5 and NAP10 Columns from GE-Healthcare. 20nm diameter gold nanoparticles stabilized in citrate were purchased from TedPella. The NPs concentration was determined analysing the absorbance of the suspension (diluted in water 20 times) in optical glass cuvette through Perkin-Elmer spectrophotometer assuming an extinction coefficient of 9.41 x 108 M^{-1} cm^{-1}.

Au nanoparticles were functionalized following several steps; the details are reported by L.Piantanida in his Ph.D. thesis. Briefly, first a coating with BSPP (Bis(p-sulfonatophenyl) phenylphosphine dihydrate dipotassium salt) was carried on following published procedures[13-15].

Then the particles were centrifuged to remove supernatant before being rinsed, concentrated and resuspended in 2.5 mM BSPP in approx. 2 mL. Afterwards, since the commercial DNA oligoucleotides are protected with disulfide bond, before use, they were reduced with DTT (0.37 M) in a solution with NaCl (0.3 M) and sodium phosphate buffer (0.01 M NaH2PO4/Na2HPO4, pH 7.04) for at least 2 h of incubation. After filtration with NAP5/10 columns the oligonucleotides were mixed with colloids solution (final concentrations ~0.33 nM AuNP, ~3 μM oligonucleotide). After 24 h sodium phosphate buffer (10 mM) was added and the solution was incubated overnight. In a subsequent salt-ageing process, NaCl solution was added to reach the concentration of 0.1 M in 6 steps during 48 h. To remove free oligonucleotides that didn't react and to exchange the buffer, the solution was centrifuged three time with Amicon® with 100K cut-off filter (purchased by Millipore) for 1.5 min at 14000 x g. The dark red suspension obtained was redispersed in buffer (TAE 1X, 0.1 M NaCl) and stored at 4°C.

Once functionalized, the dispersion stability of NP was checked visually controlling the color, that should remain ruby red during agarose gel electrophoresis. If the NP are stable in buffered media like the running buffer of gel electrophoresis they enter in the gel producing a clear red colored band. On the contrary, if they are not stable enough they form a distorted black band suggesting a large aggregation in presence of ionic charges.

Finally, to demonstrate the presence of biotin on the functionalized gold NPs, we induced aggregation by adding streptavidin to the solution. In particular mixing 40nM STV (in a SPB 0.5 M solution) with AuNPs @ 4nM, we obtained an aggregation that is visible from the absorption spectrum reported in Figure 3.6: after the exposition a shift of 5nm of the to the absorbance peak is detected.

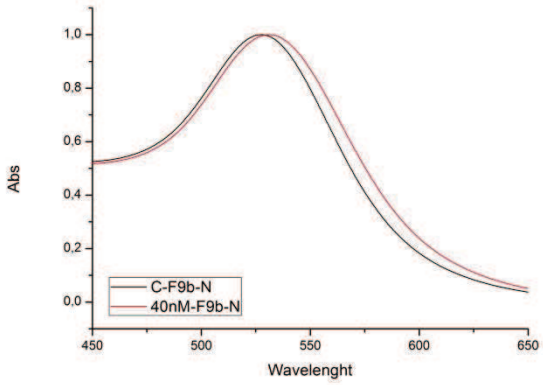

Figure 3.6 – *Absorbance spectrum of biotinilated 20nm gold nanoparticles, before and after the aggregation induced by streptavidin.*

3.3.3 Experimental protocol and results

To investigate the formation of the sandwich on the gold patches, first a mixed self-assembled monolayer of a biotin PEG thiol mixed with a mercapto-thiol was created on gold patches. The dilution of the biotin with oxydril group was performed to reduce the aspecific binding, and the ratio between the two components was defined according with data reported in literature to maximise the following streptavidin binding [16-18].

After the functionalization, an ORMOCOMP passivation step was performed incubating the substrate with a solution of bovine serum albumin (BSA). This step is needed to reduce the aspecific binding of streptavidin to ORMOCOMP that wouldn't allow to discriminate the behaviour of the individual gold patches. Thus, the substrate were incubated with a streptavidin solution and finally with a solution of biotinylated gold nanoparticles. The incubations were performed with a drop in a saturated environment, in order to avoid the concentration change due to evaporation. After each step, samples were rinsed in a proper solvent without getting dry; only after the last step they were gently dried with N_2.
A schematic representation of the experiment steps is shown in Figure 3.7, while details regarding material and protocols are reported below.

Figure 3.7 – *Schematic representation the biotin-streptavidin sandwich assay: mixed SAM exposing biotin and -OH group is incubated with streptavidin, on which biotinylated nanoparticles are then linked.*

-*Mixed (OEG-BPEG) SAM formation*: substrates were incubated overnight at 4°C with a solution of the (11-Mercaptoundecyl)tetra(ethylene glycol) (OEG, 674508 from Sigma-Aldrich) and a biotin-Peg thiol-(BPEG, PG2-BNTH-3k, from NANOCS) in ethanol; the thiol concentration was fixed at 500nM and EOG:BPEG ratio was 9:1. At the end of the incubation, sample were rinsed fist in ethanol and then in mQ water;

-ORMOCOMP passivation step: samples were incubated with a solution of bovine serum albumin (BSA, A9418 from Sigma-Aldrich) at 2%w/v in SPB(10mM) for 1h at room temperature and then rinsed in SPB (10mM);

-Streptavidin incubation: samples were incubated with a solution of streptavidin (S4762 from Sigma-Aldrich) @ 10nM in SPB(10mM), for 2 hours at room temperature and then rinsed in SPB (10mM);

-Exposition to biotinylated nanoparticles: samples were exposed to a biotinylated nanoparticles solution in SPB(10mM) at proper concentration, for a certain time – depending on the performed experiment - at room temperature; they were rinsed first in SPB (10mM), then in mQ water and finally dried.

In order to quantity the number of nanoparticles attached to the differ types of patches, after the deposition of a thin layer of chromium (5nm) that makes the surface conductive, scanning electron microscopy (SEM) images were acquired and analysed with the *"Particle Size Analyzer (PSA)"* macro available in ImageJ software: counting the number of particles present on an analysis area of at least 5x5µm, the density of particles (number of NPs/cm2) on each type of patch was calculated. As reference, Figure 3.8 shows the SEM images of two patches after the incubation with nanoparticles: the one in Figure 3.8(a) is a control sample (not incubated with streptavidin), while on the sample in Figure 3.8(b) all steps have been performed.

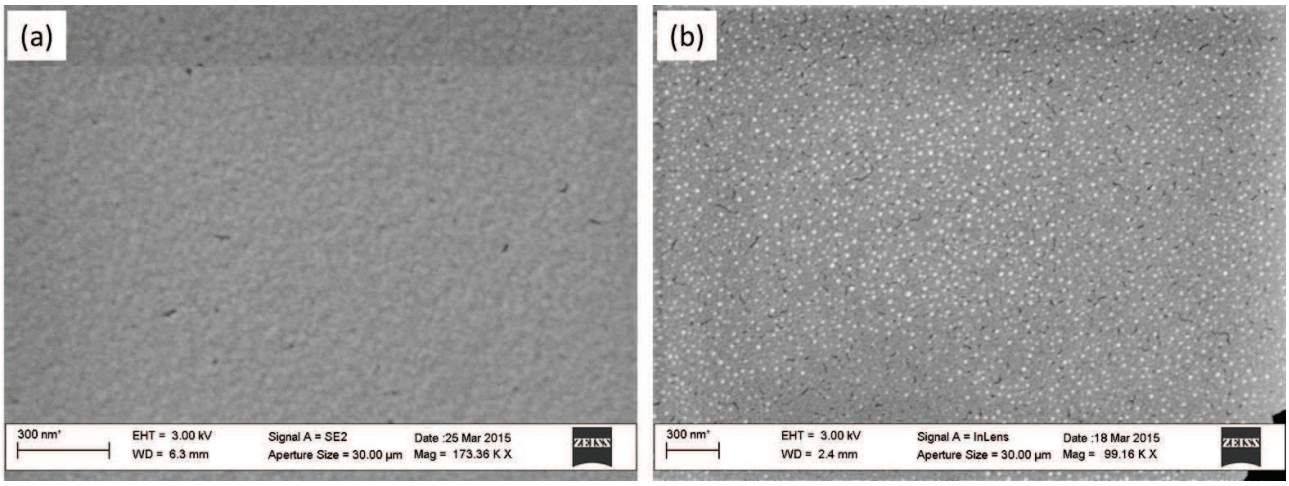

Figure 3.8- *An example of SEM images of two patches surface after the incubation with nanoparticles. (a)control sample (not incubated with streptavidin); (b) a sample on which all steps have been performed.*

At the beginning the nanoparticles incubation time was set to 1 hour according to the data reported in literature, and different concentrations (6pM, 60pM, 0,5nM and 1nM) were tested. Considering all patches types, a density in a range between 1,5 - $4 \cdot 10^9$ NPs/cm^2 was reached at 1nM. This value is comparable with the density expected at the saturation, estimated assuming that nanoparticles have a diameter of 20nm, that the density of streptavidin on the surface, measured by AFM, is around $7 \cdot 10^{10}$ molecules/cm^2 and that the ratio STV:NPs on the surface is 9:1 (the streptavidin has a footprint < 35nm^2). Moreover, 1nM was found experimentally to be the largest concentration at which the aggregation process is still negligible (Figure 3.8b), while higher concentrations lead to the formation of aggregates, complicating the analysis.

In Figure 3.9 the recorded density of nanoparticles is reported as function of the patch type, for incubation of 1 hour with 1nM solution. The labels on the x-axis refer to the lateral dimensions of isolated squared patches (left quadrant), and patches in array (right quadrant). The values are the average of at least four patches of the same type, and the error bars correspond to the standard deviation. Analysing the density recorded for the different types of patches, small patches in dense array (patches distance =5µm) seem to have the largest density, even if the complete set of data varies within a small range (1,5 – 3,5 NPs/cm^2).

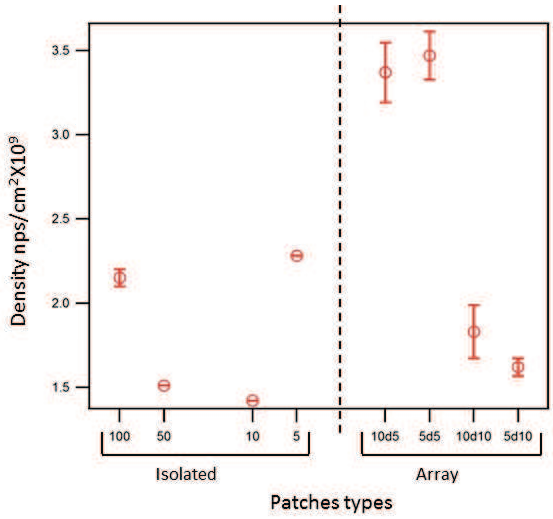

Figure 3.9- *Nanoparticles density recorded on different type of patches incubated with biotinylated nanoparticles at 1nM for 1h. On the x axis, the numbers on the left side are referred to the lateral dimensions of isolated squared patches, while on the right side patches in array are considered.*

Afterwards, keeping the concentration at 1nM, different incubation times (3, 60, 90 and 720 minutes) were tested in order to understand the dynamics of the sandwich formation. Figure 3.10 shows the recorded density values as function of the incubation time. The comparison considered a big patch (100, green line), that simulate an extended surface, and one with a dimension comparable with the top of pillars (5x5µm), isolated (red line) and inside a dense array (patches distance =µ5m, blue line). The value reported are the average among at least four patches of the same type, the error bars correspond to the standard deviation.

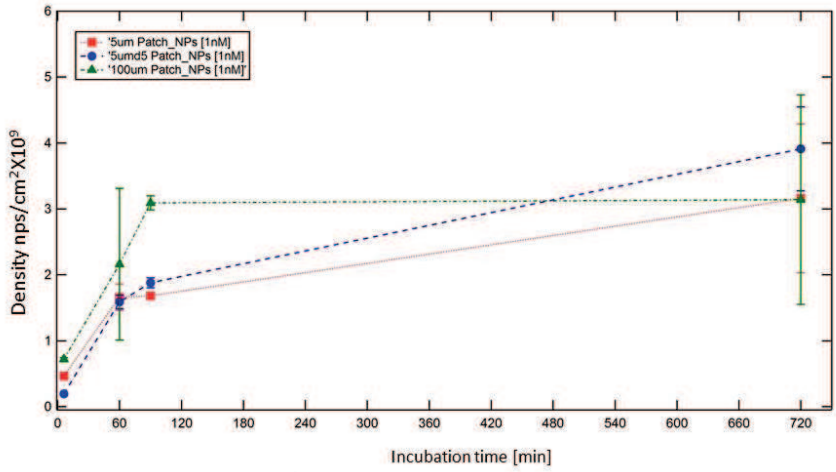

Figure 3.10-*Nanoparticles density on different types of patches (100= green line, 5= red line and 5d5=blue line) recorded as function of the incubation time.*

Observing the graph, it can be concluded that the saturation curves are actually similar for all the considered types of patches: after 90 minutes the saturation is reached both on small and big patches, with a density value of $3 \cdot 10^9$ NPs/cm^2. Those data do not support the hypothesis that the patch area have a role on the sandwich formation.

3.4 Biotin-Streptavidin sandwich assay on pillars surface

After the confirmation of the possibility to achieve the sandwich both on extended ($\geq 10000\mu m^2$) and on small surface ($25\mu m^2$) comparable with the top of pillars, the experiment performed on gold patches has been replicated on pillars. The aim of this investigation was to demonstrate how the mass amplification can improve the limits of detection signal obtained by pillars; this was done using a biotin-streptavidin system, for which in the previous paragraph it was demonstrated that no affinity competition is introduced in the case of small surfaces.

The references for the micropillars array fabrication, their treatment and resonance frequency measurements are the same reported at the beginning of §3.2.

Seven samples of micropillars arrays, previously coated with a thin layer of gold, have been functionalized with a mixed SAM of OEG-BPEG. One of them (named "Only SAM") was kept as reference in order to determinate the mass contribution due to the SAM formation. The other six samples were treated with streptavidin at three different concentrations (1nM, 1pM and 100fM), using the same conditions reported in §3.3.3. For each streptavidin concentration, two samples were prepared; both were incubated with streptavidin, but only one of them was exposed to the biotinylated nanoparticles at 1nM in SPB for 1h.

In Table 3.1 the treatments executed on the seven samples are summarized. The column "Incubation steps" reports the concentrations, at which the different incubations were performed. The other columns contain: the calculated resonance frequency shift (including all contributions coming from the different incubation

steps), the deposited mass, and the molecular or nanoparticles density, assuming the mass of thiols molecules forming the SAM =$6\cdot10^{-7}$fg, of streptavidin= $8{,}7\cdot10^{-5}$fg, biotinylated gold nanoparticle $8{,}2\cdot10^{-2}$fg, and a pillars area of $5{,}5\cdot10^{-8}$cm^2.

The deposited mass after the incubation with streptavidin is calculated subtracting the contribution of the SAM (19fg), while the deposited mass corresponding to the nanoparticles is calculated subtracting both the contributions coming from the SAM and from the streptavidin.

SAMPLE	Incubation steps			Resonance frequency shift [Hz]	Deposited mass [fg]	Density [NPs or Molecules / cm^2]
	SAM	STV	B-NPs			
OnlySAM	500nM	-	-	-526±69	19	$5\cdot10^{14}$
STV100fM	500nM	100fM	-	-873±247	11	$2{,}3\cdot10^{12}$
STV100fM+NPs	500nM	100fM	1nM	-5483±1410	158	$3{,}3\cdot10^{10}$
STV1pM	500nM	1pM	-	-1200±108	21	$4{,}3\cdot10^{12}$
STV1pM+NPs	500nM	1pM	1nM	-6520±950	177	$3{,}8\cdot10^{10}$
STV1nM	500nM	1nM	-	-1200±108	22	$4{,}5\cdot10^{12}$
STV1nM+NPs	500nM	1nM	1nM	-7444±1722	251	$5{,}4\cdot10^{10}$

Table 3.1- *Summary of the treatments executed on seven micropillars array samples, reporting the concentrations at which the incubation steps are performed, the calculated resonance frequency shift, the deposited mass and the molecular/nanoparticles density.*

Considering that the K_d defining the affinity of the biotin-streptavidin system has a value of $\sim 10^{-15}$M, it is normal that the system results to be saturated at a pM concentration, and that the masses of detected streptavidin in the case of 1pM and 1nM concentrations are comparable, while a significant difference is recorded at the fM level. The interesting and positive result is that, after the incubation with the biotinylated nanoparticles, for all the three streptavidin tested concentrations the deposited mass is increased 10 times. Comparing the number of streptavidin molecules deposited on the surface and the number of nanoparticles, the latter are two orders of magnitude less; for instance, exposing the system to streptavidin @1nM (last two samples of Table 3.1), the detected 22fg of streptavidin deposited mass correspond to around $2\cdot10^5$ molecules, while, the 251fg of detected mass after NPs incubation correspond to around $2\cdot10^3$ nanoparticles. The comparison of these two values suggest that one nanoparticle is fixed on the surface approximately every 100 molecules of streptavidin vs the 1:9 ratio of the occupied area of the two molecules.

The unfavourable ratio STV:NP is probably due to the steric hindrance between neighbouring NPs in such a dense system. By reducing the density of STV we expect to approach a regime in which for each STV we bind a biotinylated NP.

In conclusion, considering that the minimum frequency shift detectable by our system is around 70Hz, and that the mass sensitivity is in average 25Hz/fg, the minimum measurable mass without amplification is around 3fg; this value can be decreased to 300ag with the current amplification conditions. Further investigations should be performed, in order to evaluate the amplification factor with an optimized STV:NPs ratio, and thus the minimum concentration that can be detected with this method.

References:

[1] J.W. Park, S. Kurosawa, H. Aizawa, Y. Goda, M. Takai, K. Ishihara, Piezoelectric immunosensor for bisphenol A based on signal enhancing step with 2-methacrolyloxyethyl phosphorylcholine polymeric nanoparticle, The Analyst, 131(2006) 155-62.
[2] P.S. Waggoner, M. Varshney, H.G. Craighead, Detection of prostate specific antigen with nanomechanical resonators, Lab on a chip, 9(2009) 3095-9.
[3] S.M. Lee, K.S. Hwang, H.J. Yoon, D.S. Yoon, S.K. Kim, Y.S. Lee, et al., Sensitivity enhancement of a dynamic mode microcantilever by stress inducer and mass inducer to detect PSA at low picogram levels, Lab on a chip, 9(2009) 2683-90.
[4] J.L. Arlett, E.B. Myers, M.L. Roukes, Comparative advantages of mechanical biosensors, Nature nanotechnology, 6(2011) 203-15.
[5] P.R. Nair, M.A. Alam, Performance limits of nanobiosensors, Applied physics letters, 88(2006) 233120.
[6] G.S. M. Melli, and M. Lazzarino, Fast detection of biomolecules in diffusion-limited regime using micromechanical pillars, ACS nano, 5(2011).
[7] J.C. Richards, Signal amplification in an assay employing a piezoelectric oscillator, US patents 4847193 (1989).
[8] D.W.R.C. Ebersole, A piezoelectric crystal-based specific binding assay in which a sol is used to increase the mass of binding reagents to amplify responses to analyte, US patents 5501986, (1994).
[9] B.H. Cha, S.M. Lee, J.C. Park, K.S. Hwang, S.K. Kim, Y.S. Lee, et al., Detection of Hepatitis B Virus (HBV) DNA at femtomolar concentrations using a silica nanoparticle-enhanced microcantilever sensor, Biosensors & bioelectronics, 25(2009) 130-5.
[10] J. Joo, D. Kwon, C. Yim, S. Jeon, Highly sensitive diagnostic assay for the detection of protein biomarkers using microresonators and multifunctional nanoparticles, ACS nano, 6(2012) 4375-81.
[11] P.M. Kosaka, V. Pini, J.J. Ruz, R.A. da Silva, M.U. Gonzalez, D. Ramos, et al., Detection of cancer biomarkers in serum using a hybrid mechanical and optoplasmonic nanosensor, Nature nanotechnology, 9(2014) 1047-53.
[12] S.L. Su, I.P. Huang, W.R. Fair, C.T. Powell, W.D. Heston, Alternatively spliced variants of prostate-specific membrane antigen RNA: ratio of expression as a potential measurement of progression, Cancer research, 55(1995) 1441-3.
[13] D.G. Thompson, R.J. Stokes, R.W. Martin, P.J. Lundahl, K. Faulds, D. Graham, Synthesis of unique nanostructures with novel optical properties using oligonucleotide mixed-metal nanoparticle conjugates, Small, 4(2008) 1054-7.
[14] B.M. Reinhard, M. Siu, H. Agarwal, A.P. Alivisatos, J. Liphardt, Calibration of dynamic molecular rulers based on plasmon coupling between gold nanoparticles, Nano letters, 5(2005) 2246-52.
[15] C.M.M. Daniela Zanchet, Wolfgang J. Parak, Daniele Gerion, A. Paul Alivisatos, Electrophoretic Isolation of Discrete Au Nanocrystal/DNA Conjugates, Nano letters, 1(2001).
[16] M. Seifert, M.T. Rinke, H.J. Galla, Characterization of streptavidin binding to biotinylated, binary self-assembled thiol monolayers--influence of component ratio and solvent, Langmuir : the ACS journal of surfaces and colloids, 26(2010) 6386-93.
[17] L.G. Kjell E. Nelson, Linda S. Jung,Maximiliane S. Boeckl,Esmaeel Naeemi, Stephen L. Golledge, Tomikazu Sasaki, David G. Castner, Charles T. Campbell, and Patrick S. Stayton., Surface Characterization of Mixed Self-Assembled Monolayers Designed for Streptavidin Immobilization, Langmuir : the ACS journal of surfaces and colloids, 17(2001).
[18] L.A.W.K. J. Spinke; M. Liley; F.-J. Schmitt; H.-J. Guder, Molecular recognition at self-assembled monolayers: Optimization of surface functionalization, J Chem Phys 99(1993).

Chapter 4

Multiple functionalization system

In this chapter, a brief introduction on the most common strategies for the multiple functionalization of array based sensors is provided and the application of these strategies on micropillars arrays is discussed. A photochemical approach based on the cleavage of an amine protected thiol is proposed. Preliminary results regarding the definition of a protocol for the amine photo-deprotection, tested through the conjugation of Quantum Dots are presented. Finally, the setup developed for individual pillars functionalization, based on direct UV laser writing, is described.

4.1 The importance of the multiplexed approach

Multiplexing approach can significantly increase the performances and the applications of biomedical analysis. The possibility to measure within a single run of an analytical assay, tens of different biomolecules, enables fast analysis that are difficult to be performed with traditional single analyte[1].

One example is the rapid detection of different cytokines from human serum, that provides highly valuable clinical information to define the immune status of patients in case of inflammatory disease such as sepsis[2] and cancer[3]. Similarly, the possibility to detect in parallel different tumour biomarkers enable to focus the analysis on their ratio, whose diagnostic and prognostic utility have been demonstrated to be higher than that of the single marker in distinguishing false positive, e.g. in case of Prostate cancer [4]. In order to overcome the limitations of conventional clinical methods in their practical implementation as multiplexed monitoring approaches, protein microarrays based on fluorescence detection have been widely used, providing high-throughput functional proteomic analysis. Coupling these systems with the surface plasmon resonance effect, in 2013 Dai's group has developed a multiplexed fluorescence-enhancing microarray able to detect multiple cytokine in parallel with a sub-picomolar sensitivity [5]. Moreover, in 2015, high throughput nanoplasmonic based microarray system have been presented: Chen *at al.* developed a local surface plasmon resonance (LSPR) biosensor with 480 nanoplasmonic sensing spots in microfluidic channel arrays, and demonstrated the parallel detection of cytokines in a complex serum [6]; additionally, Sim's group implemented a multiplex device immobilizing functionalized plasmonic nanoparticles on hydrophilic-hydrophobic patterned glass slide[7].

An interesting alternative to plasmonic biochips is represented by our micropillars array. Since micropillars are fabricated in dense arrays, with the development of a strategy to functionalize different sensors with different probes and the implementation of a proper parallel read-out detection method, an platform characterized by an high degree of multiplexing can be obtained. In addition, combining this with the advantages coming from micropillars system, the demand of rapid, sensitive, and high throughput simultaneous detection can be met [8].

4.2 Multiple functionalization strategies applied to array based systems

In order to identify the right strategy to obtain a multiple functionalization of the pillars surface in the same array, the following aspects have to be considered: pillars arrays are characterized by high sensors density (588 pillars are integrated in 0,06 mm^2); the sensitive areas (top of pillars) are small, around 10 μm^2, and the functionalization method must not interfere with the stability of the CB superhydrophobic state.

Among multiple functionalization approaches for array systems reported in literature, one of the simplest methods is the *microfluidic masking*: with the help of a suitable microfluidic system, different biomolecules are deposited on selected positions of the array. An example of the principle is shown in Figure 4.1: an array of microchannels (red channels) orthogonal to the direction of the further analysis sample flux, defined by the yellow mask, is coupled with the microchip surface containing the sensing elements (blue circles); each red channel is loaded with a different molecule and therefore a different functionalization is obtained.

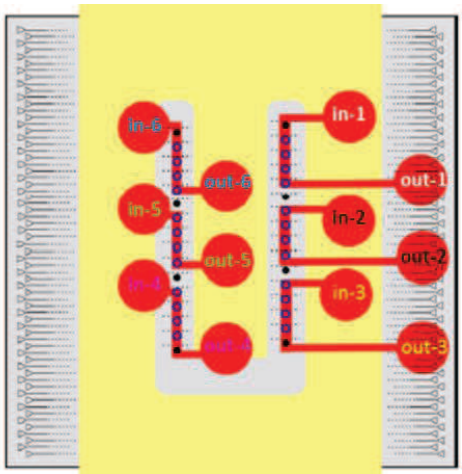

Figure 4.1 –*Schematic representation of the microfluidic masking technique. 6 microchannels represented in red, orthogonal to the subsequent analysis sample flux (yellow mask), are used to differentially functionalize six group of sensing element. Adapted from [9].*

Microfluidic masking approach has been successfully applied for multiple functionalization of microring based arrays sensors [9, 10]. However, this approach requires large volumes of reagent (ten to hundreds of microliters), in contrast with one of the strong advantages of the micropillars technique, the reduction of sample volume to few microliters. Moreover, the array functionalization is limited by the sealing footprint to confine the fluidics, therefore it cannot achieve sufficient densities to exploit the potential of a dense microarray, such as micropillars array[11].

A major ability to chemically address individual microsensing elements can be found in pin-based contact printing or in non-contact inkjet printing, both extensively used for conventional microarray functionalization, first in DNA and then in protein microarray fabrication[12]. As schematically represented in Figure 4.2a, pin-based contact printing consists on the transfer of a small volume of fluid from the tip of the pin to the sensing elements, gently touching them. Notably with this approach, delicate silicon structures

like pillars can be easily damaged by the contact. Thus, in our case non-contact methods should be preferred [13]. In inkjet non-contact technique, represented in Figure 4.2b, picolitre-sized droplets can be dispensed by spotting from a fine glass capillary positioned above the substrate surface.

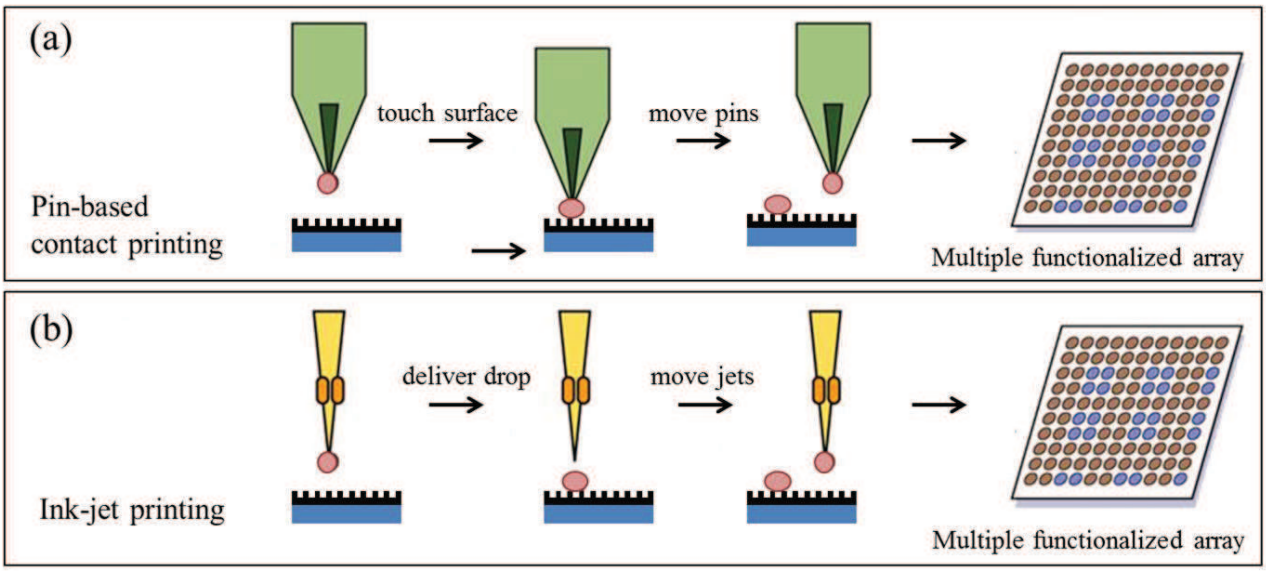

Figure 4.2 –*Schematic representation pin-based contact printing (a) and Inkjet non-contact printing(b). In pin-based contact printing the drop is deposited on the surface lightly touching it, while in inkjet printing the drop is spotted.*

In this approach the spotting accuracy is the major issue; indeed, the inhomogeneous modification of individual sensors or cross-reactivity of adjacent sensors can easily result in poor array performance. Nonetheless, the fine positional control offered by piezoelectric inkjet printers has made this approach appealing to microarray biosensor applications; in 2011 Ratner's group has demonstrated a rapid and efficient application of this strategy for the printing of bioactive protein on high density silicon microrings [11]. In the case of small sensitive areas, as the top surface of pillars (less than $10\mu m^2$) a further functionalization accuracy can be obtained by femtoliter printers [14]; on the other side, it is not guaranteed that the pressure of the spot enables the preservation of the superhydrofobic condition on the micropillars array. In addition to the alignment and contamination problems, inkjet approach is susceptible to both reduced biological activity of the immobilized ligands and nonspecific binding resulting from non-oriented immobilization of the biomolecules by physical adsorption[15].

In order to achieve a better spatial functionalization control, preserve the micropillars structure and superhydrophobicity, and provide an optimal orientation and the maximum bioactivity of the immobilized ligands, photopatterning approach has been investigated. Photopatterning is a site-specific cross-linking strategy that can be performed using either photoactivatable cross-linkers or photodeprotection of masked or "caged" reactive functional groups [15]. In particular, the use of photocleavable groups was introduced at the beginning of 90s and, exploiting the photoprotected phosporamidite chemistry, the light-generation of oligonucleotide arrays for rapid DNA sequence analysis was demonstrated[16]; today this method is commercially known as *Affymetrics GeneChip*® [17]. Figure 4.3a reports the structural formula of a

photoprotected Adenosine. In Figure 4.3b, the method is schematically represented: the chip containing photoprotected oligos is illuminated by the light passing through a photolithography mask; deprotection of the illuminated sides leads to activation and coupling of nucleosides at the specific site. The process is repeated several times in order to grow the base chain and complete the multiple probe array.

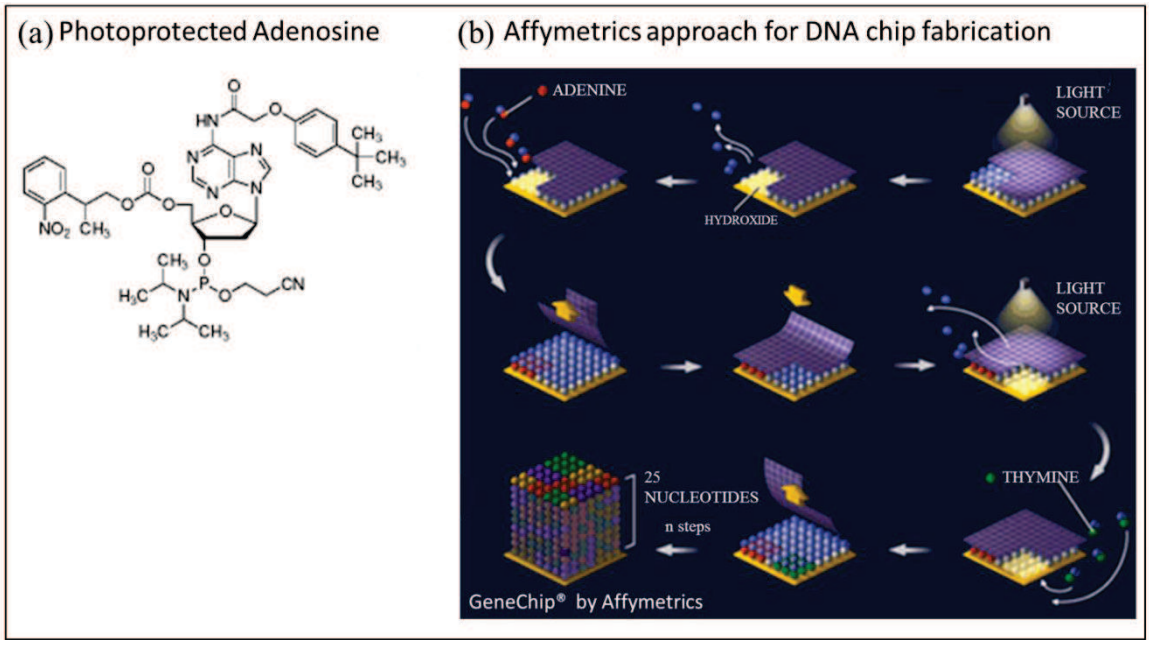

Figure 4.3 – *(a) Example of photoprotected oligo: structural formula of a photoprotected Adenosine, (b)schematic representation of Affymetrics method for DNA chip fabrication: photoprotected oligos are illuminated by the light passing through a photolithography mask; deprotection of the illuminated sides leads to activation and coupling of nucleosides at the specific site. The process is repeated as many times as requested to obtain the requested olygonuclotides.*

This approach can be extended to multiple protein functionalization, exploiting the non-covalent but highly specific immobilization strategy based on complementary oligonucleotides, named DNA-directed immobilization (DDI)[18]. Thus, after the formation of different DNA sequences on the surface, proteins conjugated with complementary DNA sequences can be immobilized to distinct attachment points of the oligonucleotide chip. Despite the potentiality of this approach, the availability of proteins conjugated with DNA oligonucleotides is required and the method becomes convenient only when hundreds of different functionalizations have to be performed.

As alternative, proteins (e.g Antibodies) can be directly covalently immobilized to the surface exploiting the crosslink between carboxyl (-COOH) and amine ($-NH_2$) groups, as done in Biacore©. In order to do this in a selective way, heterobifunctional reagents - thiols or silanes - are used to create on the surface a homogenous dense monolayer that expose chemically protected amine groups. After light exposure, the amine groups become available for further coupling with other species bearing free carboxylic groups (e.g antibodies)[19]. As already discussed in Chapter 3, the covalent bond of antibodies to the surface leads to a more robust system, avoiding binding affinity competition that can affect the further steps, like the amplification of the mass signal through the sandwich approach. Thus, the covalent bond based on the reaction between carboxyl

(-COOH) and amine (-NH_2) groups was identified as the best strategy for the functionalization of pillars with different probes.

4.3 Amine protected photocleavable thiol

With the aim of exploiting a selective covalent bind of different functionalities (e.g antibodies) on different pillars based on photodeprotection approach, the thiol photocleavable chain presented in Figure 4.4a (named compound 1) has been investigated.

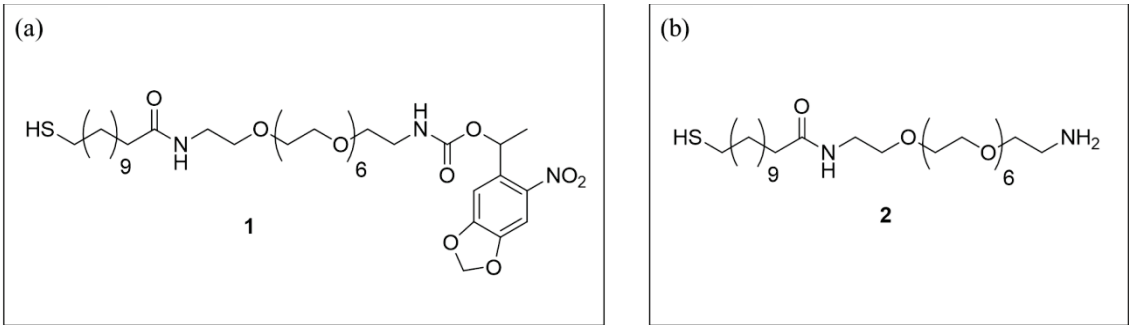

Figure 4.4 – *(a) Amine-protected form of the amphiphilic thiol reported in (b), investigated for a multiple functionalization of pillars based on the covalent bind of different antibodies thought a photodeprotection approach.*

This molecule, synthetized by the group of *Prof. Lucia Pasquato, University of Trieste*, is the amine-protected form of the amphiphilic thiol reported in Figure 4.4b (compound 2) terminating with a free amino group. This amine protected thiol can be used for SAMs preparation and, after photodeprotection, the amino group is available for coupling with carboxylic groups. The synthesis is outlined in Scheme 4.1.

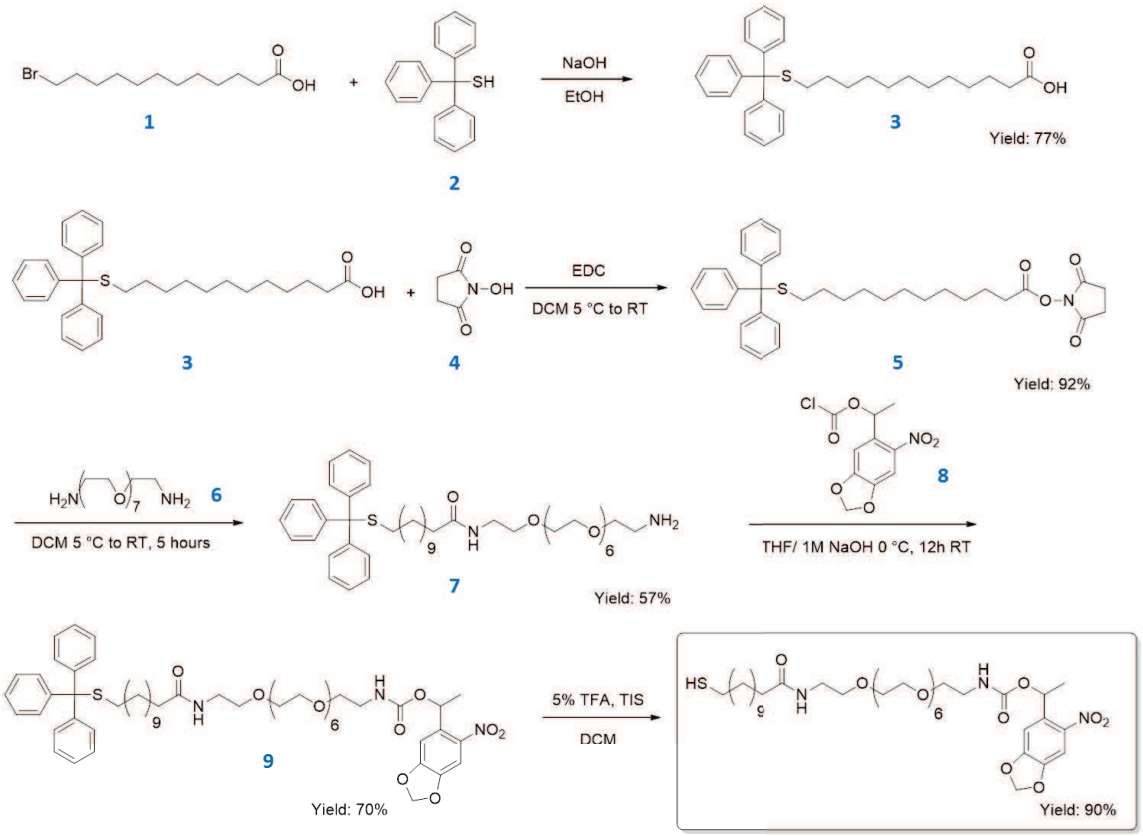

Scheme 4.1 –*Scheme of synthesis of the amine-protected thiol reported in Figure 4.4.*

Briefly, the commercially available 12-bromododecanoic acid **1** was reacted with triphenylmethanethiol **2** affording the trityl protected 12-mercaptododecanoic acid in 77% isolated yield. The synthetic procedure was adapted from one by Sawamura's group in [20] using two equivalents of base; the first equivalent is used to deprotonate the carboxylic acid, while the second equivalent is used to deprotonate the triphenylmethanethiol. The thiolate anion thus generated gives an SN_2 reaction on the 12-bromododecanoic acid affording product **3**. This intermediate was converted to the active ester **5** by a standard procedure employing EDC as coupling agent and *N*-hydroxysuccinimide. The active ester **5** was reacted with an excess of α,ω- bis-amino octa(ethylene glycol) affording the amine **7** in 57% yield. The amino function of compound **7** was protected by using the commercially available MeNPOC-chloride **8** according to a procedure reported by A. Gautier *at al*.[21]; the fully protected amino thiol **9** was obtained in 70% yield. The deprotection of the thiol group was achieved by a standard procedure employing 5% trifluoroacetic acid in methylene chloride in the presence of two equivalents of triisopropylsilane as scavenger for the trityl cation; the amine protected thiol was obtained in 90% yield.

The structure of the amine protected thiol, Figure 4.4a, was conceived in order to be modular: the hydrocarbon chain next to the thiol group has to be long enough in order to provide stable and compact monolayers, and since this stability mainly arise from the van der Waals interactions established by neighboring methylene groups, any alkyl chain longer than eight methylene units could be used. The

hydrophilic part of the molecule comprises a relatively long polyethylene oxide unit, and also its length can be varied with limited synthetic effort, since a variety of α,ω-PEG diamines are commercially available.

The photocleavable protecting group has been chosen among the derivatives of *o*-nitrobenzyl alcohol, which are the most commonly used for this application. Indeed, the 2-nitrobenzyl functionality is the most widely used photoremovable protecting group for application in synthesis[22] and photolithography, with focus on DNA microarrays[23]. In seeking an improvement in the photocleavage process, several protecting groups based on the scaffold of *o*-nitrobenzyl alcohol have been proposed and among them NVOC (6-nitroveratryloxycarbonyl), MeNVOC (methyl-6-nitroveratryloxycarbonyl) and MeNPOC (α-methyl-(6-nitropiperonyloxymethyl)) found wide application, Figure 4.5.

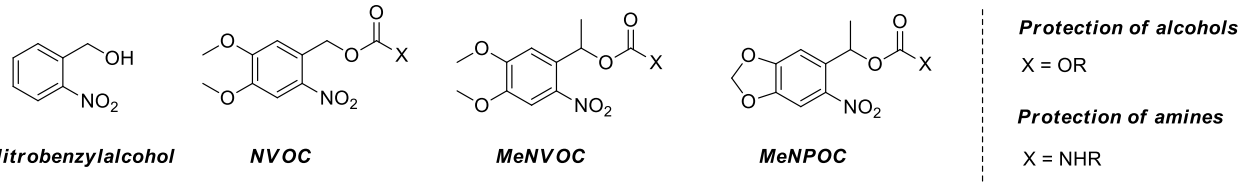

Figure 4.5- *Structures of o-nitrobenzyl alcohol and of common photolabile protecting groups derived from its scaffold.*

The use of MeNPOC is advantageous with respect to its analogues because of the higher quantum yield of the photodeprotection process; photocleavage can be achieved by irradiation at 365 nm. A solution phase comparison of the release quantum yield of thymidine derivatives of NVOC and MeNPOC reveals a 5.7-fold enhancement in favour of MeNPOC ($\Phi_{MeNPOC} = 0.0075$; $\Phi_{NVOC} = 0.0013$)[24].

4.3.1 Mechanism of photodeprotection

The photodeprotection of the MeNPOC group, with reference to protected amines, takes place with the mechanism briefly sketched in Figure 4.6. The photoreaction is initiated by an intramolecular 1,5-H shift yielding the *aci*-nitro tautomer **II** as primary photoproducts. A short lived benzisoxazolidine **III** obtained by cyclization from the intermediate **II** is generally assumed to be formed in the next step. Ring opening of compound **III** releases 2-nitrosobenzophenone and the carbamic acid **IV** that undergoes spontaneous decarboxylation to the final amine product **V**.

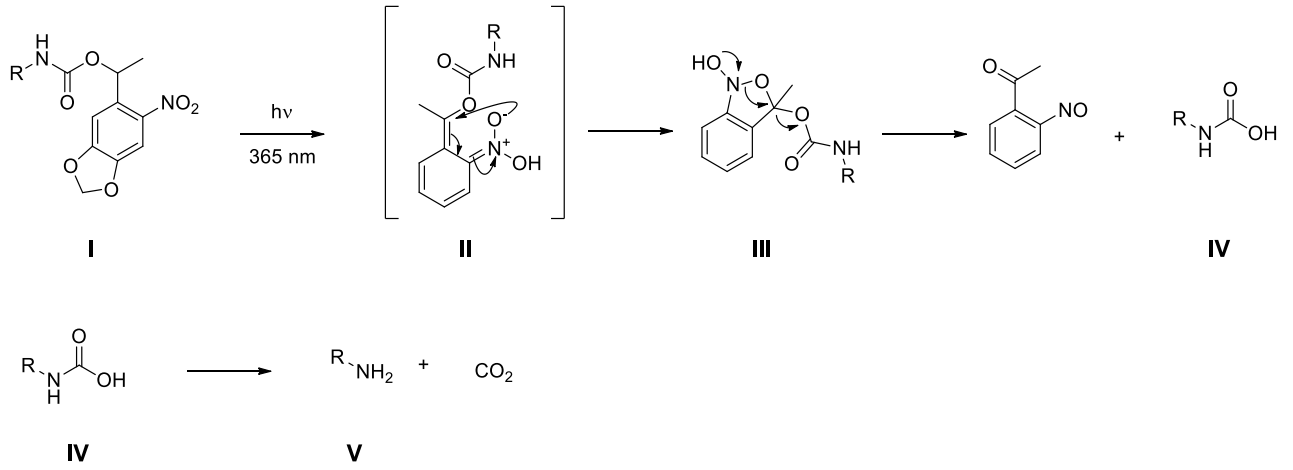

Figure 4.6- *Mechanism for the photocleavage of MeNPOC protected amines.*

Although the mechanism is reasonable, the reactions following the primary photoexcitation leading to release of the unprotected amine are not well understood, and a description of the exact cleavage mechanism still awaits clarification. A detailed mechanistic investigation has been performed for the photocleavage of 2-Nitrobenzylmethyl and ethyl ethers[25] that may be taken as models for the various derivatives of *o*-nitrobenzyl alcohol including MeNPOC. In this study the authors report that after photoabsorption, three different reaction pathways for the release of the photocleavage products are possible according to the nature of the reaction medium (solvent, pH and buffer concentration), making the mechanism reported in Figure 4.6 an oversimplification.

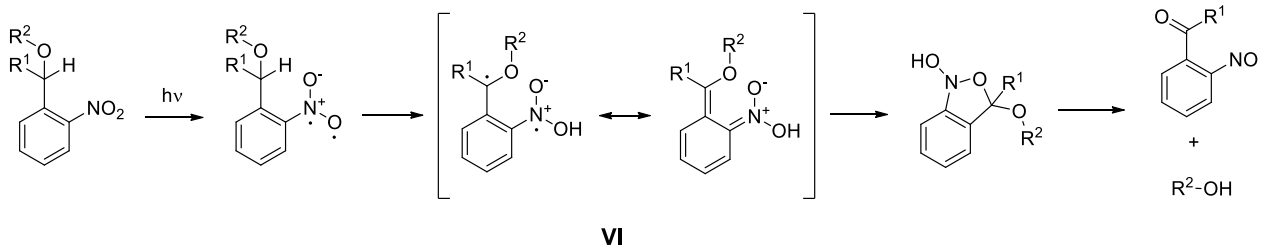

Figure 4.7- *Sequence of reactions following the initial photoexcitation of 2-Nitrobenzyl-alkyl ethers.*

As for the MeNPOC derivatives, the photocleavage of 2-Nitrobenzylmethyl ether takes place with the initial intramolecular H-atom transfer affording *aci*-nitro tautomer **VI**, Figure 4.7, but the intermediate **VI** may evolve to products in three different ways, according to its protonation state, Figure 4.8.

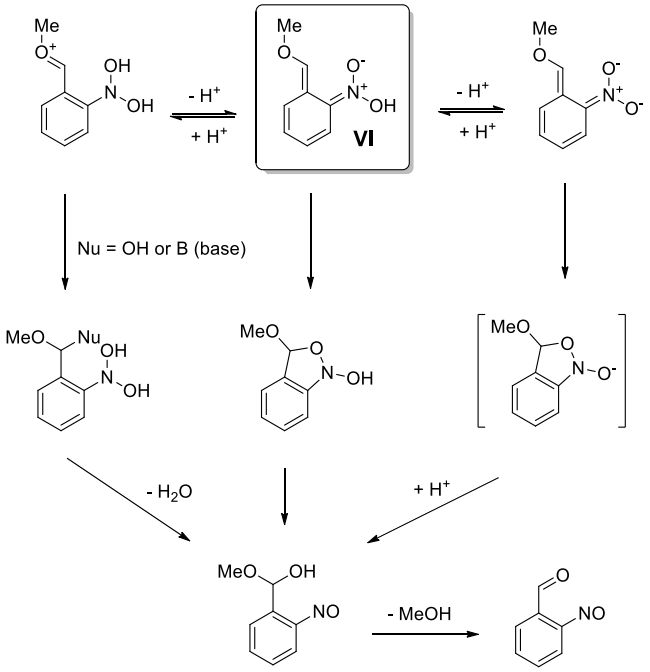

Figure 4.8- *Revised mechanism for the photocleavage of 2-Nitrobenzyl-alkyl ethers.*

The efficiency of the photocleavage is therefore expected to dependent on the pH of the medium; the authors report that in general higher reaction rates are observed at low pH values.

4.3.2 Solution phase photodeprotection test

The viability of the photocleavage on the amine protected thiol has been preliminary evaluated in solution, determining the change in molecular mass after UV exposure by means of electrospray ionisation mass spectrometry (ESI-MS); the analysis have been performed with a Perkin Elmer APII at 5600 eV.

The protected amine thiol was diluted in methanol at the concentration 0.1 mg/mL and irradiated with a UV-laser at 375nm (LBX-375, Oxxius Laser). Based on what reported in literature regarding the cleavage of other *o*-nitrobenzyl derivatives (e.g NVOC) [19] and considering an elliptical cross section of the beam of circa 0,1cm^2, the power was set at 5mW. Thus, using a fixed intensity of 50mW/cm^2, three doses have been tested, using three different exposure times: 3, 10 and 30 minutes. The three related mass spectra are reported in Figure 4.9.

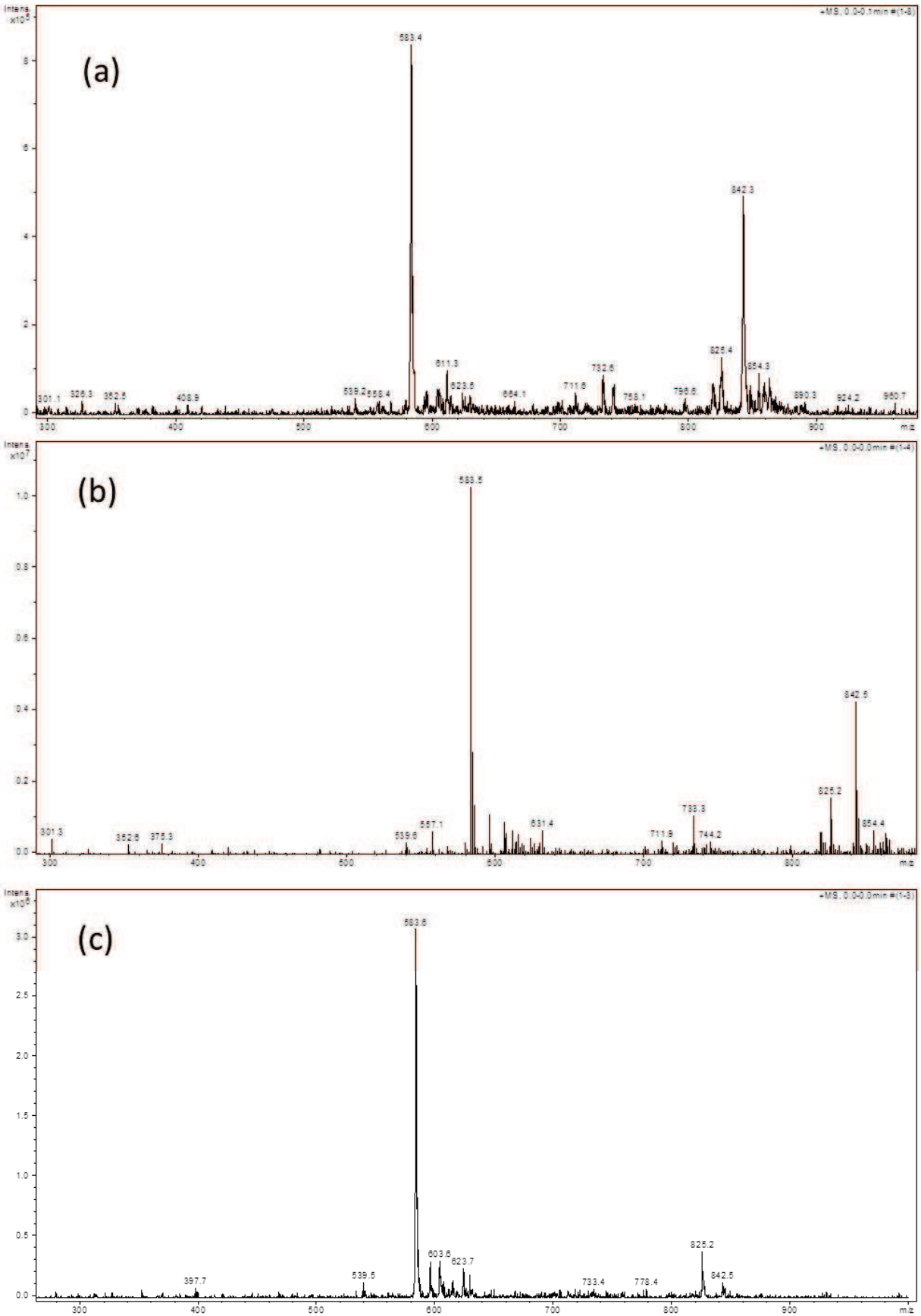

Figure 4.9-*Mass spectra analyses for the photodeprotection of amine protected thiol after irradiation with light at 365nm, for different exposition times (a): 3 minutes, (b) 10 minutes, (c) 30 minutes. The experiment was run on a 0.1 mg/mL solution of Compound 1 in methanol. Mass spectra recorded by Dr. Fabio Hollan, Department of Chemical and Pharmaceutical Sciences, University of Trieste.*

After three minutes of irradiation the cleavage of the protecting group is clearly evident from the mass spectra, Figure 4.9a, with the appearance of a peak at m/z = 583.4 corresponding to the mass of the product with the free amine plus one hydrogen ion $[M+H]^+$; the presence of the protected compound is also evident at m/z = 842.3 and m/z = 825.4 corresponding to the masses of the starting material plus one Na^+, $[M+Na]^+$, and plus one hydrogen ion $[M+H]^+$ respectively. A similar composition can be observed after 10 minutes of irradiation, Figure 4.9(b). After 30 minutes, Figure 4.9(c), the starting material was almost completely photo-converted.

4.4 Photocleavage on the surface: Quantum Dots conjugation test

In order to test the cleavage process of the amine protected thiol, immobilized on a surface as self-assembled monolayer, one possible and fast strategy consists in using Quantum Dots (QDs) fully coated with carboxyl groups (-COOH). These QDs are conjugated to the amine groups ($-NH_2$) exposed by the surface after the photo-deprotection, and their presence is evaluated through fluorescence images. To be sure that the results obtained by the analysis are influenced only by the cleavage process, a QDs conjugation protocol was first set on surfaces fully coated with $-NH_2$; afterwards the same protocol was applied to test the efficiency of photo-deprotection of the amine groups in different conditions.

5nm Quantum CdxSe1-x/ZnS core/shell fluorescent nanocrystals coated with –COOH functional ligands(QDs-COOH) soluble in water and aqueous buffers, were purchased by Cytodiagnostic (FN-665-C - TriliteTM Fluorescent Nanocrystals 665nm – Carboxy, Emission (λ max): 665±5nm, FWHM 30-40nm). The nanocrystals are fully coated; in addition to the carboxyl ligand (approximately 25 functional groups per nanocrystal), the remaining available surface area has been coated with a small hydroxyl ligand as backfiller.

The conjugation between QDs-COOH and NH_2 was performed in phosphate buffered saline (PBS), exploiting the well-known carbodiimide-amine conjugation chemistry, and in particular N-(3-Dimethylaminopropyl)-N′-ethylcarbodiimide hydrochloride (EDC, SigmaAldrich E7750) was used as mediator.

In the first step, the COOH activation, EDC reacts with the carboxylic acid groups present on the QDs to form an active O-acylisourea intermediate; this is easily displaced by nucleophilic attack from primary amino groups in the reaction mixture (conjugation step). Thus, the primary amine forms an amide bond with the original carboxyl group, and an EDC by-product is released as a soluble urea derivative. The O-acylisourea intermediate is unstable in aqueous solutions, thus it is generally stabilized with N-hydroxysuccinimide (NHS), but since in our case the activated QDs could immediately be exposed to the NH_2, there is no need of this additional stabilization. Molecular ratios COOH:EDC and NH_2:COOH, and pH value have been set according to the following observations reported by D. A. East *at al.* in [26]: “Carbodiimide coupling procedures are carried out at an acid pH range 3.0-5.0, while the coupling reaction must be performed with a basic pH between 7.5 and 9”, and considering that the used QDs are stable in a pH range between 6 and 9.

Conjugation protocol

- activation step: a small quote of QDs-COOH was diluted in PBS at pH 6, the minimum to guarantee the stability of QDs. A fresh prepared solution of EDC in water is added to QDs, with a molar ration COOH:EDC of 1:2000. The reaction is performed at RT for 15min.

- conjugation step: the surface containing NH_2 (Silica beads or micropillars array, see next paragraph) is immersed in a PBS solution at pH 7.8. A certain quantity of activated QDs are added according to the molecular ratio NH_2:COOH=1:2; the reaction is performed for 2h at RT.

4.4.1 QDs-COOH conjugation protocol tested on NH_2 Silica beads

The protocol described above has been used to conjugate QDs-COOH to silicon beads fully coated with NH_2 group (beads diameter: 800nm). A 70µM solution of silica beads in PBS at 7.8pH, corresponding to 500pmol of NH_2, has been exposed to activated and non-activated QDs. The success of the conjugation protocol has been evaluated performing Fluorescence-activated cell sorting-FACS Analysis by BD FACSCalibur™ to distinguish the silica beads that were conjugated with QDs. Figure 4.10 shows the histogram of counts as function of the fluorescence intensity (APC= Emission 657.5nm); spectra of Silica particles (a) and Silica particles treated with not-activated QDs (b) are used as negative controls, and compared with the positive one Silica particles conjugated with activated QDs (c).

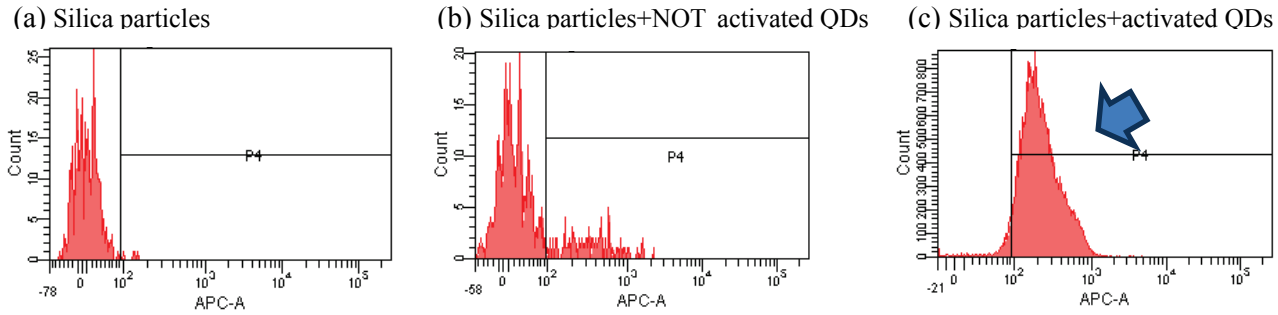

Figure 4.10 *–FACS Analysis:histogram of counts as function of the fluorescence intensity (APC= Emission 657.5nm). Spectra of Silica particles (a), particles treated with not-activated QDs (b) and conjugated with activated QDs (c). FACS analysis performed by Dr. Giulio Fracasso, University of Verona.*

In the histogram for silica beads, the maximum intensity is 10^2. For silica beads treated with not-activated QDs the histogram is comparable to the previous one, with few counts in the range of intensity between 10^2 and 10^3, suggesting a slight aspecific binding, while only silica beads treated with activated QDs show an histogram above the negative axis, confirming the successful conjugation of at least 90-95% of the beads population.

4.4.2 QDs-COOH conjugation protocol tested on NH_2 pillars surface

For a further confirmation of its the validity , the conjugation protocol has been applied to bind QDs-COOH to micropillars exposing NH_2 groups on their top.

Micropillars array, previously coated with a thin layer of gold, have been incubated overnight at 4°C with a solution of amine thiol (11-Amino-1-undecanethiol hydrochloride, Sigma Aldrich 674397) at @100µM in ethanol; micropillars array were rinsed with ethanol, and then dried with N_2. The obtained substrate has been estimated to have circa 42 pmol of NH_2 on the whole chip. Both the pillars coated only with gold and the ones functionalized with NH_2 have been treated with not-activated and activated QDs, following the protocol described above. After that, the samples were rinsed in mQ water and dried with N_2.

The presence of QDs on the surface was evaluated through fluorescence images. The sample was mounted on an inverted optical microscope (Zeiss Axiovert 200) equipped with Xenon lamp and filters for fluorescence microscopy, and the images were performed in reflection geometry. Samples were illuminated with a lamp x-cite 120, through a Zeiss objective (Alpha Plan-Fluar 100x/1.45 Oil, WD=0.11mm); the Zeiss Filter Set 25 was used to split the light. Finally, the photoluminescence signal is detected by a DVC CCD camera.

Figure 4.11 shows the fluorescence images, acquired with 10 seconds of exposure to avoid signal saturation, corresponding to: a micropillars array coated with gold (Figure 4.11a); the same substrate incubated with activated QDs (Figure 4.11b); micropillar array coated with NH_2 and exposed to not-activated QDs (Figure 4.11c); and finally, the same array exposed to activated QDs (Figure 4.11d).

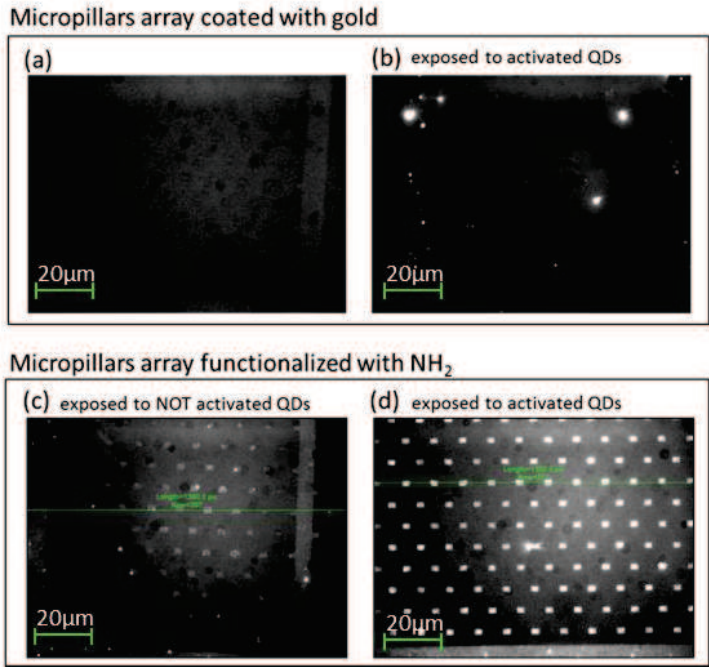

Figure 4.11 *–Fluorescence images acquired with 10 seconds of exposure: (a) a micropillars array coated with gold, (b) a micropillars array coated with gold and incubated with activated QDs; (c) a micropillars array coated with NH_2 and exposed to not- activated QDs(c) and activated QDs(d).*

Figure 4.11a and 4.11b confirm that no fluorescence signal can be detected from the gold deposited on pillar surface, as well as after the exposure of this substrate to activated QDs. Instead, the success of the conjugation is confirmed in case of NH_2 surface exposed to activated QDs. Indeed, in Figure 4.11(d), on the top of pillars a strong fluorescence can be detected, while the exposure of NH_2 surface to not-activated QDs causes only a slight non-specific signal; this is confirmed from Figure 4.12, that compares the graph of the intensity recorded on a cross section of the fluorescence image 4.11c (red line on the graph) with the one of 4.11d (dark line on the graph).

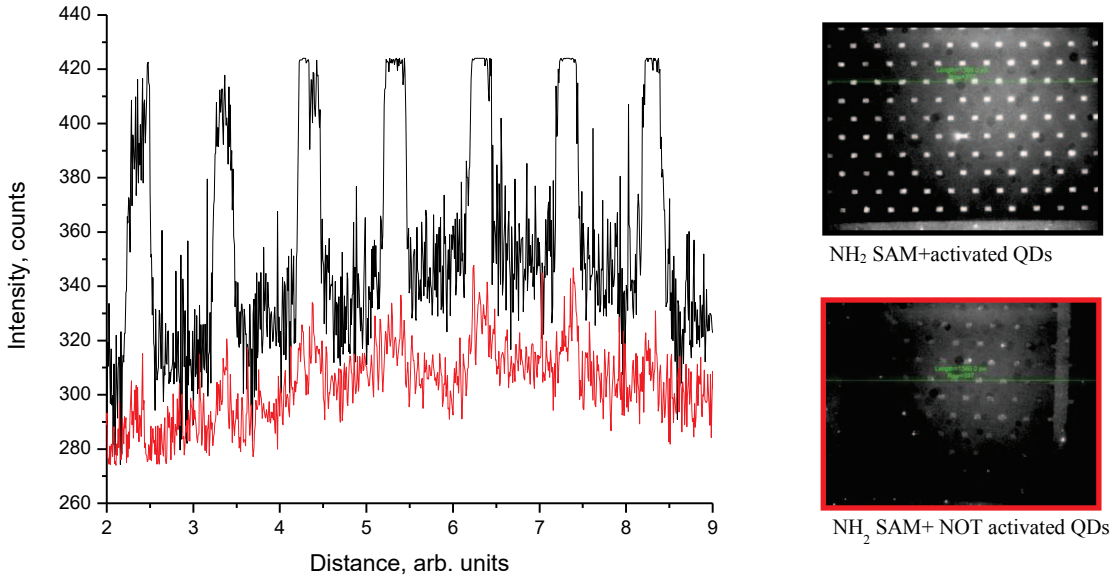

Figure 4.12 – *Comparison between the intensity recorded on a cross section of the fluorescence image reported in Figure 4.11c, (red line on the graph) and that one of the image reported in Figure 4.11d, (dark line on the graph).*

4.4.3 Photocleavage conditions tested with QDs-COOH conjugation

After its validation, the QDs-COOH – NH2 conjugation protocol has been used to evaluate the efficiency of cleavage, and consequently the activity of the NH_2 deprotected groups in binding free COOH.

For a faster preliminary evaluation, patches of gold deposed on silicon have been used as substrate for the formation of the SAM of amine protected thiol, only the few mm^2 of gold on the silicon substrate have been involved in the further processes. Samples were incubated overnight at 4°C with a solution of amine protected thiol at 100µM in ethanol. After that, the substrates have been rinsed with EtOH, dried with N_2 and used for exposure experiments.

The exposition has been performed with a mercury lamp having the main line at 365nm, with an intensity of $7mW/cm^2$. According to the data reported in literature[19, 27], the dose was set at $6J/cm^2$, thus the exposure time was fixed at 14min. The exposition has been performed in liquid, keeping the sample immersed in PBS. Three pH conditions have been tested: 6, 7 and 8, and one sample was not exposed to the UV light. After the

exposition, sample were rinsed two times with the buffer at the same pH, and one time with PBS at 7pH, in order to neutralize the pH for the further steps. The samples are immersed in eppendorf containing PBS at pH 7.8, in which the conjugation was performed following the protocol described in §4.4. After the conjugation step, samples were rinsed in mQ water and dried with N_2, and the presence of QDs was evaluated by fluorescence following the same procedure described in §4.4.2.

The fluorescence images are crop to analyse for all samples a sub-area of the gold patch; screen shots are reported in Figure 4.13.

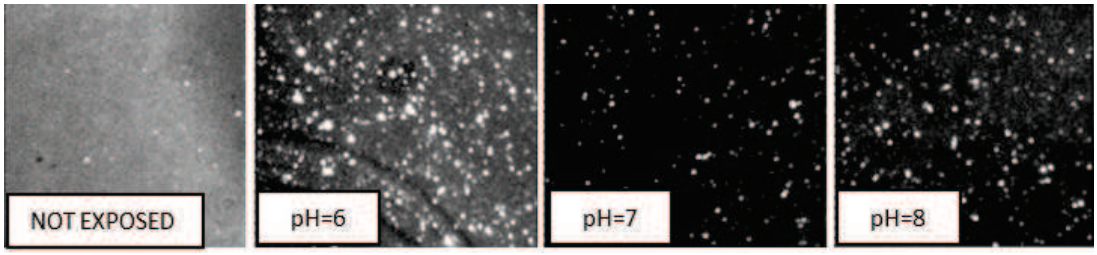

Figure 4.13 – *Screen shots: crops of the fluorescence images used to evaluate the fluorescence intensity as function of the three pH investigated in the cleavage process.*

The crop of the image has been converted in 3D array by Gwyddion software, statistically analysed to obtain an intensity distribution. In figure 4.14 the intensity distribution of the not exposed samples is shown. The slight signal is due to the gold patch and is expected to be constant for all the 4 samples.
The average value is 0.027, the maximum intensity is around 0.1; therefore, in figure 4.15, where the intensity distributions of the 4 sample are compared, only values above 0.1 are considered.

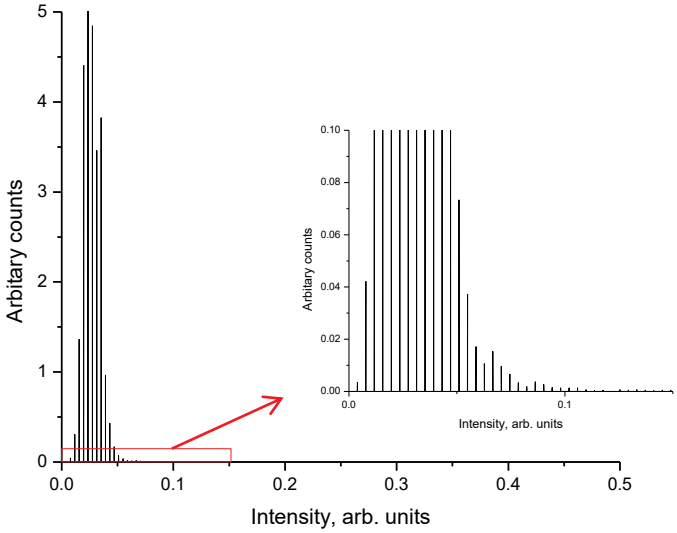

Figure 4.14 – *The intensity distribution of the not exposed samples. The average value is 0.027, the maximum intensity is around 0.1.*

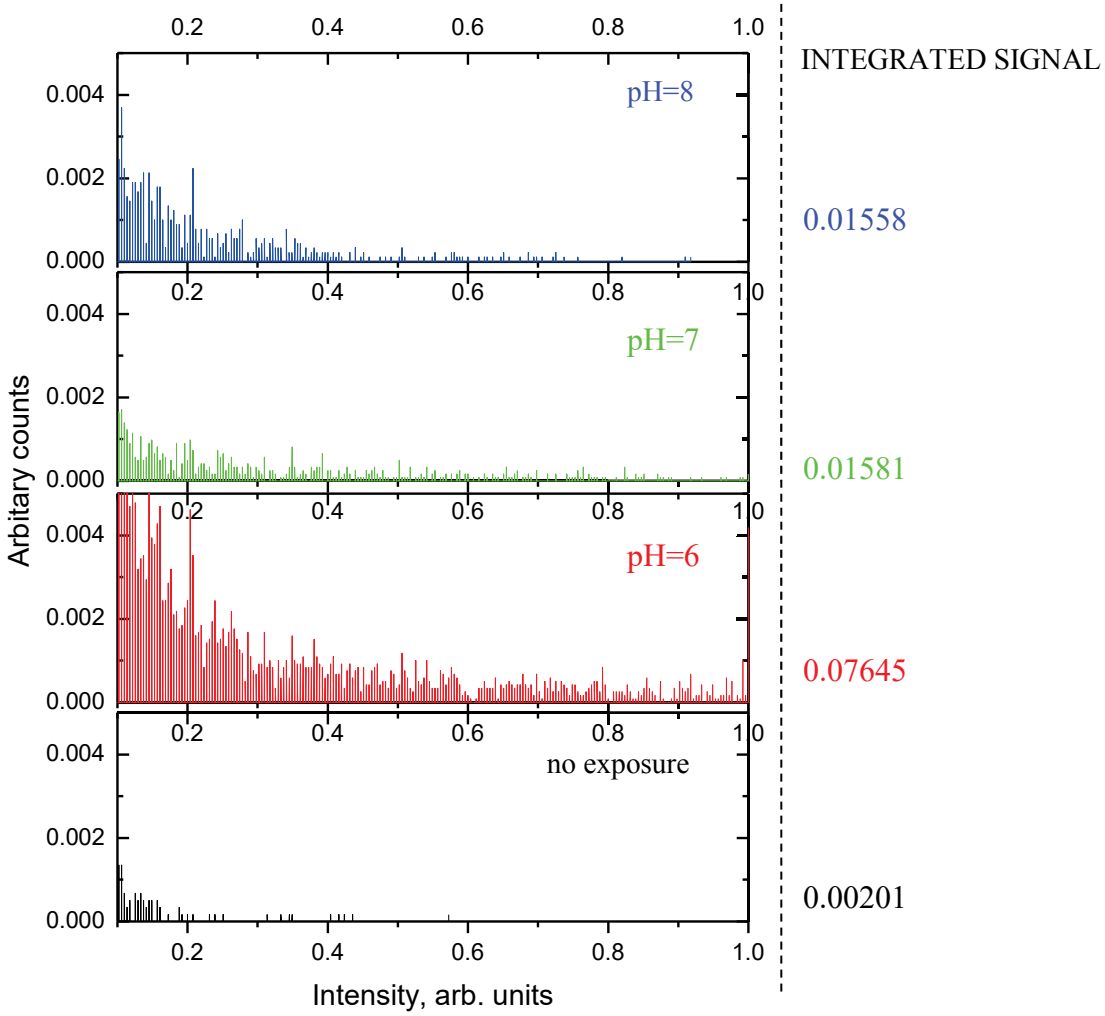

Figure 4.15 *–Intensity distributions of samples cleaved at different pH: pH8 (first graph, blue), pH7 (second graph, blu) , pH6 (third graph, green) and not exposed (last graph, dark). The intensity distribution are shown above 0.1 value of intensity, considered the maximum intensity given by the gold surface. To the right of each graph, the integrated signal calculated over the entire distribution is reported.*

For a better evaluation of the differences between the distributions, for each one the integrated signal has been calculated over the entire distribution and reported to the side of the related graph. The integrated signal recorded after cleavage at low pH is 50 times higher than the one recorded with the cleavage performed at neutral or basic pH. This is in accordance with what described in 4.3.1 regarding the influence of the pH on the cleavage efficiency.

4.5 Selective exposure of pillars

After the definition of proper cleavage and coupling protocols, the next aim is the selective exposure of individual pillars. The implementation of a traditional masking approach would be complicated, due to alignment issues correlated to the high density of pillars array; therefore a UV laser writing strategy has

been implemented. As schematically represented in Figure 4.16, considering a pillar array, on which a self-assembled monolayer of the amine terminated thiol has been formed, the UV laser is focused on the top of pillar1, exposing only it to the light. On this pillar, the amine groups are deprotected, thus incubating the sample with species having free –COOH group (QDs or Abs), they can be conjugated to the NH_2 available on pillar . Sample is moved and the laser is focalized on another pillar (e.g. pillar 2). Repeating the previous steps, changing the functional element, a multiple selective functionalization can be obtained.

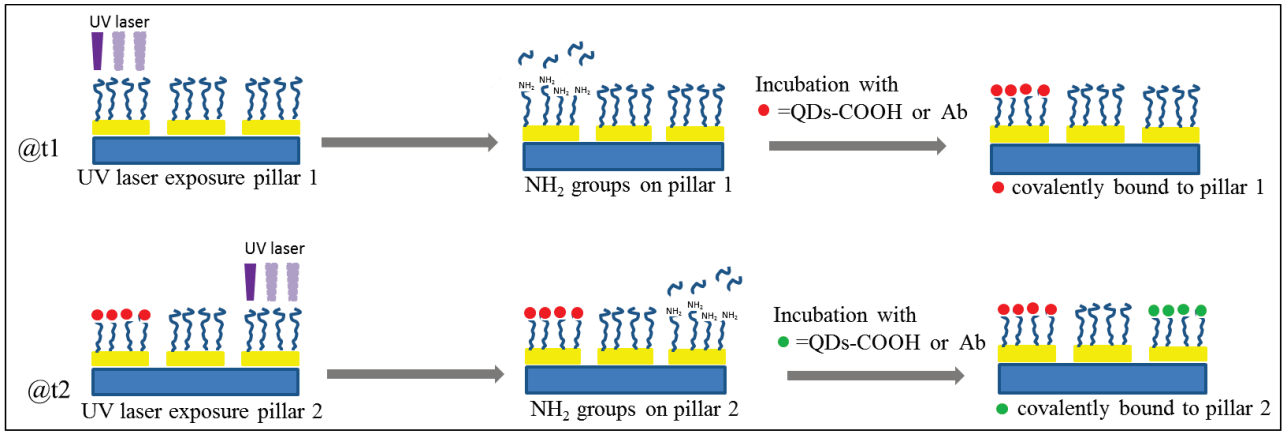

Figure 4.16 – *Schematic representation of the UV laser writing principle.*

In order to implement the strategy illustrated above, a dedicated setup of exposure has been developed.
A schematic representation of the operational mode is reported in Figure 4.17a, while in Figure 4.17b an image of the experimental setup is shown.

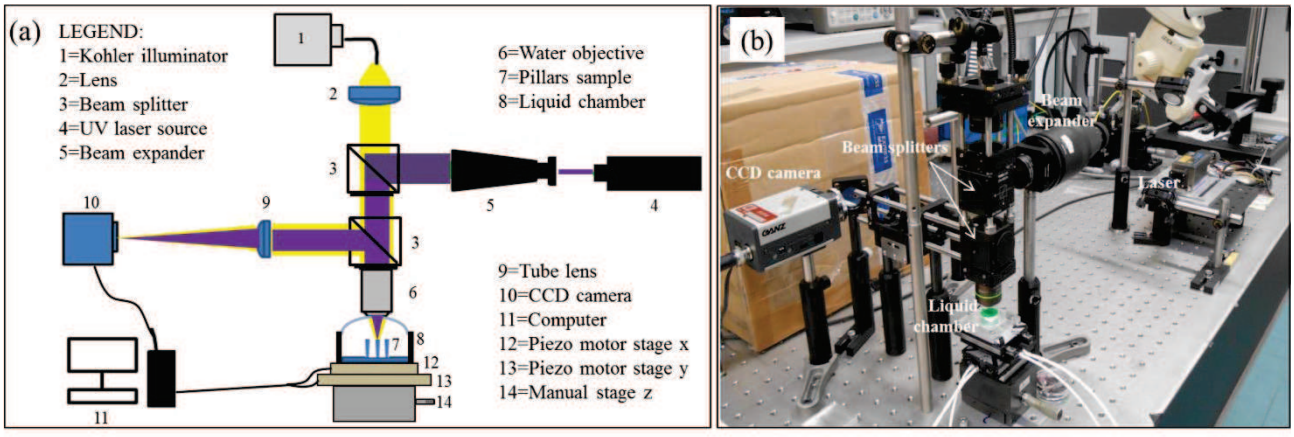

Figure 4.17 - *Scheme of the setup for selective UV pillar exposure. (b) Image of the experimental setup.*

A micropillars array sample is loaded in a liquid chamber, mounted on two piezo-motor stages (Linear Piezo Stage LPS-65, Pimicos) controlled by Driver E-861, enabling the x, y positioning of the sample (on the table plane) with subnanometer resolution; x, y stages are mounted on a manual z stage.

An UV laser source (LBX-375-Oxxius, wavelength 375 nm, max power = 15 mW) and a white light source are focused by a water objective (OLYMPUS LUMPlanFL/Ir, magnification 60x, numerical aperture 0.90, working distance 1.5mm) on the top of a pillar, the laser beam spot is estimated to be about 200nm; the liquid chamber is open and the objective is immersed in liquid. In order to have an uniform laser illumination on the objective pupil, before to enter to the objective, the laser is expanded with a 10x beam expander, allowing also the control of the spot size and shape of the laser. The alignment of the laser beam with the beam expander is obtained by two mirrors mounted on adjustable supports and placed after the laser source. Above the objective, two 50:50 beam splitters are placed; the top one conveys the laser beam on the sample, the bottom one reflects the sample image on image the CCD (½ in. DBK 41BU02, Pyramid Imaging, US), passing through a tube lens (focal length of 200 mm) that focalizes the infinitive corrected image exiting from the objective.

The xy piezostage, the laser power and on/off switching mode are controlled by a Labview program. First the coordinates of one corner of the array are acquired, then it is possible to address any of the pillars of the array. The repositioning precision is limited by the piezostage performances and is in our case better than 100nm. The lateral resolution is 5nm which allows the production of arbitrary patterns. The laser exposition path on the single pillar (Figure 4.18) , is performed on the base on a predefined matrix of points.

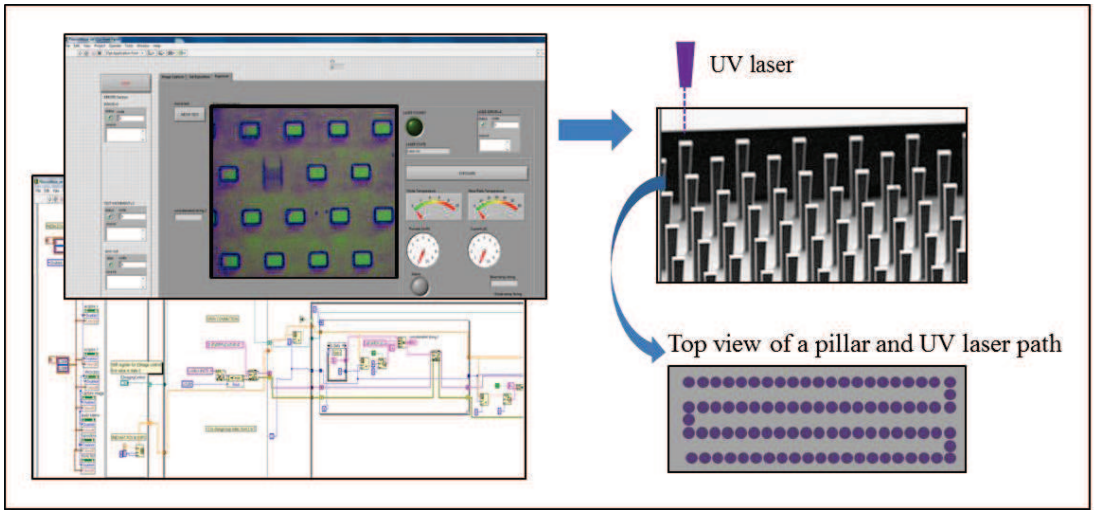

Figure 4.18 – *Representation of the operations performed by the Labview program. To the right, a schematic image of the UV writing path is reported.*

Due to multiple reflections and splitting along the optical path, the power of the laser recorded after the objective is reduced by a factor 1000, ranging from 2,7 to 20 µW. Considering the small spot area, 0,05 μm^2 of the focalized laser, even with the use of optical filters, the laser intensity recorded on the sample is 500 times higher than values reported in literature[19, 27]. During preliminary experiments the definition of a proper exposition dose has been investigated, but no positive results were obtained and further investigations of the effect of the high intensity is necessary.

References:

[1] D. Falconnet, J. She, R. Tornay, E. Leimgruber, D. Bernasconi, L. Lagopoulos, et al., Rapid, sensitive and real-time multiplexing platform for the analysis of protein and nucleic-acid biomarkers, Analytical chemistry, 87(2015) 1582-9.

[2] V.A.D. Steven M. Opal, Anti-Inflammatory Cytokines, Chest, 117(2000).

[3] B.E. Lippitz, Cytokine patterns in patients with cancer: a systematic review, The Lancet Oncology, 14(2013) e218-28.

[4] S.L. Su, I.P. Huang, W.R. Fair, C.T. Powell, W.D. Heston, Alternatively spliced variants of prostate-specific membrane antigen RNA: ratio of expression as a potential measurement of progression, Cancer research, 55(1995) 1441-3.

[5] B. Zhang, J. Price, G. Hong, S.M. Tabakman, H. Wang, J.A. Jarrell, et al., Multiplexed cytokine detection on plasmonic gold substrates with enhanced near-infrared fluorescence, Nano research, 6(2012) 113-20.

[6] P. Chen, *et al.*, Multiplex Serum Cytokine Immunoassay Using Nanoplasmonic Biosensor Microarrays, ACS nano, 9(2015) 4173–4181

[7] J.U. Lee, A.H. Nguyen, S.J. Sim, A nanoplasmonic biosensor for label-free multiplex detection of cancer biomarkers, Biosensors & bioelectronics, 74(2015) 341-6.

[8] K.D. Barbee, A.P. Hsiao, E.E. Roller, X. Huang, Multiplexed protein detection using antibody-conjugated microbead arrays in a microfabricated electrophoretic device, Lab on a chip, 10(2010) 3084-93.

[9] A.L. Washburn, M.S. Luchansky, A.L. Bowman, R.C. Bailey, Quantitative, label-free detection of five protein biomarkers using multiplexed arrays of silicon photonic microring resonators, Analytical chemistry, 82(2010) 69-72.

[10] C.F. Carlborg, K.B. Gylfason, A. Kazmierczak, F. Dortu, M.J. Banuls Polo, A. Maquieira Catala, et al., A packaged optical slot-waveguide ring resonator sensor array for multiplex label-free assays in labs-on-chips, Lab on a chip, 10(2010) 281-90.

[11] J.T. Kirk, G.E. Fridley, J.W. Chamberlain, E.D. Christensen, M. Hochberg, D.M. Ratner, Multiplexed inkjet functionalization of silicon photonic biosensors, Lab on a chip, 11(2011) 1372-7.

[12] V. Romanov, S.N. Davidoff, A.R. Miles, D.W. Grainger, B.K. Gale, B.D. Brooks, A critical comparison of protein microarray fabrication technologies, The Analyst, 139(2014) 1303-26.

[13] T.C. Tisone and J. L. Tonkinson, Protein Microarrays, Ch.10, pp. 169–177: Jones and Bartlett Publishers; 2005.

[14] D. Witters, K. Knez, K. Janssen, B. Verbruggen , R. Puers, J. Lammertyn, High-Throughput Patterning of Single Magnetic Beads Using Digital Microfluidic Technology, Lab on a chip, 11(2011) 1495-7.

[15] X.H. Liu, H.K. Wang, J.N. Herron, G.D. Prestwich, Photopatterning of antibodies on biosensors, Bioconjugate chemistry, 11(2000) 755-61.

[16] A.C. Pease, D. Solas, E.J. Sullivan, M.T. Cronin, C.P. Holmes, S.P. Fodor, Light-generated oligonucleotide arrays for rapid DNA sequence analysis, Proceedings of the National Academy of Sciences of the United States of America, 91(1994) 5022-6.

[17] J.W. Engels, Gene synthesis on microchips, Angewandte Chemie, 44(2005) 7166-9.

[18] L. Gogolin, H. Schroeder, A. Itzen, R.S. Goody, C.M. Niemeyer, C.F. Becker, Protein-DNA arrays as tools for detection of protein-protein interactions by mass spectrometry, Chembiochem : a European journal of chemical biology, 14(2013) 92-9.

[19] A. Buxboim, M. Bar-Dagan, V. Frydman, D. Zbaida, M. Morpurgo, R. Bar-Ziv, A single-step photolithographic interface for cell-free gene expression and active biochips, Small, 3(2007) 500-10.

[20] D.S. Shin, K.N. Lee, K.H. Jang, J.K. Kim, W.J. Chung, Y.K. Kim, et al., Protein patterning by maskless photolithography on hydrophilic polymer-grafted surface, Biosensors & bioelectronics, 19(2003) 485-94.

[21] A. Gautier, D.P. Nguyen, H. Lusic, W. An, A. Deiters, J.W. Chin, Genetically encoded photocontrol of protein localization in mammalian cells, Journal of the American Chemical Society, 132(2010) 4086-8.

[22] Pillai, V. N. R. Synthesis 1980, 1-26. Greene, T. W.; Wuts, P. G. M. Protective Groups in Organic Synthesis, 3rd ed.; Wiley-Interscience: New York, 1999.

[23] Pirrung, M. C. Angew. Chem., Int. Ed. 2002, 41, 1276-1289.

[24] P.V. Berroy, M. L.; Carre, M. C. Sens. Actuators, B 2001, B74, 186.

[25] Y.V. Il'ichev, M.A. Schworer, J. Wirz, Photochemical reaction mechanisms of 2-nitrobenzyl compounds: methyl ethers and caged ATP, Journal of the American Chemical Society, 126(2004) 4581-95.

[26] D.A. East, D.P. Mulvihill, M. Todd, I.J. Bruce, QD-antibody conjugates via carbodiimide-mediated coupling: a detailed study of the variables involved and a possible new mechanism for the coupling reaction under basic aqueous conditions, Langmuir : the ACS journal of surfaces and colloids, 27(2011) 13888-96.

[27] D. Ryan, B.A. Parviz, V. Linder, V. Semetey, S.K. Sia, J. Su, et al., Patterning multiple aligned self-assembled monolayers using light, Langmuir : the ACS journal of surfaces and colloids, 20(2004) 9080-8.

Chapter 5

Micropillars parallel read-out

In this chapter, as second aspect in driving our system toward a multiplex detection method, we describe the development of a parallel read-out method applied to sensors array. An overview of the investigated implementation strategies is first provided, followed by the explanation of the innovative optical method developed during this research project.

5.1 Advantages of parallel read-out in array based systems

The implementation of a parallel read-out method to detect sensor responses is crucial to exploit the full potentiality of array systems, such as pillars array. It improves the single marker detection, and it is complementary to the sensors functionalization with different molecular probes (see Chapter 4) in the development of a multiple detection system. In general, this approach leads to a higher throughput, giving the possibility to obtain more information per unit time. This means an increase of the speed analysis, and also an increase of the detectable information types (ex. a pool of marker), when it is combined with a proper multiple functionalization. Furthermore, the application of a parallel read-out method enables to implement sensor arrays as efficient strategy to increase the sensitive area, reduce the noise and improve the lower detection limits [1]. Indeed, when extreme low concentration (fM) have to be detected on a small sensitive area, such as the pillar top surface (around ten square micrometres), despite a faster kinetic, the frequency of binding events leads to the unlimited growth of the analysis time [2]. Thus, an alternative or additional strategy to the signal amplification presented in Chapter 3, can be the compensation of the rare binding with the increase of the number of detected areas, and thus of the total sensitive area, per unit time.

5.2 Parallel read-out strategies

As well as the single cantilever detection, also the parallel read-out has been performed using different techniques including optical, electrical, capacitive and piezoresistive cantilevers based methods [3]. The dense pillars geometry, imposed as first step to ensure the superhydrophobic state §2.1.2, can be either an advantage or an obstacle toward the realization of a parallel read-out detection. As first attempt, our group has investigated an all-electric read-out method, substituting the piezoelectric pillar actuation with an electrical one driven by Kelvin polarization forces, Toffoli *et al.*[4]. As shown in Figure 5.1a, each rectangular pillar is surrounded by three electrodes; when a non-uniform, quasi-static electrical field is created between the two lateral electrodes, the polarization induced on the micropillars causes its motion. When the oscillation amplitude is high enough, the pillar at resonance can hit a counter electrode placed at short distance (few hundred nanometers), producing an AC current at the same frequency of the resonator, in

parallel to what obtained with a cantilever resonator. In Figure 5.1b is reported the electrical configuration that was found to maximize the oscillation amplitude.

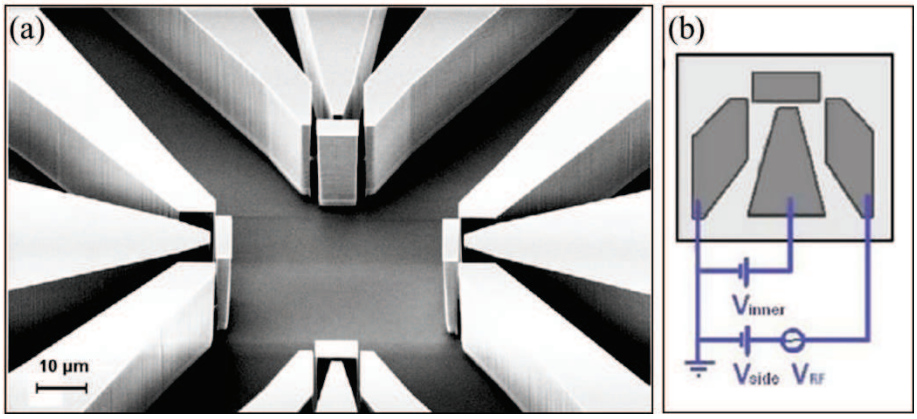

Figure 5.1 – *(a) SEM image of four rectangular micropillars each flanked by three electrodes for actuation driven by Kelvin polarization forces. (b) Electrical configuration schemes which maximizes the oscillation amplitude. Adapted from[4].*

This all-electric read-out method doesn't require the alignment of laser or any other optical components. On the other hand, due to wiring issues, it works effectively only with few pillars. Additionally, the complexity of electrically addressing each individual resonator grows exponentially with the number of pillars; since the advantage of a parallel detection comes from wide arrays, in our case thousands of pillars can be integrated in few mm^2, an alternative optical read-out configuration has been investigated.

In literature, different optical methods have been applied to obtain a cantilever parallel read-out. Starting from optical lever scheme, the first approach proposed used one laser source and one detector for each cantilever, but this leads to high complexity and cost for the integration of multiple and repeated components. To overcome this issue, a single laser was used to scan all the cantilevers of the array, moving the laser source[5, 6] or the array[7]. As an alternative, the cantilever arrays were illuminated by a multiple laser source [8] or by a single collimated laser and the reflected beam from each element was collected by means of a CCD camera, monitoring the changes in the position of each spot [9, 10]. All these approaches suffer of limited speed, low cantilever density and high costs. To overcome these limitations, Ekinci's group has proposed a near field optical technique[11]. In their setup a tapered fiber is positioned close to the array (circa 270 nm), and two lasers, one for the actuation and one for the read out, are combined, as shown in Figure5.2a: the optical dipole forces from the field gradients generated by the first laser around the taper are used to actuate the cantilever, while the scattering of the evanescent optical waves of the second laser are used to sense the displacement. With this technique, up to 63 independent nanocantilevers, with growing length and so with well separated resonance frequencies, were measured, Figure 5.2b. The technique showed a sensitivity to motion of 2-8 $pm \cdot Hz^{-1/2}$.

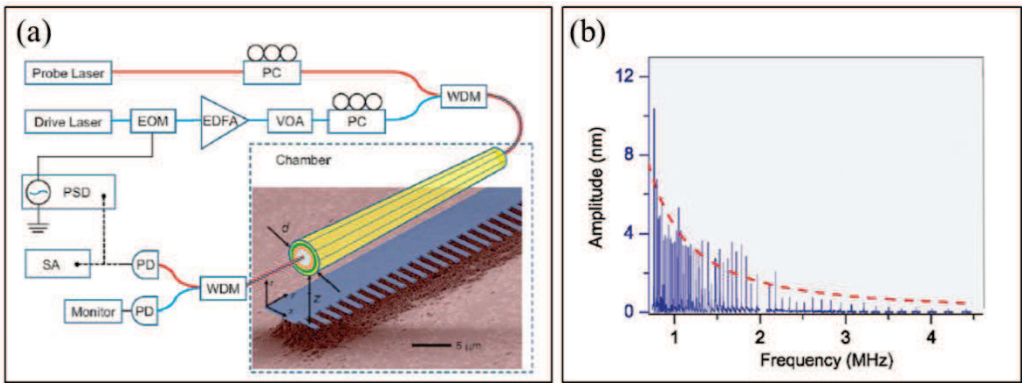

Figure 5.2 – *(a) Experimental scheme of the actuation and detection through near field effect on an array of nanocantilevers. The driving laser passes through an electro-optic intensity modulator (EOM), an erbium doped fiber amplifier (EDFA), a variable optical attenuator (VOA) and a fiber polarization controller (PC), and is combined through a wavelength division multiplexer to the probe laser from another PC. The two lasers pass through the fiber taper and are separated, by another WDM, to two high-speed photodetectors (PD). A spectrum analyzer (SA) is used to measure the noise, while phase-sensitive detection (PSD) is performed through a network analyzer to measure the response. (b) Resonance spectra of 63 independent cantilevers, with different lengths in order to obtain a well separated resonance frequency.*

An interferometric technique has also been recently applied by Sampathkumar and co-workers to monitor in parallel a wide array of double clamped beam resonators, actuated by the photothermal effect of an infrared laser shone on the whole array [1].

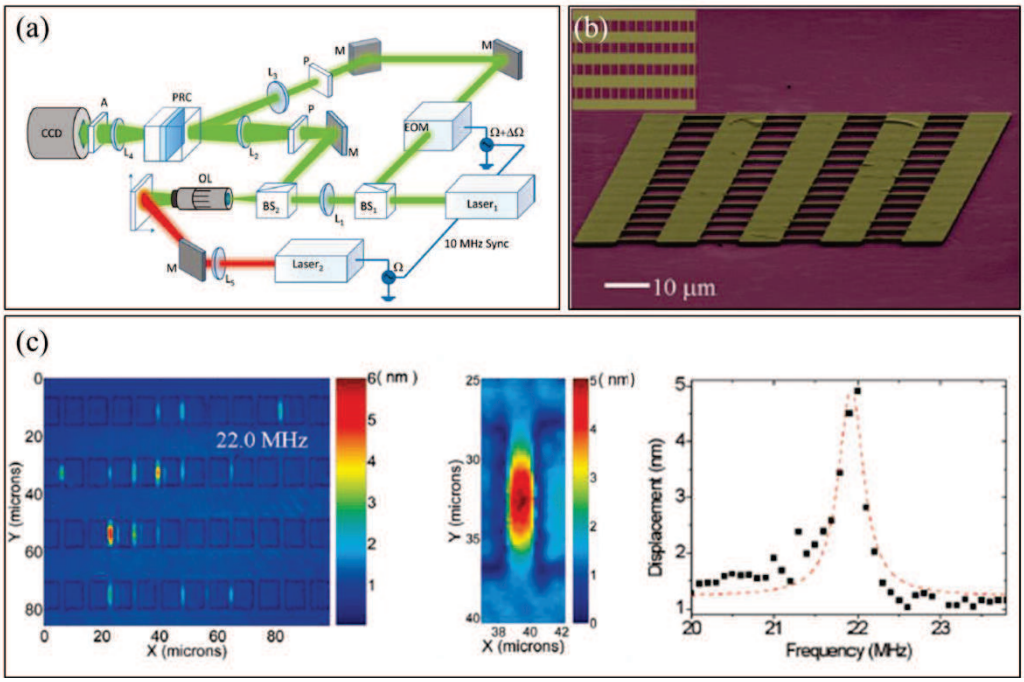

Figure 5.3 – *(a) Schematics of the interferometric setup used for actuation (red laser) and detection (green laser) of multiple resonators, where L1-L5=lenses; BS1 and BS2=beam spitters; P=polarizer; OL=optical objective; M=mirror; EOM=electro-optic modulator; PRC=photorefractive crystal; A=polarization analyzer (b) SEM image of the double clamped beam array. (c) The displacement image of the array under excitation, the deflection of some resonators is visible; the scale bar reports the displacement for each pixel Follows a magnification of the deflection image of a single cantilever and the spectra response for the beam. Adapted from [1].*

In this case, using the adaptive holographic interferometry through the optical setup reported in Figure 5.3a, the high-frequency phase modulation created by the resonating structures is converted, by means of a photorefractive crystal, to a low frequency intensity modulation, detectable with a common CCD; thus, detection of displacements at the second mode of vibration, even with reduced amplitude of oscillation, was demonstrated. With this technique a parallel read-out of up to 1000 resonators is feasible, without stringent requirements of alignment of the laser on the array. Figure 5.3b reports a typical array of double clamped beams, while Figure 5.3c displays the output of the technique, with a color scale that represents the displacement of each point of the resonator at an actuation frequency of 22 MHz. In Figure 5.3c the magnification of the deflection image of a single cantilever and the spectra response for the beam are shown.
Despite the potentiality of these methods, the implementation of similar optical setups is often challenging. Pillar size, few μm squared, imposes the use of high numerical aperture objectives to focus a laser on their top; moreover, pillar oscillations are typically extremely small, even at resonance (amplitude <100nm and angle < 0.01rad) and therefore resonant frequencies are usually monitored by the optical lever method [12, 13]; the implementation of laser scanning systems is not straightforward. Additionally, pillars oscillate in the device plane, and thus also interferometric detection cannot be applied.
To overcome all these issues, a still optical but simple and effective method has been developed and applied in our group: an optical parallel read-out which exploits the blurring effect, observed on pillar imaging, when the same oscillates with amplitudes comparable or larger than the optical spatial resolution; we have named this approach *blur read-out method*. In the following paragraphs the principle and the optical set up are discussed, while the sensibility improvement, gained through the implementation of this method is demonstrated in Chapter 6, applying it to a case of study.

5.3 Optical parallel read-out based on blurring effect

The implementation of the *blur read-out method* has started from an optimization of the pillars fabrication process. Indeed, by a suitable pillar design, such as the one presented in §2.1.1.2 characterized by a concave structure terminating with a vertical post, much higher oscillation amplitudes can be achieved at high resonance frequency (between 2.5 and 3MHz); oscillation amplitudes exceeding hundreds of nanometers in vacuum (depending also on the actuation voltage) have been registered, without loss in sensitivity. Instead, when the undercut involves the entire structure, in order to obtain an increase of the oscillation amplitude, a base thickness reduction is necessary; as consequence pillars oscillate at lower frequency (usually 1-2 MHz) and are less sensitive as mass resonators[14].
Thanks to the compactness of a pillars array, the tens of pillars contained in it can be easily imaged in a single field of view of an optical microscope. Monitoring the pillar array with a CCD, when pillars oscillate, the light reflection path, used to create the image, is slightly deviated (figure 5.4b). During CCD integration time several thousands of oscillation cycles are performed and the CCD image is indeed an average of the pillar position/tilt; thus, when the oscillation amplitude is comparable or larger than the optical resolution, the light intensity recorded by the CCD slightly decreases; the top area of the oscillating pillar appears blurred and, upon suitable illumination, darker. In Figure 5.4b, the optical image of a pillar array actuated by

a piezo at the resonance frequency of one of them is shown: this pillar in the middle is oscillating and appears blurred.

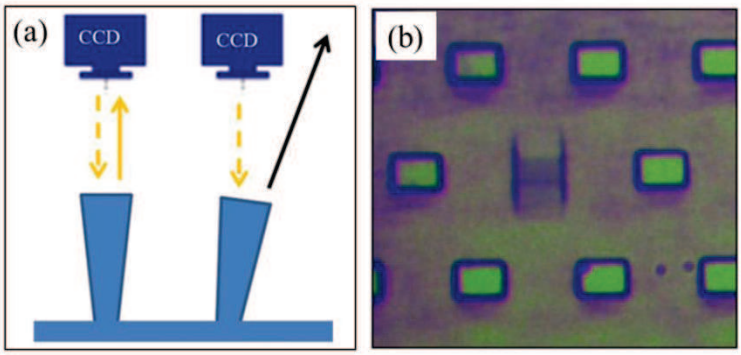

Figure 5.4*– (a) A schematic representation of the pillar detection principle: when pillars oscillate, the light reflection path is slightly deviated and the light intensity recorded by the CCD slightly decreased. (b) Optical image of a pillar array actuated by a piezo at the resonance frequency of one of them; in the middle a pillar is oscillating, and the top of the oscillating pillar is blurred and darker.*

5.3.1 Optical setup and measurements method

The setup developed for the pillars optical parallel red-out is schematized in Figure 5.5a; it consists in a modification of the one presented in §2.2.2.1, where only the optical detection part, previously based on a laser, has been modified. The silicon chip is mounted on the sample holder and load into the vacuum chamber. The pillar oscillation is forced by the piezoelectric actuator, driven by a sinusoidal signal provided by a function generator,. The illumination of the pillars array with white light is provided by a Kohler-like illumination, which consists of a bulb halogen lamp, an optical fiber and a lens, introduced to enlarge the illuminated area of the array. Kohler illumination is used to produce a uniform illumination of the pillars array with a high contrast, in order to better distinguish the top area of pillars from the surrounding portions. The white light passes through a beam splitter and one of the two optical beams is collected by a long working distance objective (OLYMPUS LMPLFLN 50x magnification, numerical aperture = 0.5) and focused on the pillar array. The reflected image passes again the beam splitter and is focused by a tube lens (focal length of 200 mm) on a ½ in. CCD camera (DBK 41BU02, Pyramid Imaging, US), that captures pillars images at 15 frames per second (fps). In Figure 5.5b an image of the complete experimental setup is reported.

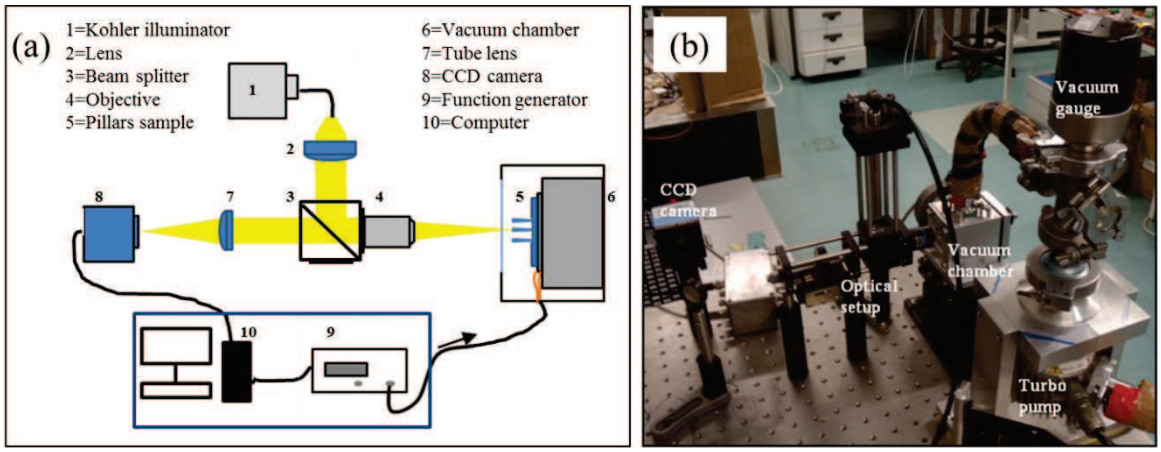

Figure 5.5– *(a) Scheme of the setup developed for the pillars optical parallel read-out. (b) Image of the experimental setup.*

The entire setup and the resonance frequency measurements are controlled by a Labview program developed in our lab. Through the software, first of all, regions of interest (ROIs) are defined as rectangles corresponding to the top area of the investigated pillars. The light intensity, collected by the CCD on each ROI, is recorded and processed in real time by the software. Performing a frequency scan and acquiring the ROIs light intensity as function of the actuation frequency, the dynamic response of the pillars is obtained, and at the resonance frequency a negative peak appear on the spectrum.

The screenshot shown in Figure 5.6, reports how the Labview software interface appears during a frequency scan, and in particular during the oscillation of a pillar. In the upper part, there is the live image of the pillars array. On it, six ROIs has been highlighted just for exemplification; usually a number of ROIs corresponding to the total of visible pillars are investigated. To the right side, scan parameters are shown and below them, during the frequency scan, the current frequency can be read. Below the array image, the live spectrum reporting the light intensity during the time, and thus during the frequency scan has shown; each colored line is associated to a ROI, and thus to a single pillar. As previously explained, at the resonance frequency, the pillar oscillation leads to a blurring, indicated in Figure 5.6 with a green arrow on the array image, and, as consequence, the light intensity decreases. By recording the light intensity versus the actuation frequency, the inverse of a resonance spectrum is recorded: the resonance frequency corresponds to the minimum of the light intensity recorded in the pillar region.

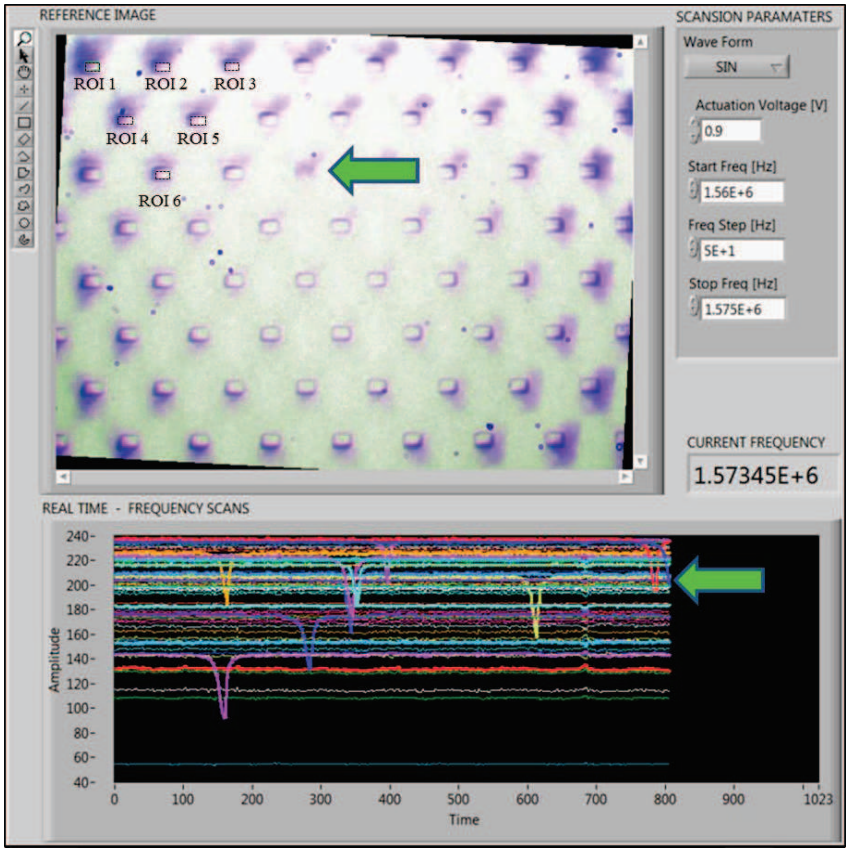

Figure 5.6– *Screenshot of the Labview software interface during pillars measurements, and in particular during the oscillation of a pillar. In the upper part, the live image of the pillars array on which six ROIs has been highlighted and an oscillated pillar is indicated by a green narrow. To the right, scan parameters are shown and below them the current frequency can be read. Below the array image, the live spectrum reporting the light intensity during the frequency scan has shown; the light intensity corresponding to the oscillated pillar is indicated with a green narrow, on it a negative peak is forming.*

A broad preliminary scan at 300 Hz of frequency step and actuation voltage from 6 to 8 V_{pp} is performed to quickly identify the resonance frequency range. After that a more accurate acquisition is performed with 20 Hz resolution and at an actuation voltage sufficient to produce a well detectable darkening of the ROIs at resonance but also low enough to avoid non linear effects. Light intensity collected by the CCD on each ROI at each frequency of actuation is registered and saved.

5.3.2 Results and advantages of the new optical setup

With this method, the number of pillars that can be measured in parallel depends only on the field of view of the imaging system and on the size of the pillars: in our system a maximum of 64 pillars enter the field of view, so the resonance frequency of all of them was measured within 30 minutes, but this limit could be further enhanced by modifying the optical elements, for instance widening the illuminated area. Actually not all the pillars displayed a sufficient oscillation amplitude and so only a subset of those included in the field of

view were measured. Figure 5.7 displays 53 raw traces acquired in parallel corresponding to 53 different pillars in the CCD image, as they achieved from the Labview program.

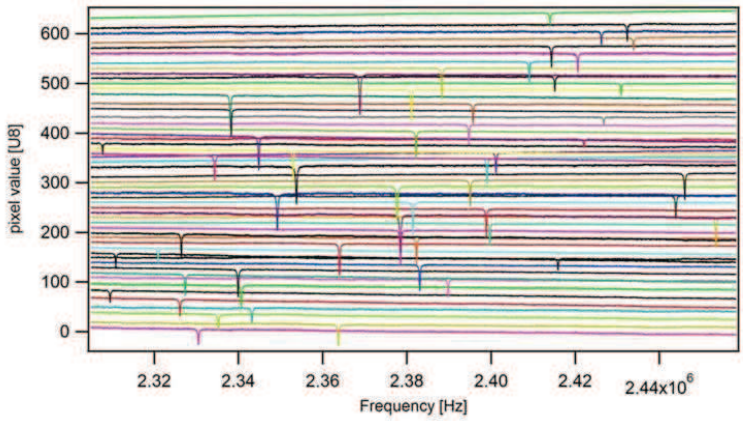

Figure 5.7– *(a) 53 traces corresponding to 53 different pillars acquired in parallel as a function of actuation frequency.*

This approach turned out to be much user-friendlier than the optical lever described in §2.2.2.1, where the laser alignment, signal optimization and spectra collection require almost five minutes per pillar. In addition, it has been reported [15] that laser heating may alter the mechanical properties and/or induce molecular desorption, thus affecting the reproducibility of the measurements. The read-out method proposed here, is less invasive and therefore is more suitable to be adopted for molecular sensing; indeed, the light intensity shone on a single resonator is two orders of magnitude lower (10^3 W/cm^2 in case of Köhler illumination, 10^5 W/cm^2 for a focused 1mW red laser).

Finally our approach offer the opportunity of actuate simultaneously pillars resonating at different frequencies. This mode of operation could reveal very useful in case of interference or beatings of different pillars: pillars can be designed to have well separated frequency and still be characterized in parallel all together. The actuation signal could be formed by the superposition of all the separated frequencies that can be swept independently. By a careful choice of the actuation signal, all the pillars can be driven simultaneously at the resonance frequency, and the evolution of the different resonances can be tracked in parallel in real time. In Figure 5.8, the pillar oscillation is first obtained through a single frequency actuation, the four figures report the live image at four different time, thus at four different frequency. While, on the left the result of a multiple frequency actuation is shown: all pillars previously drive to oscillate in different moment are now moving simultaneously.

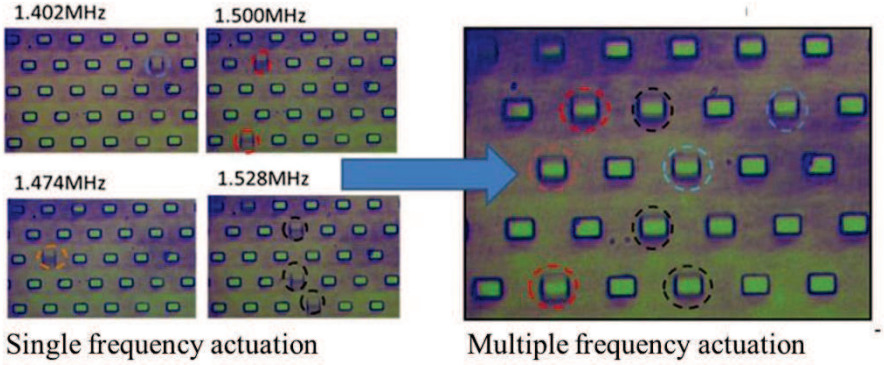

Figure 5.8– *Individual (right)and multiple (left) actuation mode. In the single actuation mode, the four figures report the live image at four different times, thus at four different frequencies. With the multiple frequency actuation: all pillars previously drive to oscillate in different moments are now moving simultaneously.*

References:

[1] A. Sampathkumar, K.L. Ekinci, T.W. Murray, Multiplexed optical operation of distributed nanoelectromechanical systems arrays, Nano letters, 11(2011) 1014-9.
[2] P.R. Nair, M.A. Alam, Performance limits of nanobiosensors, Applied physics letters, 88(2006) 233120.
[3] K.M. Goeders, J.S. Colton, L.A. Bottomley, Microcantilevers: sensing chemical interactions via mechanical motion, Chemical reviews, 108(2008) 522-42.
[4] V. Toffoli, F. Dandash, A. Pozzato, D. Borin, S. Carrato, M. Lazzarino, Actuation of silicon pillar micro-mechanical resonators by Kelvin polarization force, Microelectronic engineering, 111(2013) 1-6.
[5] M. Álvarez, J. Tamayo, Optical sequential readout of microcantilever arrays for biological detection, Sensors and Actuators B: Chemical, 106(2005) 687-90.
[6] J. Mertens, M. Álvarez, J. Tamayo, Real-time profile of microcantilevers for sensing applications, Applied physics letters, 87(2005) 234102.
[7] N.F. Martinez, P.M. Kosaka, J. Tamayo, J. Ramirez, O. Ahumada, J. Mertens, et al., High throughput optical readout of dense arrays of nanomechanical systems for sensing applications, The Review of scientific instruments, 81(2010) 125109.
[8] N. F. Martínez, *et al.*, Label-free protein assay based on a nanomechanical cantilever array, Nanotechnology, 14(2003).
[9] D. Raorane, S. Satyanarayana, A. Majumdar, Nano-chemo-mechanical sensor array platform for high-throughput chemical analysis, Sensors and Actuators B: Chemical, 119(2006) 466-74.
[10] M.Yue e*t al.*, A 2-D Microcantilever Array for Multiplexed Biomolecular Analysis, Journal of Microelectromechanical Systems, 13(2004).
[11] O. Basarir, S. Bramhavar, K.L. Ekinci, Motion transduction in nanoelectromechanical systems (NEMS) arrays using near-field optomechanical coupling, Nano letters, 12(2012) 534-9.
[12] J. Kehrbusch, E.A. Ilin, M. Hullin, E. Oesterschulze, High frequency columnar silicon microresonators for mass detection, Applied physics letters, 93(2008) 023102.
[13] M. Melli, M. Lazzarino and G.Scoles, Fast detection of biomolecules in diffusion-limited regime using micromechanical pillars, ACS nano, 5(2011).
[14] M. Tardivo, *et al.,* Parallel optical read-out of micromechanical pillars applied to prostate specific membrane antigen detection, Biosensors & bioelectronics, 72(2015) 393-9.
[15] J. Lee, F. Goericke, W.P. King, Temperature-dependent thermomechanical noise spectra of doped silicon microcantilevers, Sensors and Actuators A: Physical, 145-146(2008) 37-43.

Chapter 6

Proof of principle: PSMA detection on micropillars devices

In this chapter, as ultimate scope of this work, the advantages in applying micropillars array devices to biosensing are reported detecting a marker for Prostate tumour (PCa): the Prostate Specific Membrane Antigen (PSMA). After the description of the development of a proper bio-recognition layer on the top of pillars, the detection of PSMA in buffer (PBS), at different concentrations, is reported. The analysis is focused on the positive effect that the implementation of the read-out method (see Chapter 5) has on the system sensitivity, and consequently on the range of PSMA concentrations in which the system results to be effective. The following investigation regarding the PSMA incubation time demonstrates that, exploiting the faster kinetics typical of the pillar approach, also for this issue positive results are obtained. Finally, the capability of our device to measure the antigen also in physiological conditions is analysed, showing the results of the PSMA detection in serum. The work reported in this chapter has been published in [1].

6.1 Why to base a proof of principle on PSMA detection

Usually, the evaluation of a new biosensor technology is based on the detection of well-known and clinically used biomarkers such as carcino-embryonic antigen (CEA) or prostate-specific antigen (PSA)[2, 3] if not standard textbook interactions such as for the biotin-streptavidin pair. The relevant concentration of PSA and CEA in blood are respectively 0.16nM and 0,1nM. The detection of these marker is usually performed using immunosensing methods such as ELISA requiring long incubation time, large sample volumes, suitable protocols, primary and secondary antibodies are already optimized. Therefore a direct application of pillar assay would not necessarily lead to a straightforward improvement in clinical applications. Other markers are present in larger amounts but still require an optimization of antibodies and protocols, however, once validated, they could usefully integrate the traditional ones.

Prostate-Specific Membrane Antigen (PSMA), is a transmembrane glycoprotein (molecular weight ≈ 90 kDa) overexpressed by malignant prostate tumours, whose expression is correlated with the disease recurrence[4]. PSMA is less known but its clinical value and diagnostic potential have been demonstrated to be superior compared to traditional PCa-correlated biomarkers, such as PSA. In particular, PSMA serum level has been proposed to discriminate between men affected by benign prostatic hyperplasia (BPH) and PCa patients, whose PSMA serum level is significantly higher (6nM) than in BPH (1nM) [5]. Another important advantage of PSMA over other PCa-correlated biomarkers is that it can be detected in body fluids such as blood/serum, obviating the need of a biopsy.

So far the clinical use of PSMA has been hindered by the lack of suitable assays [6]. Enzyme- and fluorescence-based immunosensitive assays require the use of a further secondary antibody, but the available candidates still need further development to reach the desired sensitivity. PSMA detection is currently performed through western blot or by protein biochips, analysed by surface-enhanced laser desorption ionization/time of flight (SELDI-TOF) machinery[5]. Thus, a label free technique, such as micromechanical sensor weighting, can be the right approach but up to now, based on what reported in literature, the detection of PSMA through cantilevers or other MEMS/NEMS has not been demonstrated yet.
Therefore, we concentrated our effort on PSMA detection, thus pursuing three different tasks at the same time. On one side we used PSMA to demonstrate the performances of our sensing methods. The same results could have been obtained also using traditional markers, with the same degree of confidence. But, second, we also optimize the use of an innovative antibody anti PSMA, developed by the group of M. Colombatti in Verona, demonstrating that its performance is not deteriorated when bound to a solid surface, and, third, we paved the way to a sensor which may flank the traditional assays, helping a more accurate diagnosis of PCa.

6.2 PSMA detection on a micropillars array

PSMA detection has been performed using pillar devices fabricated and made superhydrophobic with the protocols described in § 2.1.1.1 and § 2.1.2.1 respectively. Micropillars arrays coming from different fabrication batches have been calibrated following the procedure described in § 2.2.2., resulting in a mass sensitivity around 25 Hz/fg. The measurements of the resonance frequency have been performed in vacuum with the setup and the method described in § 5.4, collecting, for each sample, the resonance spectra of at least 64 independent pillars. Data Processing is performed as reported in § 2.2.2.2 and § 2.2.2.3; for each sample the value of the deposited mass, and the consequent molecular density, correspond to the average of the signals coming from tens of pillars, all exposed to the same incubation.

6.3 Biofunctionalization of the top area of micropillars

In order to have a device able to capturing PSMA, on the top of pillars a bio-recognition layer was assembled. To this purpose, we used a monoclonal antibody (Ab) against PSMA, named D2B, recently isolated by the group of *Prof. Marco Colombatti, University of Verona* [7-9]. The antibody immobilization on the pillar top was performed exploiting the gold-thiol interaction between a thin layer of gold deposited on the pillars (§ 2.1.3) and a thiolated form of the antibody (D2B-SH). Immediately after gold deposition, the patterned area of the micropillars chip was covered with 20 μL of D2B-SH solution at a proper concentration. The chip was incubated for a certain time at room temperature in a vapour saturated environment, to avoid droplet drying. After that, the chip was rinsed first in PBS and then in milliQ water, then it was used for PSMA detection or blown dried in N_2 and loaded in the vacuum chamber for

measurements. A scheme of the functionalization procedure is displayed in Fig. 6.1. All details about the functionalization protocol are reported in § 6.3.2.1.

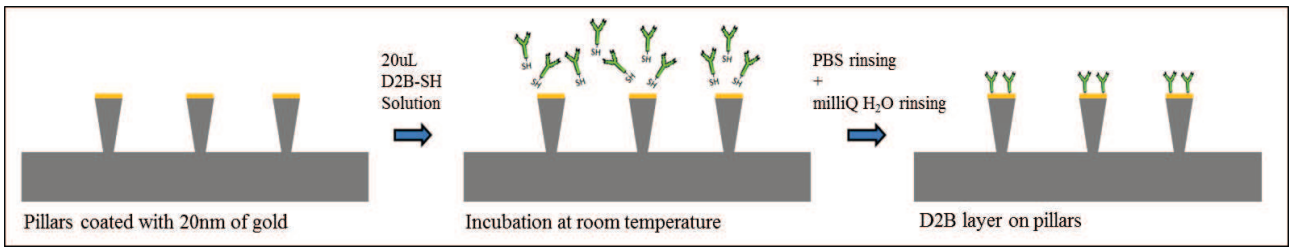

Figure 6.1 – *Schematic representation of the formation of a bio-recognition layer on the top of pillars, based on gold-thiol interaction between the thin layer of gold, deposited on pillar, and a thiolated form of the antibody (D2B-SH). Pillars coated with gold are exposed to a D2B-SH solution at RT, then after a proper time they are rinsed first in PBS and then in milliQ water.*

6.3.1 Antibody D2B and its thiolated form

The IgG1 anti-PSMA Antibody D2B is obtained by conventional hybridoma technology applied on mice immunized with a cell lysate of LnCAP cell membranes and boosted with a recombinant form of PSMA[7]. D2B is able to recognize both cell surface forms (i.e. monomer and dimer) as well as deglycosylated forms of PSMA antigen. Moreover, it has been demonstrated that the recognition of the extracellular fragment of PSMA occurs with a K_D lower than 6nM[9], thus having a better sensitivity of a benchmark existing antibody J591[10].

The thiolated form of D2B, (D2B-SH), is obtained by the reaction of the ε-amino group of lysines in the Ab with the 2-iminothiolane (2-IT) reagent, adding a new-free thiol group, as represented in Figure 6.2. After the chemical modification and the blocking of the reaction, the modified Abs have been purified by gel filtration to remove the excess of 2-IT[11].

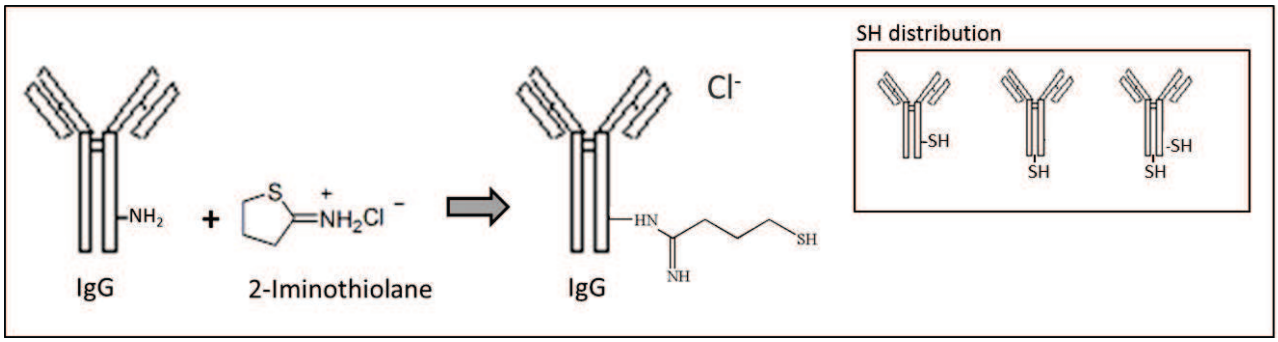

Figure 6.2 – *Schematic representation of the chemical modification of D2B which leads to the thiolated form of the antibody. The ε-amino group of lysines in the Ab D2B reacts with the 2-iminothiolane (2-IT) reagent, adding a new-free thiol group. In the detail box, the three main probable locations of the -SH group.*

The number of added -SH groups were calculated using Ellman's assay: the reaction of the free thiol groups with the 5,5'-dithiobis-(2-nitrobenzoic acid), DTNB is exploited, leading to a cleavage of the dithiol group

and to the production of the dianion TNB^{2-} in water at neutral or alkaline pH. The concentration of the latter is measured by spectrophotometer at 412 nm and related to the amount of the free thiol groups.
From D2B-SH assay, it resulted that on average one -SH group has been inserted per Ab. In particular, due to the conformation of the D2B antibody, IgG1 type[7], this group is preferentially located on the Fc fragment (the heavy, constant chain of the antibody), improving the antibody orientation once it is adsorbed on gold substrate. Finally, the binding capability of the Ab after the thiolation has been confirmed by flow cytometry assay[11].

6.3.2 Micropillars array functionalization with D2B

In order to define the best protocol to obtain on top of pillar a full monolayer of D2B, different incubation times and concentrations of D2B-SH in PBS have been tested. The density of the D2B layer was determined in the follow way: for each sample, the resonance spectra of at least 53 independent pillars were collected. For each pillar, the resonance frequency shift produced by D2B was calculated subtracting to the resonance frequency value recorded after gold evaporation the one obtained after D2B incubation. The frequency shift is converted in a deposited mass value through the calibration constant (25Hz/fg), and then in molecular density (molecules/cm2) assuming a D2B mass of 150kDa (corresponding to 2,4•10-4fg) and a pillar surface of $6•10^{-8}cm^2$. Finally, considering the results obtained for at least 40 pillars, mean values and standard deviations for frequency shift, deposited mass and molecular density are calculated and associated to the sample.

6.3.2.1 Evaluation of different functionalization conditions

The result of the frequency shift and the corresponding antibody density as function D2B-SH concentration and incubation time are reported in Table 6.1.

D2B-SH [M]	time [min]	Δf [Hz]	Density [mol/cm^2]
$7•10^{-6}$	300	-4664±1145	$9.24•10^{12}$
$7•10^{-6}$	10	-4056±709	$8.83•10^{12}$
$7•10^{-8}$	10	-950±70	$2•10^{12}$
$7•10^{-10}$	10	-493±75	$1.02•10^{12}$

Table 6.1 *Frequency shift [Hz] and antibody density [molecules/cm^2] obtained after the pillars functionalization with D2B using different incubation time and concentration of D2B-SH in PSB; mean values and standard deviations obtained for the measurements of at least 40 pillars.*

Analyzing the data, it was observed that at 7μM (initially used to ensure the saturation, as in the ELISA method) the deposited mass obtained both with 5 hours and 10 minutes of incubation was comparable,

therefore we assumed that the saturation was already reached after 10 minutes of incubation. On the other hand, considering the lateral dimension of the Ab around 5nm[12], the high Ab density recorded corresponds to a surface coverage above 100%, that indicates the formation of a multilayers; this is also suggested by the broad distribution of the measurements (see standard deviation values in Table 6.1).

, Keeping constant the incubation time to 10 minutes, two lower concentrations were tested: 700 pM and 70 nM. In these cases the resonance frequency shift was much more homogeneous, and the density varied from $1 \cdot 10^{12}$ mol/cm^2 (for 0.7nM) to $2 \cdot 10^{12}$ mol/cm^2 (for 70nM). Thus, assuming an uniform antibody distribution, at 70nM a monolayer of antibody covering 25% of the active surface was obtained, and this has been chosen as our best condition to provide a sufficiently dense Ab layer.

The effective presence of a D2B layer on top of pillars, and consequently the proof that the mass increase after incubation with D2B-SH solution was due to the antibody deposition, was obtained using an enzymatic immunodetection assay. It is important to highlight that this test demonstrates only the presence of the antibody; no information regarding its orientation and its activity can be deduced. Indeed, the binding capability of the D2B layer can be proved only using it to detect the PSMA.

Generally, to avoid the evaporation of the solution, incubation steps were performed using large drops of solution (20µL) that are in contact with the entire chip, not only with the patterned area. This choice was motivated to facilitate the experimental procedure and reduce the issues linked to the analyte evaporations. In the case of the immunodetection assay test, to get a signal coming only from the top of pillars, a wide silanized and gold-coated micropillars arrays (1.5 x1.5 mm^2 patterned area) were used, and using the methodology described in § 2.2.1.1, a drop of few µL of D2B-SH solution was deposed only on the patterned area as shown in Figure 6.2. Thus, exploiting the Cassie-Baxter state, the incubation was limited to the top of pillars, while the condition used are the same reported above (D2B-SH solution @70nM and 10 min of incubation time).

After the functionalization process, the samples were exposed to a solution of a α-mouse antibody, conjugated with an HRP enzyme, which binds the heavy chain of the eventually immobilized antibody. After one hour of incubation, the sample was rinsed with PBS and exposed to 3,3',5,5'-Tetramethylbenzidine (TMB) a chromogenic substrate for HRP activity detection: if D2B is immobilised on the surface, the secondary antibody will bind it, and consequently HRP remains on the surface causing a change of the solution color from transparent to blue.

In Figure 6.2 b the result of the enzymatic immunodetection assay test is shown, comparing the color of the substrate obtained for a sample incubated with the D2B-SH solution and the one of a control sample incubated only with PBS.

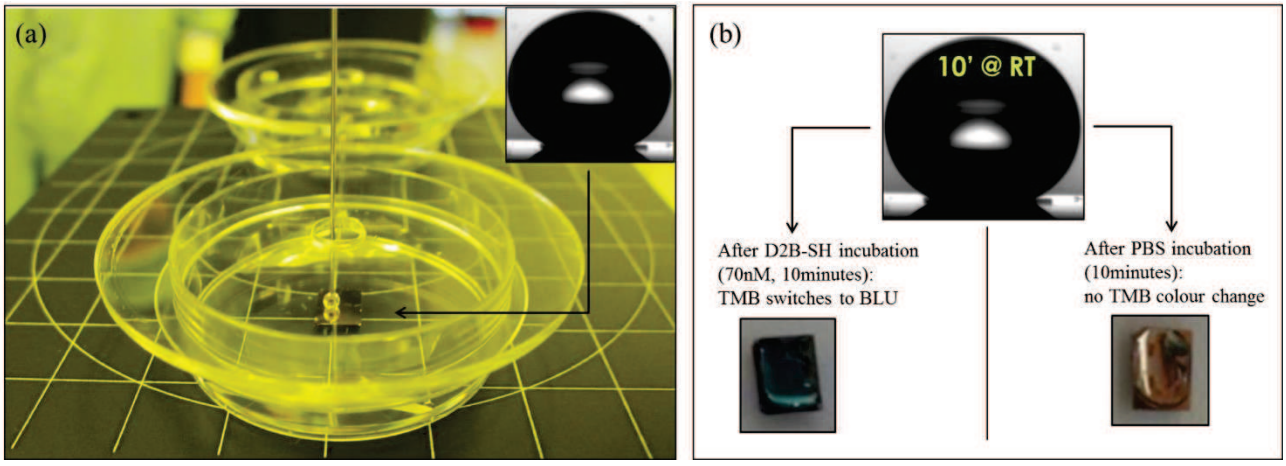

Figure 6.2 – *(a) D2B immobilization on a superhydrophobic micropillar array, incubation performed with the drop analyzer system. In the detail box it is shown that the microdroplet of D2B-SH solution is put in contact only with the patterned area of the chip. (b) Effect of the immunoenzymatic assay by a secondary antibody conjugated to the HRP enzyme: for sample incubated with D2B-SH solution, the effective presence of adsorbed D2B Abs on pillars is confirmed by the color shift of the substrate, from transparent to blue, while in the control case no substrate color change is observed.*

In conclusion the best functionalization conditions, which enables to obtain a sufficiently dense D2B monolayer, have been identified in a concentration of D2B-SH of 70nM and incubation time of 10min. Remarkably, volume and concentrations as small as respectively few µL and nanomolar can be used to a proper micropillars array functionalization. This additionally proves the advantage of micropillars due to their faster kinetic[13, 14]. Indeed, these conditions compared with those used in a standard immunoassay (100µL and 1µM) allows a reduction of the antibody need of more than 5 order of magnitude, which represents a great advantage when the availability of antibody is extremely low or its production is expensive.

6.3 PSMA detection

After the creation of the bio-recognition layer, the micropillars array is ready to be applied to the PSMA detection. But before this, as shown in Figure 6.3, the surface is incubated for one hour with a blocking agent, bovine serum albumin (BSA), 2%w/v, as commonly used in the ELISA protocols: BSA intercalates between the antibodies and saturates all the remaining unspecific adsorption sites. After this passivation step, the micropillars array is exposed for a fixed time to a solution of PSMA, then the devices are six-fold rinsed in PBS. For the following detection experiment we used a commercial, recombinant form of PSMA (r-PSMA, Cusabio, CN).

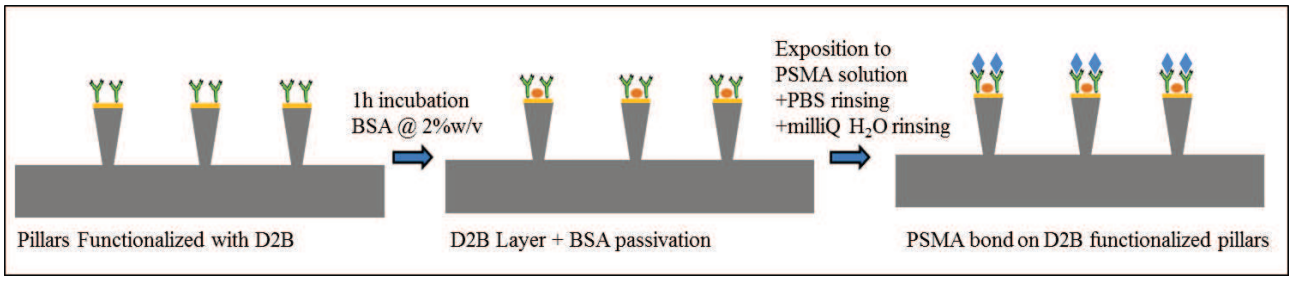

Figure 6.3 – *Schematic representation of steps involved in PSMA detection: micropillars functionalized with D2B are passivated with bovine serum albumin (BSA), 2%w/v to saturate all the remaining unspecific adsorption site; then the device is exposed to a PSMA solution for a certain time, rinsed first with PBS and then with milliQ H_2O.*

Drying procedure (N_2 drying) and measurements in vacuum can alter the Ab configuration and consequently lead to a reduction of its binding affinity. To avoid this, we have chosen to perform directly all the incubation steps (D2B immobilization, BSA passivation and PSMA recognition) without breaking the wet condition and therefore no intermediate measurements were performed. In this way, the measured resonance shift is the difference between the final condition and the after the gold deposition, named Δf*, and represent the sum of the shifts from D2B, BSA immobilization, and PSMA in the specific investigated conditions. Assuming the frequency shift of the single step respect to gold, already quantified during other experiments, to be around 950Hz for the D2B layer and 500Hz for the BSA, the net shift due to the PSMA binding is obtained subtracting 1450Hz to Δf*. The net frequency shift is then converted in mass shift through the calibration constant (25hz/fg), and then into molecules/cm^2 assuming a PSMA mass of 90kDa[7] (corresponding to 1.5•10-4fg) , and a pillar surface of $6•10^8 cm^2$. Finally, considering the values obtained for at least 40 pillars, mean values and standard deviations for frequency shift, deposited mass and molecular density are calculated and associated to the sample.

6.3.1 PSMA detection in buffer

The antigen detection capability of our system has been tested, measuring the resonance frequency shift as response to the device exposition to PSMA solution at different concentrations. In order to create an environment similar to a real sample, PSMA has been diluted in PBS containing 0.2% w/v of BSA (PBS+BSA), being BSA the most abundant protein in the serum. 7 concentrations of PSMA were tested ranging from 300pM to 100nM; for each concentration a new disposable chip was used, thus avoiding any cross contamination effect.

The results are displayed in Figure 6.4, where the frequency shifts with respect to bare Au-coated pillars are displayed vs the PSMA concentration.

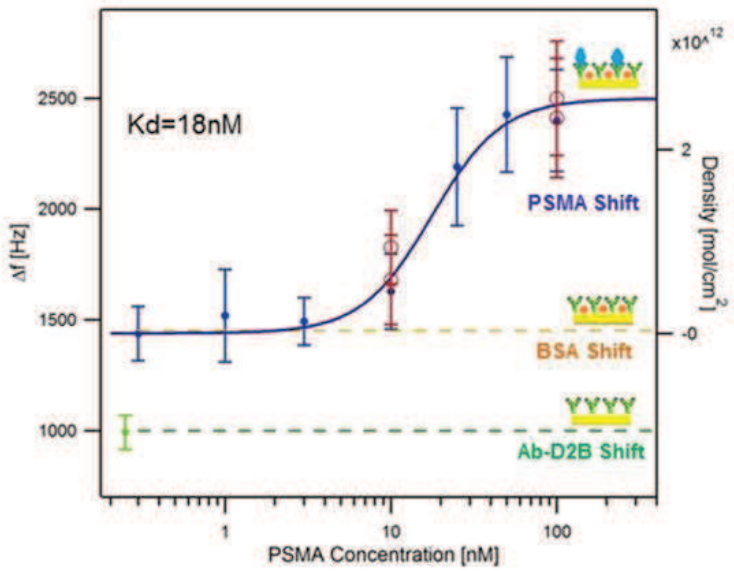

Figure 6.4 – *Results of PSMA detection in PB containing BSA 0.2%w/v, with D2B functionalized pillars devices. 7 concentrations, ranging from 300pM to 100nM, were tested, full blue circles. On the left axis, frequency shifts induced at each PSMA concentration are displayed. On the right axis, corresponding values of PSMA density are shown. The green line indicates the initial frequency shift occurring after D2B adsorption, while the orange one indicates the frequency shift induced by BSA passivation. Each value is the mean shift, and the error bar is the standard deviation of at least 40 independent pillars detected in parallel. Experimental data are fitted with a second order Langmuir curve (blue line) which provides a Kd=18nM. Red empty circles represent data acquired using three different devices to demonstrate the reproducibility of the detection system.*

The frequency shift comprises three contributions: D2B, BSA and PSMA.

The green line indicates the initial frequency shift due to D2B functionalization, the orange line indicates the frequency shift induced by BSA passivation, while the shift induced at each PSMA concentration is displayed with blue symbols. Each point is expressed as the mean and the standard deviation (the error bars) of at least 40 measured micropillars. On the right axis, the PSMA density calculated from the net frequency shift is also reported. Moreover, in order to provide consistent results, each PSMA concentration was repeated twice, and to demonstrate the reproducibility of the system, the detection of PSMA at 10nM and 100nM in PBS+BSA was performed using three different chips fabricated in different production batches: these data are shown as red empty circles in Figure 6.4.

With 100nM of PSMA, the highest tested concentration, the net shift calculated is around 900Hz, which corresponds to a $2x10^{12}$ mol/cm^2 PSMA molecules, meaning that almost all the antibodies bind one antigen. Reducing the concentration of PSMA to 10nM, only 15% of antibodies bind an antigen. The minimum PSMA concentration that we were able to detect was around 1nM.

The data are fitted with a second order Langmuir adsorption curve providing a K_D = 18nM, about three times greater than the value showed by D2B on the native human PSMA (K_D = 6.5nM) [7]. However, this discrepancy could be ascribed to a reduced binding capability of D2B versus the recombinant protein, used in these experiments, with respect to the native one used during the immunization process to generate D2B.

On the other hand, the PSMA density obtained incubating the sample with a PSMA solution at 100nM that leads to the saturation, suggests that more than 90% of the D2B on the pillar top surface are active. This confirms that the condition assumed to create the bio-reactive layer lead to a proper functionalization, although our investigation cannot discriminate between the formation of a single layer of D2B and the formation of 3D islands.

Since the output of the pillar array (at least 40 independent pillars) for each PSMA concentration can be seen as a population of identical sensors subject to identical exposure, the results from different concentrations or from different experiments with the same concentration can be statistically compared to evaluate the significance. Thus, One way ANOVA and t-student tests were performed by GraphPad prism software and a p-Value $p<0.05$ was considered statistically significant.

First, the agreement among measurements conducted on our replicated devices (red empty circles in Figure 6.4) for the two concentration 10nM and 100nM were analysed performing an ANOVA test (significance $p<0.05$). Data distributions for repeated measurements at 10nM and 100nM are reported as box plot in Figure 6.5a and 6.5b respectively; ANOVA test provided a $p=0.11$ for measurements at 10nM and $p=0.14$ for measurements at 100nM, indicating in both case that the repeated measurements are not significantly different or, in other words, that the measurements are reproducible.

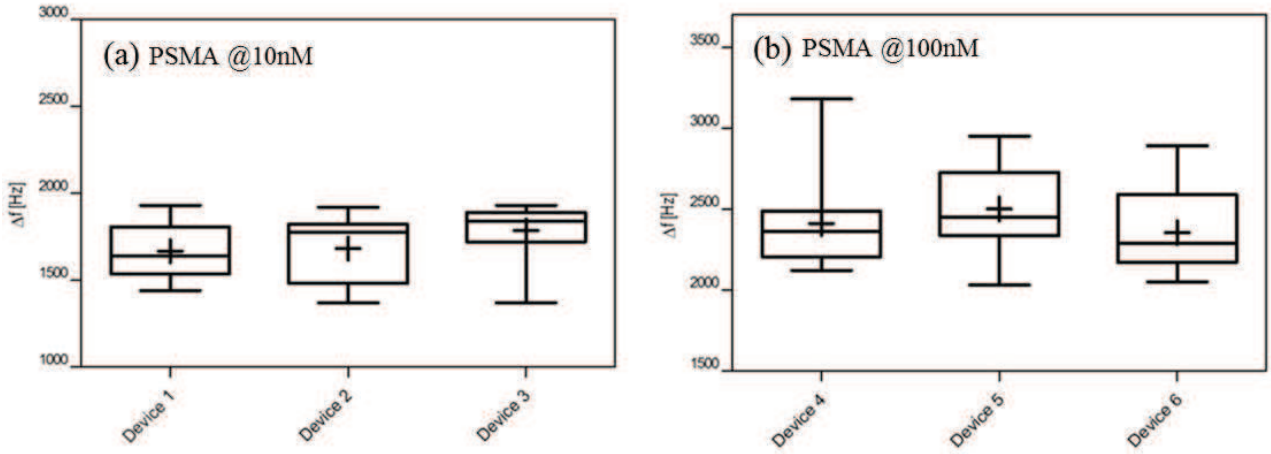

Figure 6.5 – *(a) Boxplot representation of data obtained detecting PSMA at 10nM in PBS containing BSA 0.2%w/v, with D2B functionalized pillars using three different devices. Statistical analysis, one way ANOVA test provides p=0.1132, means and variances are not significantly different (significance p<0.05). (b) Box plot representation of data obtained detecting PSMA in PBS at 100nM with D2B functionalized pillars using three different devices. Statistical analysis, one way ANOVA test provides p=0.1489, means and variances are not significantly different (significance p<0.05).*

Instead, in order to evaluate the difference in the pillar response when they are incubated with different PSMA concentrations, we performed the statistical analysis t-test (significance $p<0.05$), among data obtained detecting PSMA in PBS+BSA at 7 concentration ranging from 300pM to 100nM (blue symbols in Figure 6.4). In Figure 6.6 the box plot representation of data is shown; the significance, the output of the t-test, is represented for each investigated couple as (*) significant $p\leq0.05$, (**) very significant $p\leq0.01$, (***) extremely significant $p<0.001$.

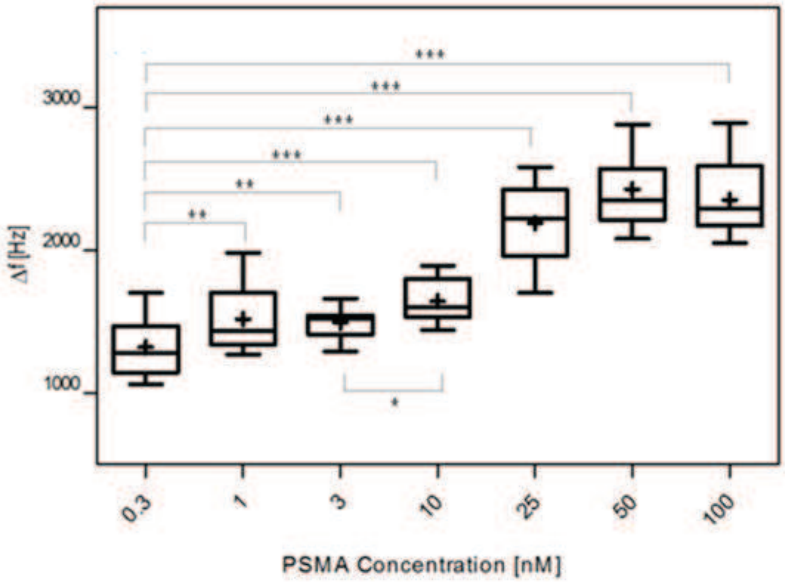

Figure 6.6- *Box plot representation of data obtained detecting 7 different concentrations of PSMA in PBS containing BSA 0.2%w/v, with D2B functionalized pillars devices; concentrations ranging from 300pM to 100nM. Data distributions are compared by t-test (significance p<0.05). Data at 300pM, assumed as baseline, are compared with all the other concentrations. Data at 3nM and 10nM are also compared. Significance is represented for each couple as (*) significant p≤0.05, (**) very significant p≤0.01, (***) extremely significant p<0.001.*

The analysis showed that all the concentrations tested provided from highly significantly ($p < 0.01$) to very highly significantly ($p < 0.001$) frequency shifts with respect to the baseline, which we assumed the sample with the lowest PSMA concentration (300pM), where the detected frequency shift is no more distinguishable from that obtained summing D2B and BSA. Moreover, t-test performed between data obtained for PSMA at 3nM and 10nM provided a $p=0.015$, confirming that we are able to distinguish the response at a 3nM PSMA value (which seems to be associated to the absence of malignancy) from the one at a 10nM (which seems to be associated to the presence of a prostate tumor) [5].

Finally, we performed a set of experiments of PSMA detection in PBS+BSA as function of the incubation time, using a 100nM PSMA concentration. The results are displayed in Figure 6.7: the resonance frequency shift detected (dark squared) are represented as function of the incubation time. As conclusion, reducing the incubation time by a factor 10, the PSMA detection remains constant within the experimental error.

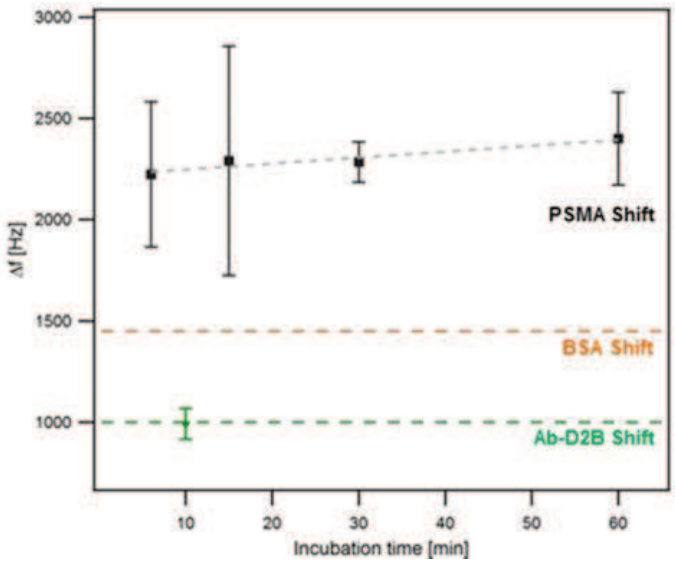

Figure 6.7- *Dark squares show frequency shifts induced by PSMA at 100nM in PBS, containing BSA 0.2%w/v, as function of the antigen incubation time.*

This result is consistent with the previous observations by M. Melli [13] on the dynamics of the formation of a self-assembled monolayer on the pillar surface. The dramatic reduction of the incubation times, that are required to reach surface saturation in the case of micron sized isolated surfaces, is explained in the framework of diffusion limited adsorption as the transition from a 1D diffusion field (valid in case of extended surfaces) to a 3D diffusion field in the case of micron sized surfaces.

The analysis made detecting PSMA in PBS+BSA strongly highlights the great advantages of a detection system based on micropillars array: additionally to the reduction of the incubation time, thanks to a faster kinetics that is proper of the pillars technology, a further improvement of the sensor performances is gained though the implementation of the new read-out detection method. Indeed, even if single measures show a certain variability due to unspecific absorption, or biological noise, by detecting tens of pillars in parallel and therefore averaging the signals coming from a multitude of devices, we can focus our attention on the data distribution rather than on individual measures. In this way we were able to improve the sensibility, and to distinguish the response in a narrow range of concentration, often significant in the diagnostic field.

6.4.2 PSMA detection in serum

To analyse the capability of our device to measure the antigen also in physiological conditions, we performed some experiments of PSMA detection in diluted bovine serum (FCS from Biochrom, Germany). Bovine serum was preferred to human one for the absence of any residual unknown concentration of human PSMA, which would introduce a systematic error in the sensor characterization. Moreover, to preserve the superhydrophobicity of the system, bovine serum was diluted 1:20 in PBS[15].

We used two PSMA concentrations, 25nM and 100nM, and a control sample without PSMA (only diluted serum). For a better comparison, the detected frequency shifts are reported as empty purple triangles over the calibration curve already shown in Figure 6.4.

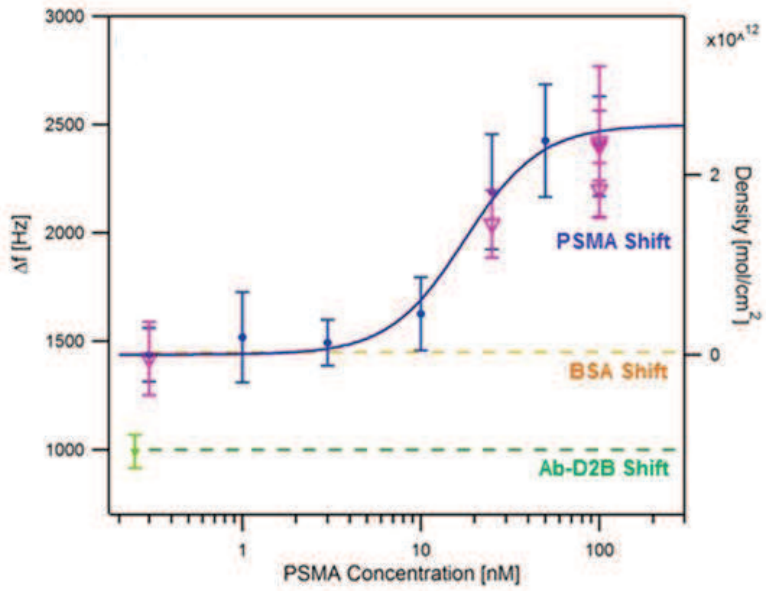

Figure 6.8- *Results of PSMA detection in diluted bovine serum, with D2B functionalized pillars devices. Full blue circles and blue line are the same already shown in Figure 6.4, while empty purple triangles represent data obtained detecting PSMA in diluted bovine serum (1:20 in PBS). Two concentrations, 25nM and 100nM, and a control sample (only bovine serum) were tested.*

The control sample (only diluted serum) induced a shift which is comparable with the baseline assumed after BSA passivation, while samples incubated at 25nM and 100nM show shifts slightly lower than in PBS, but still significantly higher than the baseline.

It is worth to stress that in this last set of experiments the antigen has been added in already diluted serum, while on a hypothetical human sample the dilution needed to maintain the Cassie-Baxter state on micropillars would produce a further reduction of the analyte concentration, lowering the limit of detection of this technique. To overcome this limitation, a pretreatment of the serum could be useful in order to deplete the most abundant species and to change the interaction of the liquid with the hydrophobic micropillars array, lowering the dilution requirement; in parallel, as already mentioned in Chapter 3, the implementation of an amplification method would enable to have a detectable signal also in this case, when the antigen concentration is reduced by a necessary dilution.

References:

[1] M. Tardivo, V. Toffoli, G. Fracasso, D. Borin, S. Dal Zilio, A. Colusso, *et al.*, Parallel optical read-out of micromechanical pillars applied to prostate specific membrane antigen detection, Biosensors & bioelectronics, 72(2015) 393-9.
[2] S.S. Acimovic, M.A. Ortega, V. Sanz, J. Berthelot, J.L. Garcia-Cordero, J. Renger, et al., LSPR chip for parallel, rapid, and sensitive detection of cancer markers in serum, Nano letters, 14(2014) 2636-41.
[3] P.M. Kosaka, V. Pini, J.J. Ruz, R.A. da Silva, M.U. Gonzalez, D. Ramos, et al., Detection of cancer biomarkers in serum using a hybrid mechanical and optoplasmonic nanosensor, Nature nanotechnology, 9(2014) 1047-53.
[4] J.S. Ross, C.E. Sheehan, H.A. Fisher, R.P. Kaufman, Jr., P. Kaur, K. Gray, et al., Correlation of primary tumor prostate-specific membrane antigen expression with disease recurrence in prostate cancer, Clinical cancer research : an official journal of the American Association for Cancer Research, 9(2003) 6357-62.
[5] Z. Xiao, B.L. Adam, L.H. Cazares, M.A. Clements, J.W. Davis, P.F. Schellhammer, et al., Quantitation of serum prostate-specific membrane antigen by a novel protein biochip immunoassay discriminates benign from malignant prostate disease, Cancer research, 61(2001) 6029-33.
[6] D. Hessels, J.A. Schalken, Urinary biomarkers for prostate cancer: a review, Asian journal of andrology, 15(2013) 333-9.
[7] M. Colombatti, G. Fracasso, S. Cingarlini, S. Canevari, M. Figini, Isolated monoclonal antibody or fragment thereof binding prostate specific membrane antigen, conjugates and uses thereof., U.D.S.D. Verona (Ed.)2010.
[8] B. Frigerio, G. Fracasso, E. Luison, S. Cingarlini, M. Mortarino, A. Coliva, et al., A single-chain fragment against prostate specific membrane antigen as a tool to build theranostic reagents for prostate cancer, European journal of cancer, 49(2013) 2223-32.
[9] J. Tykvart, V. Navratil, F. Sedlak, E. Corey, M. Colombatti, G. Fracasso, *et al*., Comparative analysis of monoclonal antibodies against prostate-specific membrane antigen (PSMA), The Prostate, 74(2014) 1674-90.
[10] S.S. Chang, V.E. Reuter, W.D. Heston, N.H. Bander, L.S. Grauer, P.B. Gaudin, Five different anti-prostate-specific membrane antigen (PSMA) antibodies confirm PSMA expression in tumor-associated neovasculature, Cancer research, 59(1999) 3192-8.
[11] F. Selvestrel, F. Moret, D. Segat, J.H. Woodhams, G. Fracasso, I.M. Echevarria, *et al*., Targeted delivery of photosensitizers: efficacy and selectivity issues revealed by multifunctional ORMOSIL nanovectors in cellular systems, Nanoscale, 5(2013) 6106-16.
[12] Y.H. Tan, M. Liu, B. Nolting, J.G. Go, J. Gervay-Hague, G.Y. Liu, A nanoengineering approach for investigation and regulation of protein immobilization, ACS nano, 2(2008) 2374-84.
[13] M. Melli, G. Scoles, M. Lazzarino, Fast detection of biomolecules in diffusion-limited regime using micromechanical pillars, ACS nano, 5(2011).
[14] P. R. Nair, M. A. Alam, Performance limits of nanobiosensors, Appl Phys Lett, 88(P2006).
[15] D. Borin, M. Melli, S. Dal Zilio, V. Toffoli, G. Scoles, G. Toffoli, et al., How to engineer superhydrophobic micromechanical sensors preserving mass resolution, Sensors and Actuators B: Chemical, 199(2014) 62-9.

Conclusions

This thesis has described the development of a high sensitive and multiplexing biosensor, exploiting the advantages coming from the micropillars array approach. In the first part, the implementation of a sandwich, in which a nanoparticles linked to a secondary recognition molecule act as mass enhancer, has been demonstrated as a successful strategy to amplify the mass signal on micropillars sensors. This approach has been tested on a biotin-streptavidin system: it has been proved that, if there is no affinity competition between the sandwich constituents, there is also no influence by the dimension of the surface on the sandwich formation, which can be implemented also on a highly reactive surface such as the top of pillars. Thus, using the protocol defined investigating the formation of the sandwich on patches of different dimensions, it has been demonstrated that the mass signal detected by pillars is amplified 10 times. With the current amplification experimental conditions, the minimum estimated detectable mass is 300ag, but optimizing the ratio between streptavidin and biotinylated nanoparticles (currently calculated to be 100:1), this value can be further reduced.

In the second part of the work, with the aim of developing a multiple detection system, both the individual functionalization of sensors with different molecular probes, and an optical parallel detection method to measure simultaneously a wide number these sensors, have been investigated. For the multiple functionalization a photocleavage strategy, based on an amine protected thiol, has been used: after deprotection of the amine groups, performed with UV light, a covalent binding of different functionalities can be performed. Preliminary investigation on the photocleavable thiol, made using quantum dots as binding functional elements, enabled to define the best conditions in terms of pH and constituents ratio for both cleavage and conjugation. It particular, it was proved that the cleavage efficiency is higher at low pH, as it was supposed studying the cleavage mechanism. After that, the development of a setup for the selective exposure and functionalization of pillars, based on a localized UV laser, is presented. This setup has been tested to define the best exposition dose, but a further investigation has to be performed because the effects of the high intensity of the focused UV laser are not yet clear.

Regarding the development of a multiple pillars read-out, a simple optical method that exploits the blurring effect of the image during pillars oscillation has been developed. With this method the parallel detection of 53 pillars in parallel has been demonstrated. The detection of PSMA (a biomarker used in the prostate cancer diagnose), both in buffer and in serum, has been used as proof of principle; fist the reduction of the incubation time and concentration, as proper advantage of a detection system based on micropillars array, have been confirmed. After that, a further improvement of the sensor performances though the implementation of the new read-out detection method has been demonstrated: considering the signal coming from a multitude of sensors that undergo the same treatments, the variability of the single data due to e.g. biological noise is overcame; this enables to improve the sensibility and to distinguish the response in a narrow range of concentration, often significant in the diagnostic field.

As future perspective, the minimum detection limits obtained through the mass amplification should be deeper investigated, also with other systems, different from biotin-streptavidin. The selective functionalization of pillars array exploiting first different quantum dots and then different antibodies should be demonstrated; finally, these two aspects, combined with the multiple read-out system, should be used to finalize the development of a high sensitive and multiplex system.

Acknowledgements

I want to briefly thank all the people that have collaborated with me:
this was a winning aspect in such an interdisciplinary work.

Thanks to *Prof. G. Scoles* and *Dr. M. Lazzarino* for giving me the opportunity
and the resources to carry on this work.

Thanks to my group (*bio-nano mechanical sensor group, CNR-IOM Trieste*).
In particular thanks to:
Dr. Daniele Borin for the shared work, support and experiences;
Dr. Valeria Toffoli for supporting me in the LabVIEW programs development;
Dr. Simone Dal Zilio and *Dr. Alessandro Pozzato* for the strong support in microfabrication processes;
Dr. Denys Naumenko and *Dr. Laura Andolfi* for supporting me in fluorescence
and AFM imaging and analysis;
Dr. Luca Piantanida and *Valentina Masciotti* for providing me functionalized gold nanoparticles
and for their support in AFM imaging;
Eleonora Funcilllo for the work done together on the mass amplification
through the sandwich assay approach.
Thanks also to *Alessia Matruglio* and *Silvio Greco* because, even with small actions,
they have contributed to make my work easier.

Thanks to the group of *Prof. M. Colombatti* (*University of Verona*) for the provided material
and the collaboration in all the activities related to the detection of PSMA on pillars.
A special thanks to *Dr. Giulio Fracasso* for the strong support on biological topics for both
the PSMA detection and the development of a multiple functionalization protocol for pillars.

Thanks to the group of *Prof. L. Pasquato* (*University of Trieste*) for providing us the photocleavable thiol
for the multiple functionalization of pillars.
In particular, thanks to *Prof. P. Pengo* for the short but strong collaboration in activities related to the
definition of a proper cleavage protocol, for the provided material and analysis.

Thanks to the group of *Dr. L. Casalis (NanoInnovationLAB, Elettra Sincrotrone Trieste)*
and in particular to *Elena Ambrosetti* and *Dr. Pietro Parisse* for the shared material
and the support regarding different topics.

Thanks to all the people that inside and outside the lab have shared with me this experience.